Title

An experimental investigation of mineral solubility in the system MgO-SiO2-H2O-CO2-NaCl at 10 kbar, 500–800 °C: Implications for Si, Mg, and C metasomatism in high pressure environments

Author

Fineman, Daniel

Publication Date

2022

Peer reviewed|Thesis/dissertation

UNIVERSITY OF CALIFORNIA

Los Angeles

An experimental investigation of mineral solubility in the system MgO-SiO_2-H_2O-CO_2-NaCl at 10 kbar, 500–800 °C: Implications for Si, Mg, and C metasomatism in high pressure environments

A dissertation submitted in partial satisfaction of the

requirements for the degree Doctor of Philosophy

in Geology

by

Daniel Fineman

2022

ABSTRACT OF THE DISSERTATION

An experimental investigation of mineral solubility in the system MgO-SiO_2-H_2O-CO_2-NaCl at 10 kbar, 500–800 °C: Implications for Si, Mg, and C metasomatism in high pressure environments

by

Daniel Fineman

Doctor of Philosophy in Geology

University of California, Los Angeles, 2022

Professor Craig E. Manning, Chair

Aqueous fluids rich in CO_2 and NaCl play an important role in the geochemical evolution of mafic and ultramafic rocks in the upper mantle and lower crust, where they act as strong agents of metasomatism and are capable of transporting significant mass and modifying bulk rock composition. Keys to understanding fluid-rock interaction in these settings are constraints on the solubilities of silica and magnesium in mixed fluids at high pressure and temperature. This dissertation outlines three experimental projects which provide new data and improve thermodynamic modeling on mineral dissolution in the system MgO-SiO_2-H_2O-CO_2-NaCl.

The first investigation focused on the solubility of magnesite ($MgCO_3$) in H_2O-NaCl-CO_2 solutions at 10 kbar, from 600-800 °C, at a mole fraction of CO_2 (X_{CO2}) of 0.05 and X_{NaCl} from 0 to halite saturation. These experiments show that the solubility of MgO derived from magnesite

in H_2O-NaCl-CO_2 fluids is significantly lower than that of Ca derived from calcite ($CaCO_3$). The measurements improve thermodynamic modeling to allow prediction of magnesite or dolomite $CaMg(CO_3)_2$ solubility in H_2O-CO_2-NaCl fluids at high pressure and temperature.

The second study investigated the solubility of quartz in H_2O-CO_2 fluids at 500-800 °C and 10 kbar. My results show that, at constant P and T, quartz solubility declines with increasing X_{CO2} at all temperatures investigated. Critical to quantifying silica dissolution is understating its interactions with the H_2O component of any mixed crustal fluid. This can be modeled by accounting for the hydrous components of dissolved silica via the equilibrium

$$SiO_{2,s} + nH_2O = Si(OH)_4 \cdot (n-2)H_2O_{(aq)}$$

quartz hydrated monomer

where *n* is the "hydration number", which corresponds to the total number of H_2O molecules consumed by the transfer of SiO_2 from quartz to the fluid. Previous studies argue that n is a constant independent of P and T. My results require that n varies with P and T, and I show that the variation can be linked to changes in the dielectric constant of H_2O.

The final study investigated the concentration of dissolved SiO_2 in H_2O-CO_2 fluids in equilibrium with quartz + magnesite, talc + magnesite, and forsterite + magnesite at 500-800 °C and 10 kbar. Results show that total Si concentration in equilibrium with quartz + magnesite is identical to that in equilibrium with quartz alone at the same P, T, and X_{CO2}. In contrast to changes in quartz solubility, Si concentration buffered by talc + magnesite and forsterite + magnesite decrease with rising temperature. Comparison to thermodynamic models reveals that the models are generally accurate, provided that silica hydration is taken into account, though I

find that a revised model based on Newton and Manning (2002, 2008) yields better agreement with experiment than that of the Deep Earth Water model (Sverjensky et al., 2014; Fang and Sverjensky 2019). I show how my results can be incorporated into models of Si metasomatism during infiltration of H_2O-CO_2 fluids, as in the mantle wedge above subduction zones.

Taken together, the experimental and modeling results will provide new insights into SiO_2 and MgO mobility in H_2O-CO_2-NaCl fluids in deep crustal and upper mantle settings.

The dissertation of Daniel Fineman is approved.

Edward Donald Young

Edwin Arthur Schauble

Lars P. Stixrude

Craig E. Manning, Committee Chair

University of California, Los Angeles

2022

To those who have helped me along the way, thank you

Table of Contents

List of Figures

List of Tables.

Acknowledgements

I would first like to thank my advisor, Dr. Craig Manning, for providing me the opportunity to explore a completely new field of science and the freedom to discover my own scientific direction. Through his mentorship I gained a new understanding of geochemistry, specifically, the thermodynamics of metasomatizing fluids and he inspired me to connect the natural world to geochemical processes. I am also grateful for the mentoring and enlightening discussions I have had with other faculty members during my time at UCLA . In particular, Prof. Edward Young, whose door was always closed but never locked. His conversations over the years offered me confidence, and his mentoring and lighthearted discussions always improved my day. Thank you for working through problems on the white board and always showing interest in my successes. Because of you, I may understand the nuances of fugacity one day. To David Jewitt, though you may never read this, thank you for explaining many "unique" cloud formations and other atmospheric phenomena I witnessed. You always had your own photograph stashed away somewhere, proving to me that it was not so unique after all and maybe even quite mundane. Additionally, what is graduate school without departmental gossip, and oh boy, did I learn a lot from you. To An Yin, may I one day be "almost" as funny as you are.

To my girlfriend, Abby, thank you for keeping me on my toes, and always convincing me to go climbing trips. To my many climbing friends, thank you for the weekly camping trips and pad island slumber parties in freezing conditions. If it were not for you, I would not be who I am today and would never have climbed the numerous high balls in Bishop and along the California

coast. The trips kept me sane and motivated for the week to come. These memories will last me a lifetime.

To my friends at UCLA, thank you for cheering me up with good humor, sarcastic jokes about my nascent Ph.D degree, my secondary degree in complaining, and for the friendships. In no order, thank you to; Dr. Heather Kirkpatrick, Dr. Kaitlyn McCain, Dr. Ellen Alexander, Erik Weidner, Dr. Liutauras Rusaitis, and everyone else for providing me endless support throughout my journey.

Adam and Bob, where do I even start? I would not be the scientist I am today without you. I can never thank you two enough for the hundreds of hours of help and mentorship. Experimental petrology is tricky, especially when welding large quantities of water, and the analysis can be overwhelming. Nothing felt too difficult when we were all hanging out in the lab together. Bob you are a true pioneer of the field and the most committed scientist I have ever met. I used to be skeptical about your favorite saying, “we are the best in the world at solubility measurements” , but now I am a strong believer.

To my parents and siblings, you are the best, and I could not ask for a better family. I loved our nearly daily phone calls and facetimes with my brothers and sister; my life is much better with all of you in it. Lastly to Luna who was one of the best puppies I have ever known. Although your life was cut short, the two years we had together were amazing. I will always remember your little face sticking out the car window, and the pure joy of the wind blowing across your face. Although you are gone, you will always be remembered.

Curriculum Vita

Education

2012 B.A., BIOLOGY: Oberlin College
2018 M.Sc., GEOLOGY: University of California Los Angeles

Certificates, training, & Awards

Distance Education Scholarship, 2020-2021 — Gemological Institute of America
Department Fellowship Award, 2020-2021 — University of California Los Angeles
Department Fellowship Award, 2019-2020 — University of California Los Angeles
Department Teaching Award, 2018-2019 — University of California Los Angeles

Selected Conference Abstracts

Fineman, D., & Manning, C. E. (2016, December). Phase relations among K-feldspar, muscovite and H_2O at 1.0 GPa and 800 °C: Implications for metasediment dissolution and melting at high pressures and temperatures. In AGU Fall Meeting Abstracts (Vol. 2016, pp. V31B-3094).

Fineman, D., & Manning, C. E. (2017, December). Magnesite Solubility at 800 ºC, 10 kbar, in H_2O-CO_2±NaCl solutions: implications for carbon transport in the mantle. In AGU Fall Meeting Abstracts (Vol. 2017, pp. V13A-0373).

Fineman, D., & Manning, C. E. (2019, December). Decreasing temperature and increasing X_{CO2} boost silica dissolution in the system MgO-SiO_2-H_2O-CO_2. In AGU Fall Meeting Abstracts (Vol. 2019, pp. V51D-0188).

.

Chapter 1: Introduction

1.1 Introduction

Subduction zones are our planet's largest recycling system and transfer volatiles such as H_2O and CO_2 from the Earth's surface to its deep interior. During subduction, the juxtaposition of rocks with different bulk compositions results in strong metasomatism associated with the liberation of H_2O and CO_2 rich aqueous fluids. Although much is understood about the chemistry of these fluids at Earth's surface and shallow depths, our understanding of these fluids in deeper settings, such as subduction zones, remains limited.

At modest pressures and temperatures carbon species become fully miscible with H_2O, enabling deep crustal and mantle fluids to become highly enriched in carbon. Open system processes control the rate of carbon subduction into the mantle and allow for the migration of highly reactive carbon-rich fluids along the subducting slab and into mantle wedge. While much is known about how pure H_2O interacts with rocks and transports elements in subduction settings, the complications that arise from the addition of CO_2 remain little explored even though carbon-rich fluids have been recognized as important agents in metasomatizing fluids. Of particular importance are the consequences of the interaction of carbon-rich fluids and mantle lithologies. For example, Kelemen and Manning (2015) noted that the amount of subducted carbon currently recycled into the mantle is so uncertain that it may range from none to over half. A major source of uncertainty is the amount of CO_2 that is sequestered in the mantle wedge above subduction zones. Moreover, slab fluids may be extremely complex mixtures of H_2O-CO_2 and salts (e.g., Manning and Frezzotti 2020). Profound carbon mobility can result from the

dramatic enhancements in carbonate mineral solubility arising from high P and T, and elevated salt contents that are to be expected in subduction zones.

The purpose of my dissertation is to gather meaningful data within subsections of MgO-SiO_2-H_2O-CO_2-NaCl systems. First, a key product of the interaction of such fluids with the mantle is the Mg carbonate magnesite ($MgCO_3$). However, little is known about the solubility of magnesite in deep fluids. In Chapter 2, I describe new experiments designed to assess how magnesite solubility changes as a function of NaCl concentration. This work allows assessment of why the presence of NaCl profoundly enhances carbonate mineral solubility.

Chapter 3 of this dissertation focuses on quartz solubility in H_2O-CO_2 fluids. It is well known that the addition of CO_2 diminishes the solubility of quartz at constant P and T. However, the nature of the decline proves to be extremely useful for modeling the interaction of water molecules with silica during the dissolution process. My work shows that previous studies have been too limited in P and T to generate an accurate model of this process. I derived a new semi-empirical model, based on Born solvation theory, which links the dielectric constant of water to water-silica interaction in mixed fluids.

The new model for the hydration of dissolved silica provides a necessary foundation for accurate modeling of silica metasomatism by H_2O-CO_2 fluids. Also required for understanding deep metasomatic systems such as subduction zones are experimental constraints on the solubilities of key silica buffering mineral assemblages. Chapter 4 describes experiments on the solubilities of the mineral pairs magnesite + quartz, magnesite + talc, and magnesite + forsterite in H_2O-CO_2 fluids. The results provide critical tests of thermodynamic models and provide a basis for modeling couple C and Si metasomatism during fluid infiltration in the mantle wedge of subduction zones.

The results of this dissertation provide a better understanding silica-fluid-carbonate interactions to help better understand the carbon cycle, and silica mass transfer and speciation in quartz-undersaturated systems.

1. References

Kelemen, P. B., & Manning, C. E. (2015). Reevaluating carbon fluxes in subduction zones, what goes down, mostly comes up. Proceedings of the National Academy of Sciences, 112(30), E3997-E4006.

Manning, C. E., & Frezzotti, M. L. (2020). Subduction-zone fluids. Elements, 16(6), 395-400.

Chapter 2: Solubility of magnesite in H_2O-CO_2-NaCl: implications for carbon transport and mantle-wedge metasomatism in subduction zones

Abstract

Subduction zones play an essential role in recycling Earth's surficial carbon into the deep mantle. While there is general agreement that approximately 55±15 Mt carbon are subducted each year, there is significant debate about how much of this carbon is recycled into the mantle, with estimates ranging from effectively none to nearly all (Kelemen and Manning 2015). One major source of uncertainty arises from the limited experimental measurements of carbonate solubility and a poor understanding of carbonate dissolution and aqueous speciation. Over the past two decades numerous papers have investigated the solubility of calcium carbonates (calcite and aragonite) in H_2O ± salt solutions, but these phases are unlikely reservoirs for carbon in the mantle. Instead, magnesite ($MgCO_3$) is a predicted product of the interaction of slab fluids and the mantle wedge. However, its solubility in H_2O-CO_2-NaCl fluids remains poorly known. I carried out an experimental investigation of magnesite solubility using hydrothermal piston-cylinder methods. Results were obtained at 600-800 ºC, 1 GPa, in H_2O-CO_2 ± NaCl solutions. The NaCl mole fraction (X_{NaCl}) ranged from 0 to 0.4. Magnesite dissolves incongruently to brucite ($Mg(OH)_2$) in pure H_2O at all conditions investigated. Solubility measurements were therefore conducted at X_{CO2} = 0.05, fixed by addition of hydrous oxalic acid and maintenance of high f_{O2}, where magnesite dissolution was congruent allowing utilization of simple weight-loss methods. In NaCl-free experiments, magnesite molality (m_{MgCO3}) at 1.0 GPa, 700 and 800 °C at

(X_{CO2} = 0.05) is very small, approximately 0.008, 0.02, respectively. The presence of NaCl results in nearly 45 and 60X greater solubility near halite saturation at 700 and 800 °C, respectively. The 3rd order form of magnesite dissolution in H_2O-CO_2-NaCl solutions was modeled using the aqueous speciation-solubility code EQ3 (Wolery, 1992) adapted to include equilibrium constants calculated with the Deep Earth Water (DEW) model (Sverjensky et al. 2014). EQ3 was run iteratively by finding the pH at which $m_{Mg,total}$ equaled the $m_{C,total}$ in excess of the carbon molality derived from OAD (X_{CO2} = 0.05 corresponds to m_C = 2.922). The thermodynamic data from Fang and Sverjensky (2019) resulted in nearly 1000 times greater magnesite solubility then experimentally determined. Sverjensky et al. (2014) at 1 GPa, underpredicted magnesite solubility all experimental conditions $m_{Magnesite}$ = 0.00296 (800 °C), 0.00149 (700 °C), and 0.00087 (600 °C) and was used as the starting point for our calculations. At 1 GPa and 800 °C modification of logK for the reaction $MgOH^+ = Mg^{+2} + OH-$ to -6.4, consistent with values measured by Macris et al. (2020) resulted in magnesite solubility that agreed with my experiments. The small addition of NaCl (NaCl < 1 molal) resulted in $MgCl^+$ becoming the predominant Mg species in the modeled fluids. EQ3 modeling implies that the cubic behavior of magnesite solubility results from the association of Na^+ and Cl^- to form $NaCl_{aq}$. This implies that association of $NaCl_{aq}$ is the primary explanation for the pattern of magnesite solubility increase.

2.1 Introduction

Subduction zones play an important role in the carbon cycle (e.g., Jarrard 2004; Dasgupta and Hirschmann 2010; Burton et al 2013; Kelemen and Manning 2015; Plank and Manning 2019). While there is general agreement that approximately 55±15 Mt carbon are subducted each year, there is significant debate about how much of this carbon is recycled into the mantle, with estimates ranging from effectively none to nearly all (Kelemen and Manning 2015). Kelemen and Manning (2015) noted that a major source of this uncertainty is poor understanding of the role of the mantle wedge as a potentially important carbon storage reservoir. Carbon storage would most likely arise from formation of the carbonate minerals magnesite ($MgCO_3$) and/or dolomite ($MgCa(CO_3)_2$), generated – at least in part – during interaction of mantle minerals with carbon-bearing saline aqueous fluids derived from the slab. Rare examples of rocks exhumed from this setting support this possibility. Magnesite and dolomite are common accessory minerals (Flak and Keleman 2015 and Menzel et al., 2020), and where fluid inclusions are preserved they may contain up to 45 wt % NaCl (e.g., Scambelluri and Phillipot 2001)

There is abundant literature on Ca-carbonate dissolution in H_2O±NaCl±CO_2 at lower crustal and upper mantle conditions (Ellis 1959; Fein and Walther 1963; Newton and Manning 2002; Caciagli et al. 2003; Facq et al., 2016; Eguchi and Manning 2020). These experiments demonstrate that calcite solubility is low in pure H_2O at crustal P and T. The very high pressures of subduction zones lead to substantial increases in $CaCO_3$ solubility in H_2O ($CaCO_3$ as aragonite; e.g., Facq et al., 2014; Kelemen and Manning 2015). The addition of NaCl further enhances $CaCO_3$ solubility at a given P and T (e.g., Newton and Manning 2002; Facq et al., 2016).

In contrast to work on the solubility of $CaCO_3$ minerals, magnesium carbonates have received substantially less attention. This is problematic because magnesite and dolomite, rather than calcite or aragonite, are the expected products of mantle wedge metasomatism by slab-derived fluids. At present, the only investigation of Mg carbonate solubility relevant to the pressure range of subduction zones is the study by Pan et al. (2013), which used ab initio molecular dynamics to predict magnesite solubility in pure H_2O up to 10 GPa. The results suggest that magnesite solubility in pure H_2O is lower than aragonite at similar P and T; however, the calculations did not consider NaCl and experimental verification is required.

The present study investigates the role of NaCl on magnesite solubility aqueous fluids at high pressure and temperature. I conducted experiments on magnesite solubility in H_2O-CO_2-NaCl fluids in a hydrothermal piston cylinder apparatus at 1.0 GPa and 600 – 800 ºC. The experiments determined the solubility of magnesite at mantle conditions in the system H_2O-CO_2-NaCl under a range of bulk compositions. The experimental results provided the basis for thermodynamic modeling using the Deep Earth Water (DEW) model (Sverjensky et al. 2014) to assess the stability of relevant aqueous species. Discrepancies between the experiments and the predicted solubility trends suggest the presence of new aqueous species and form the basis for theoretical prediction of solubility involving more complex phases, such as dolomite, for which order-disorder and solid solution effects complicate direct experimental investigation.

*2.*2. Methods

2.2.1 Thermodynamic considerations

At the conditions of the present experiments, determination of the solubility of magnesite ($MgCO_3$) in initially pure H_2O is complicated by incongruent dissolution. This was confirmed by

initial experiments at 700 °C and 1.0 GPa in pure H_2O, which resulted in the formation of brucite ($Mg(OH)_2$), consistent with the predicted phase relations at low X_{CO2} (Fig. 2.1). Preliminary experiments using H_2O-NaCl solutions at $X_{NaCl} < \sim 0.5$ also yielded brucite. These results are problematic because the presence of residual brucite prevents direct determination of magnesite solubility by weight-loss methods.

The problem of brucite growth was overcome by adding sufficient CO_2 to suppress brucite. Thermodynamic calculations indicate that magnesite is stable at 1.0 GPa and 600, 700 and 800 ºC, at $X_{CO2} = 0.0031$, 0.0105, 0.0277, respectfully, which is sufficient to maintain equilibrium (Fig. 2.1). Accordingly, initial X_{CO2} in all experiments was $\geq X_{CO2} = 0.05$. Oxalic acid dihydrate (OAD): $(COOH)_2 \cdot 2H_2O$) was used as a CO_2 source to generate fluids on the H_2O-CO_2 join. During initial heating of an experiment, OAD breaks down to produce CO_2, H_2O, and H_2 through the reaction

$$(COOH)_2 \cdot 2H_2O \rightarrow 2CO_2 + H_2O + H_2 \qquad (2.1)$$

The H_2 produced in Eq. (2.1) is a complication where CO_2 is a desired fluid component. In the absence of any external control on oxidation state, the H_2 reacts with CO_2 at the conditions of the present study, leading to CO_2 reduction and graphite precipitation via

$$CO_2 + 2H_2 \rightarrow C + 2H_2O \qquad (2.2)$$

Graphite

(Brooker et al. 1998). Adopting standard states of unit activity for pure minerals

$$K_{cco} = \frac{a_{H2O}^2}{a_{CO2} f_{H2}^2} \quad (2.3)$$

Graphite precipitation is problematic because it can lower X_{CO2} sufficiently that brucite is stable.

To prevent the reduction of CO_2 to graphite, low hydrogen fugacity (f_{H2}) (i.e., high oxygen fugacity (f_{H2O})) must be maintained over the duration of an experiment. In the present study, this was achieved using H-trap ("buffer") double capsule method. At experimental conditions, Pt is permeable to H_2 (Chou et al 1978; Eugster and Wones 1962). Accordingly, a sealed Pt inner capsule filled with a chemical system capable of controlling H_2 fugacity was used. During the experiment, the breakdown of the OAD creates a steep chemical gradient between H_2 in the fluid and the inner buffer capsule. The gradient promotes H_2 diffusion into the buffer, resulting hematite's reduction to magnetite (Fe_3O_4). While both hematite and magnetite are present, the equilibrium

$$3Fe_2O_3 + H_2 = 2Fe_3O_4 + H_2O \quad (2.4)$$

holds and the equilibrium constant K_{hm} fixes the fugacity of H_2 via

$$K_{hm} = \frac{(a_{H_2O})(a_{Fe2O3})^3}{(f_{H_2})(a_{Fe3O4})^2} \quad (2.5)$$

Adopting standard states of unit activity for pure minerals. H_2O and CO_2 at any temperature and pressure, and unit fugacity of pure H_2 and O_2 at 1 bar and any temperature, and assuming pure

hematite and magnetite and negligible H_2 concentrations, the value of f_{H2} imposed by the equilibrium in the buffer capsule is

$$f_{H2} = K_{hm}^{-1} \tag{2.6}$$

In the buffered capsule, homogeneous equilibrium among the H-O components of the fluid phase is described by

$$H_2O = H_2 + 1/2O_2 \tag{2.7}$$

for which

$$K_w = \frac{f_{O2}^{1/2} f_{H2}}{a_{H2O}} \tag{2.8}$$

Combining equations 2.6 and 2.8 leads to

$$f_{O2} = (K_w K_{hm} a_{H2O})^2 \tag{2.9}$$

Equation (2.9) shows how fixing hydrogen fugacity in the buffer capsule translates to control of oxygen fugacity of the fluid. Provided that these values are greater than that of CO_2-graphite equilibrium

$$f_{O2} = K_{cco} K_w^2 {a_{H2O}}^2 \tag{2.10}$$

graphite precipitation in the capsule is suppressed. Note that a result of lowering the activity of H_2O in Eq. (2.10) is a decrease in f_{O2} becomes more negative. This highlights that control of f_{H2} and fO2 by buffering is essential.

Use of the hematite-magnetite buffer was found to be inadequate because, due to the small inner capsule size restraint, hematite quickly reduced completely to magnetite allowing Eq. (2.2) to proceed and resulting in CO_2 consumption and brucite formation. In order to increase run durations, a MnO_2 (Pyrolusite) buffer was favored due to its much higher initial f_{O2}, which in turn allowed longer experimental run times. Equations (2.11-2.13) show that MnO_2 reduces to MnO (Manganosite) over several intermediate reactions. As long as Mn_2O_3 (Bixbyite), Mn_3O_4 (Hausmannite), or MnO (Manganosite) are present for the duration of the experiment, Eq. (2.11-2.12), CO_2 will not be consumed, and magnesite will remain stable.

$$2MnO_2 + H_2 = Mn_2O_3 + H_2O \quad (2.11)$$

$$3Mn_2O_3 + H_2 = 2Mn_3O_4 + H_2O \quad (2.12)$$

$$Mn_3O_4 + H_2 = 3MnO + H_2O \quad (2.13)$$

Adopting the same standard states of unit activity as Eq. (2.6), Equations (2.11-2.13) fix the H_2 fugacity.

$$K_{PB} = \frac{(a_{H_2O})(a_{Mn2O3})}{(f_{H_2})(a_{MnO2})^2} \quad (2.14)$$

$$K_{BH} = \frac{(a_{H_2O})(a_{Mn3O4})^2}{(f_{H_2})(a_{Mn2O3})^3} \quad (2.15)$$

$$K_{Hmango} = \frac{(a_{H_2O})(a_{MnO})^3}{(f_{H_2})(a_{Mn3O4})} \quad (2.16)$$

combining Eq. (2.6) with equations (2.14), (2.15) and (2.16), respectively, fixes f_{O2} at each reaction.

$$f_{O2} = (K_w K_{PB} a_{H2O})^2 \quad (2.17)$$

$$f_{O2} = (K_w K_{BH} a_{H2O})^2 \quad (2.18)$$

$$f_{O2} = (K_w K_{Hmango} a_{H2O})^2 \quad (2.19)$$

Provided that these f_{O2} values are greater than that of CO_2-graphite equilibrium, graphite formation (Eq. (2.2)) does not occur.

A distinctive pistachio green color indicated the presence of MnO from the consumption of Mn_3O_4 which is black in appearance allowing for easy identification. The exhaustion of the Mn oxide buffer occurred when Eq. (2.13) reacted to completion, which was identified when the entire buffer turned pistachio green. At this point, Eq. (2.19) no longer occurred and the buffer no longer fixed f_{O2} above the carbon dioxide-carbon (CCO) buffer resulting Eq. (2.2) and the destabilization of magnesite to brucite. Figure 2.2 shows that hematite + magnetite equilibrium and hausmannite+manganosite equilibrium always keeps f_{O2} many orders of magnitude higher

than the value at which CO_2 reduces to graphite, consistent with the absence of graphite in any run products below (see below)

2.2.2. Experimental Apparatus and Assembly

All experiments were conducted in an internally heated piston cylinder apparatus with 2.54 cm diameter piston, NaCl pressure medium, and a graphite heater sleeve. Temperature was controlled using a Pt-$Pt_{90}Rh_{10}$ thermocouple with an estimated accuracy of ±3 °C (Bohlen 1984; Manning and Boettcher 1994), and pressure was measured with a Heise Bordon tube gauge that has an estimated uncertainty of ±0.03 GPa. Pressure was achieved using the piston-out technique, in which assemblies were first cold pressurized to 70% of the final value before temperature was increased. Thermal expansion of the assemblies during the subsequent heating raised the pressure to the target pressure of 1.0 GPa. Pressure was held within ±0.015 GPa of the desired pressure through the duration of the experiment by bleeding pressure when necessary. At final run conditions, the NaCl cells are frictionless and require no pressure correction (Manning and Boettcher 1994).

2.2.3. Starting material and loading of experimental charges

The experiments employed natural, high-purity magnesite from Pomba Pit, Serra das Eguas, Brumado Brazil. X-ray diffraction indicated near-end member crystals. Electron microprobe analysis showed ≤0.217 wt% FeO and ≤0.008 wt% CaO. The fluid components included ultra-pure 18-MΩ-cm water, 99.6 % pure sodium chloride (Fisher chemical), and 99.998% pure oxalic acid (Fisher chemical). We used two forms of magnesite depending on the experiment: a single crystal or a finely powdered mixture. Magnesite single crystals were

cleaved to rhombohedra with a razor blade from a larger crystal, then sonicated in ethanol to dislodge any small crystal fragments and adhering impurities. Starting crystal weights varied between 0.5 and 1.5 mg. Finely powdered magnesite was prepared by repeated grinding of crystals in an agate mortar under acetone. All magnesite samples were dried at 600 °C for 10 minutes to volatilize residual organic solvent.

Experiments were performed using a double-capsule technique similar to Manning and Boettcher (1994) with the addition of an internal buffer capsule. The two inner capsules were 1.5 mm outer diameter (OD) platinum (Pt) tube 5 mm in length and the outer capsule was 3.5 mm OD Pt tube 18 mm in length. All Pt tubes were cleaned with acetone and annealed using a Bunsen burner.

Experiments at 1.0 GPa, 600, 700 and 800 °C and $X_{NaCl} < 0.5$ constrained magnesite solubility from the weight changes of a single magnesite crystal. In contrast, at 1.0 GPa, 800 °C and $X_{NaCl} > 0.5$, magnesite solubility was so high that single-crystal weight-loss experiments were impractical. At these conditions, a bracketing method using powdered magnesite was employed.

For single-crystal weight-loss experiments, the first inner capsule was made from a piece of Pt sample tubing which was partially crimped on one end. Then a single magnesite crystal was weighed, placed inside, and then the remaining open end of the capsule was crimped shut. The capsule was perforated twice with a needle. The ends were burnished to remove any loose Pt slivers, and then the capsule was weighed. The perforations allow fluid and magnesite to interact and equilibrate during the experiment. The inner capsule retained any magnesite fragments that might dislodge during the experiment and minimized consequences of quench precipitation (Newton and Manning 2002, 2006).

The second inner capsule was welded shut on one end using LAMPERT PUK 5 precision welder, at 14% power and 4 ms, packed with a hematite, MnO_2, or a MnO_2-water mixture and welded shut. This capsule served as an internal buffer capsule, which was required to sequester H_2 from the breakdown of hydrous oxalic acid and then maintain oxidizing conditions. Refer to section 2.3.2 above.

Experiments at 800 °C, $X_{NaCl} > \sim 0.5$, magnesite solubility was so high that simple weight loss methods could not be used due to crystal fragmentation. To address this, a bracketing technique which used crushed magnesite was implemented to constrain solubility (Tropper and Manning 2007). Magnesite was crushed in a mortar and pestle until becoming a fine powder, approximately five minutes. An outer capsule was loaded with a precisely measured mass of crushed magnesite and fluid phase components (H_2O + oxalic acid ± NaCl), followed by the inner buffer capsule. H_2O was added with a microliter syringe and allowed to evaporate until the desired weight was present, then pinched shut and weighed, then welded, and weighed again. All weighing's were made with a Mettler Toledo UMX20 ultramicrobalance with an uncertainty of $1\sigma = 0.2$ μg).

2.3. Solubility Determination

2.3.1. Single-crystal experiments

Quenched capsules were retrieved from the furnace assembly and soaked in distilled water to dissolve any adhering NaCl. Retrieved capsules were typically inflated due to high internal CO_2 pressure, providing a preliminary assessment of run success. The capsule was then weighed as a check on capsule integrity; if a capsule lost weight it was assumed to have leaked and results were discarded. Outer capsules were carefully cut open with a razor blade, and both

inner capsules were retrieved. In some cases, the inner magnesite capsule was flattened or the magnesite crystal was crushed by contact with the buffer capsule, preventing accurate weighing. These runs were also discarded.

Solubility determination required removal of the fluid from the inner magnesite-bearing capsule, but simple drying caused halite precipitation. To circumvent this, the inner capsule was placed in a beaker with distilled water, heated to 70 °C for ~5 minutes while stirring, then dried and weighed. The process was repeated until the inner capsule came to a consistent mass, signaling that all salt had dissolved. Care was taken to ensure that no loose fragments were lost. All weight loss measurements were calculated from weight changes of the crystal from the Pt inner capsule and represent a minimum solubility. Magnesite solubility in H_2O at ambient conditions is negligible.

2.3.2. Bracketing measurements

At 800 °C, 1.0 GPa, and X_{NaCl} ~ 0.6, magnesite solubility was so large that weight-loss methods could not be used. In this case, solubility was established by a bracketing method. I performed two experiments (DC_65 and DC_66) with different starting magnesite masses at the same X_{NaCl}. Methods similar to those above were used in these experiments, with the exception that finely ground magnesite was used the inner capsule, and the solubility was bracketed by the presence or absence of magnesite in the run products, as determined by petrographic microscope on dried run products mounted in high-dispersion oil with an index of refraction of 1.5400.

2.3.3. Vapor transport

A complication in single-crystal solubility determinations is the potential growth of new crystals during the run ("vapor transport crystals", e.g., Caciagli and Manning 2003). When it occurs, vapor transport is likely promoted by a small (1-2°C) temperature gradient across the capsule (Tropper and Manning 2007). Accumulated experience in our laboratory indicates that very low mineral solubility and the absence of NaCl promotes growth vapor transport crystals.

In the present study, evidence of vapor transport was only seen in experiments at 600 °C, where new magnesite rhombohedra precipitated on outer capsule walls during experiments. The textures of vapor-transport magnesite differ from those of calcite which may reach >100 μm in the longest dimension (Caciagli and Manning 2003). In contrast, we observed vapor-transport magnesite crystals that were on average ~55 μm in length and more numerous (Fig 2.3a). Collecting vapor transported crystals for weighing proved impossible due to their small size and their tendency to tightly adhere to the Pt walls. Magnesite crystals formed during quench in NaCl were texturally distinct disordered masses of birefringent carbonate, easily distinguished from the rhombohedral vapor transport crystals (Fig. 2.3b).

2.4. Results

Experimental results are given in Table 2.1. In the following discussion, the mole fraction of solvent component i in solution X_i defined by $X_i = n_i/(n_{NaCl} + n_{H_2O} + n_{CO_2})$, where n_i is number of moles of the subscripted component in the fluid. The minor dissolved magnesite is not included.

Textures of run products were observed by optical and scanning electron microscope (SEM). A Tescan Vega3 scanning electron microscope equipped with EDAX and EDS detector was used

for all SEM investigation. Fig. 2.3b shows quenched vapor phase with highly disordered masses of birefringent carbonate in 1.5400 dispersion oil. Intergrown skeletal quenched-magnesite crystals can be seen outlining NaCl crystals (Fig. 2.3c). Figure 2.3d shows a run-product magnesite crystal with rounded edges and an etched crystal face which resulted from dissolution. Magnesite in bracketing experiments show substantial recrystallization and growth of euhedral magnesite into rhombohedra with approximately 250 μm base, and the presence of large fluid inclusions, some containing both a vapor bubble and halite daughter crystals, indicating their growth during the run (Fig. 2.3E).

2.4.1. Results of solubility experiments

Run duration necessary to attain equilibrium was determined by seven experiments at 700 °C and 1.0 GPa at $X_{NaCl} = 0.15$ and $X_{CO2} = 0.05$ (Fig. 2.4, Table 1). Time-independent studies demonstrated equilibrium was achieved by 4 hr. Runs at 800 °C would require less time for equilibration and it was assumed that >1.5 hr was sufficient.

Table 2.1 provides 1σ errors in magnesite solubility derived from my experiments. These values are propagated errors associated with each weighing step. In practice, this source of error is very small due to the high precision balance employed. External reproducibility associated with all other aspects of the experiments (P and T accuracy, capsule cleaning, etc) are the primary cause of modest scatter in the results. This can be seen in Fig. 2.4. The standard error in the seven experiments >3 hr in duration is 0.003 molal, slightly greater than the 1σ of ~0.001 molal derived from weighing-error propagation for individual experiments.

Figure 2.5 shows experimental results at 600, 700 and 800 °C and 1 GPa. Solubility measurements are presented in molality (m), defined as the moles of dissolved magnesite per kg

of H_2O. In NaCl-free experiments, magnesite molality (m_{MgCO3}) at 1.0 GPa, 700 and 800 °C at (X_{CO2} = 0.05) is very small, approximately 0.008, 0.02, respectively. At 600 °C (X_{CO2} = 0.05) in NaCl-free solutions, vapor transported crystals always formed and solubility measurements were not feasible. The variation in magnesite solubility with X_{NaCl} for aqueous solutions containing H_2O-CO_2-NaCl indicates considerable enhancement in solubility to that in NaCl-free solutions at X_{CO2} = 0.05.

The dissolution of magnesite adds oxidized carbon to the fluid. Assuming this carbon is present as CO_2 (see below), this will increase the X_{CO2} of the final fluid from the nominal starting value of 0.05. However, the comparatively low solubility of magnesite makes this shift negligible. For most results, the increase in X_{CO2} is 0.001-0.003. In the highest solubility runs (DC_65 and DC_66) at 800 °C, X_{NaCl} ~ 0.6, a maximum increase of 0.008 was observed.

2.4.2 Phase relations at 700 °C, 1.0 GPa

A sufficient number of experiments was conducted at 700 °C, 1.0 GPa, to constrain phase relations in the system MgO-H_2O-CO_2-NaCl at this P and T. Experiments in progressively more saline H_2O-NaCl solutions without added CO_2 at 700 °C and 1.0 GPa yielded brucite to X_{NaCl} as high as 0.345 (Fig. 2.6, Table 2.1.). Only Magnesite was observed at X_{NaCl} = 0.453. This demonstrated the importance of a minimal CO_2 concentration to stabilize magnesite. Large, euhedral halite crystals were observed in run products at $X_{NaCl} \geq 0.500$, indicating halite saturation. This is confirmed by observation of constant solubility at $X_{NaCl} \geq 0.453$ (e.g., Newton and Manning, 2002; Eguchi and Manning 2020). Thus, halite saturation in initially pure H_2O is between 0.45 and 0.50. Experiments X_{CO2} = 0.05 never contained brucite, and evidence for halite

saturation was not observed at the highest X_{NaCl} = 0.413. These constraints were used to construct the phase boundaries shown in Figure 6.

2.5. Discussion

2.5.1. Solubility trends and solution mechanisms

Figure 2.5 illustrates that, as with calcite solubility (Newton and Manning 2002; Eguchi and Manning 2020), increasing salinity greatly enhances magnesite solubility at a given temperature. Figure 2.5b illustrates at 700 °C, magnesite solubility at X_{NaCl} = 0.40 is m_{Mag} = 0.327, about 40 times greater than in H_2O-CO_2 alone (m_{Mag} = 0.0077). Increasing temperature results in great magnesite solubility at a given X_{NaCl}, where at 800 °C, 1.0 GPa magnesite solubility increases from m_{mag} = 0.02 (X_{NaCl} = 0.0) to m_{Mag} = 0.564 (X_{NaCl} = 0.4), approximately 28 tines greater than that in H_2O-CO_2 solutions (Fig. 2.5a). The trends in the data at 600 °C imply similar behavior. As shown in Fig. 2.5D, the degree of enhancement increases with increasing temperature at high X_{NaCl}. Notably however, solubility appears to be similar at 600 and 700 °C at low X_{NaCl} from 0 to ~0.2.

Establishing the functional form of the solubility isotherms in Fig. 2.5 is important because it provides useful insights into the nature of the solute species. Figure 2.5 shows that the initial increase in solubility is concave downward, but after an inflection the increase changes to concave upward. The inflection point moves to lower X_{NaCl} as T rises. Least-square regression to 3rd order polynomials at 800, 700, and 600 °C, respectively, gives:

$$m_{mag} = 0.026261 + 1.5333X_{NaCl} - 2.672X_{NaCl}^2 + 5.4928X_{NaCl}^3 \quad (2.20)$$

$$m_{mag} = 0.010084 + 1.0552X_{NaCl} - 2.2694X_{NaCl}^2 + 4.0225X_{NaCl}^3 \quad (2.21)$$

$$m_{mag} = \ 0.0024969 - 7.2004X_{NaCl} - 12.766X_{NaCl}^2 + 12.766X_{NaCl}^3 \qquad (2.22)$$

Correlation coefficients are 0.99414 (800 °C), 0.99633 (700 °C) and 0.99412 (600 °C). The intercepts of 0.026 and 0.0101 at 800 and 700 °C and are quite close to the measured values of 0.022 and 0.008 molal. The regression curve at 600 °C predicts that solubility in NaCl-free solutions is 0.0025 molal, consistent with the trend implied by the measurements at 700 and 800 °C.

The isothermal cubic dependence of magnesite solubility on X_{NaCl} clarifies previous results on calcite solubility at similar conditions (Newton and Manning, 2002; Eguchi and Manning, 2020). Newton and Manning (2002) inferred a simple X_{NaCl}^2 dependence, which they attributed to a calcite-solution equilibrium described by: $CaCO_3 + 2NaCl_{aq} = CaCl_{2aq} + NaCO_{3aq}$. This functional form fits their result well at approximately $X_{NaCl} > 0.1$, however, it consistently misfits the data at $X_{NaCl} < 0.1$. Eguchi and Manning (2020) noted a simple X_{NaCl}^2 dependence in a range of salt solutions at $X_{NaCl} > 0.1$, but as with Newton and Manning (2002), data at low X_{NaCl} were mostly insufficient to carry out more accurate fitting to higher order equations. Figure 7 shows two cases where data at low X_{NaCl} allow demonstration that calcite solubility isotherms are also likely cubic in form.

2.5.2 Theoretical solute speciation modeling of magnesite dissolution

The most likely interpretation of the cubic form of the solubility isotherms is that there is a boundary between domains where different dissolved species predominate, but the experiments alone are insufficient to identify the particular species. I tested this hypothesis using thermodynamic models of magnesite dissolution and aqueous speciation in H_2O-CO_2-NaCl

solutions at experimental conditions. This was carried out using the aqueous speciation-solubility code EQ3 (Wolery, 1992) adapted to include equilibrium constants calculated with the Deep Earth Water (DEW) model (Sverjensky et al. 2014). Activity coefficients of aqueous species are calculated using the B-dot extension of the Debye-Hückel equation (Helgeson 1969, Helgeson and Kirkham 1976). This equation is strictly valid only 3 molal NaCl, but Manning (2013) showed that it can accurately be applied at high P and T to ~10 molal (X_{NaCl} = 0.15). Although these conditions are at the low end of the full range of X_{NaCl} investigated, the modeling is nevertheless useful for investigating changing species abundance with NaCl concentration. I used the DEW data set of Sverjensky et al. (2014) rather than the updated data of Fang and Sverjensky (2019). The latter study results in highly inaccurate predictions of magnesite solubility at the present experimental conditions. For example, the 2019 data set predicts magnesite solubilities in excesses of 20 molal at 800 °C and 1.0 GPa, nearly a 1000 times great then measured here. This error is due to at least two factors: (1) modifications by Fang and Sverjensky (2019) were are optimized for very high P and T well outside the range studied here, and (2) apparently erroneous changes to the logK of $NaHCO_{3,aq}$ dissociation. For these reasons, the 2014 data set appears to be more accurate at the present experimental conditions and was used for all calculations below.

As a starting point, I calculated magnesite solubility at 600, 700, and 800 °C in NaCl-free solutions. EQ3 was run iteratively by finding the pH at which $m_{Mg,total}$ equaled the $m_{C,total}$ in excess of the carbon molality derived from OAD (X_{CO2} = 0.05 corresponds to m_C = 2.922). Using the thermodynamic data from Sverjensky et al. (2014) at 1.0 GPa, the modeling gives $m_{Magnesite}$ = 0.00296 (800 °C), 0.00149 (700 °C), and 0.00087 (600 °C). The predicted values at 800 and 700 °C are lower than those observed in my experiments, and the predicted value at 600

°C is lower than that implied by Eq. (2.22) (Fig. 2.5). These results imply that one or more Mg species is more stable than is predicted by the DEW data set. The predominant Mg species is predicted to be $MgOH^+$, followed by Mg^{+2} and then $Mg(HCO_3)^+$. Data for the Mg^{+2} ion are well known based on independent experiments and theoretical models. Results of experiments on forsterite-enstatite solubility in pure H_2O at 800 °C, 1.0 GPa (Macris et al., 2020) suggest greater stability of $MgOH^+$ relative to Mg^{+2} and OH^- than is predicted by the DEW model. Modification of the logK for the reaction

$$MgOH^+ = Mg^{+2} + OH^- \quad (2.23)$$

to -6.4 at 800 °C, 1.0 GPa, leads to prediction of forsterite solubility in H_2O that is consistent with values measured by Macris et al. (2020). Using this value yields magnesite solubility of 0.019 molal at an initial $X_{CO2} = 0.05$, the same within error as in experiment DC_1. Thus, the underprediction of magnesite solubility in NaCl-free fluids implies greater stability of $MgOH^+$ species than predicted by the DEW model. Notably, regardless of the logK used for Eq. (2.23), nearly all carbon in solution is present as CO_2 rather than bicarbonate. Predicted pH of solutions ranges from 5.47 at 800 °C to 4.61 at 600 °C.

The change in magnesite solubility with NaCl concentration was investigated at 800 °C, 1.0 GPa, using the modified logK for Eq. (2.23). Figure 2.8a shows that, as in my experiments, the DEW data predict that magnesite solubility increases with added NaCl. However, the increase with NaCl is less pronounced than is observed experimentally. Addition of even small amounts of NaCl <1 molal leads to formation of $MgCl^+$ as the predominant Mg species in the model fluids. The suppressed dependence of magnesite solubility on NaCl in the models thus

suggests that $MgCl^+$ is substantially more stable than predicted. For the purposes of illustration, I modified the logK for the reaction

$$MgCl^+ = Mg^{+2} + Cl^- \quad (2.24)$$

from -3.1 to -5.0. This produces a change in magnesite solubility with NaCl that is broadly similar in form to that observed (Fig. 2.8a): at low X_{NaCl}, solubility rises with a decelerating dependence on salt content until $X_{NaCl} \sim 0.1$, above which the solubility rise begins to accelerate. EQ3 becomes unstable and solutions are not possible above $m_{NaCl} \sim 15$ ($X_{NaCl} \sim 0.2$). Although, the results at high X_{NaCl} qualitatively demonstrate a cubic form to the solubility rise, similar to (and more pronounced than) the experiments.

Evaluation of species abundance changes can be used to assess the cause of the inflection. Figure 8b shows that most Mg is in solution as $MgCl^+$, and that there is no change in Mg speciation that correlates with the location of the inflection in the solubility isopleth. In contrast, Fig. 2.8c and d show that association of Na+ and Cl- to form $NaCl_{aq}$ is such that below $X_{NaCl} \sim 0.1$, Na+ and Cl- predominate, whereas above this composition $NaCl_{aq}$ predominates. This implies that association of NaCl is the primary explanation for the pattern of magnesite solubility increase. Regardless of $NaCl_{total}$ concentration, $MgCl^+$ is the primary host of the Mg from magnesite. Below $X_{NaCl} \sim 0.1$, the primary dissolution reaction can be written as:

$$MgCO_3 + Cl^- + H^+ = MgCl^+ + OH^- + CO_2 \quad (2.25)$$

When $NaCl_{aq}$ becomes predominant, the primary dissolution reaction transitions to

$$MgCO_3 + NaCl_{aq} + H^+ = MgCl^+ + NaOH_{aq} + CO_2 \quad (2.26)$$

Because the solubility of magnesite is small relative to the total abundance of NaCl, the patterns of species change (Fig. 2.8c) are amplified to give the functional form of the magnesite solubility isotherm.

It is important to note several caveats. This analysis is based on a significant extrapolation of activity coefficient equations to high salt concentration. Moreover, several candidate species are effectively ignored in the DEW model, largely for lack of constraining data. These include $MgCl_2$ and $NaCO_3$ aqueous species. It is possible that either or both play a role in the fluid phase at these conditions. However, additional associated species would likely be subject to similar effects as NaCl. Thus, it appears that the nature of species association, chiefly NaCl, plays a primary role in governing the form of the magnesite solubility increase with NaCl at a given P and T.

2.5.3. Geological Applications

The results suggest that chloride-bearing fluids strongly enhance the solubility of magnesite. The experimental data help explain geological examples of strong Mg carbonate metasomatism in the mantle wedge and crust. For example, Kaminsky et al (2013) demonstrated magnesite+KCl+NaCl fluid inclusions in diamonds from Juina area, Mato Grosso, Brazil. The presence of saline fluids at mantle conditions provide direct evidence for chloride-rich brines in the mantle, and show that they produce substantial $MgCO_3$ mobility. This observation is consistent with predictions of Isshiki et al. (2004).

Ferrando (2012) reviewed the occurrence of Mg-rich metasomatic rocks in the Alps, which display evidence for highly channelized Mg-metasomatic fluids infiltrating the continental crust along stain zones. The center of the strain zones are enriched by ~30 wt % MgO, indicating high Mg mobility. Additionally, the Brossasco-Isasca Unit in the Alps provides evidence for Mg-Cl-rich fluid inclusions up to 28 wt% NaCl, demonstrating the presence of saline-MgO metasomatizing fluids.

2.6. Conclusion

The results of this study present several conclusions:

1. Magnesite solubility in pure water is very low, and a minimum X_{CO2} is required for congruent dissolution.
2. The aqueous speciation-solubility code EQ3 (Wolery, 1992) adapted to include equilibrium constants calculated with the Deep Earth Water (DEW) model (Sverjensky et al. 2014) underpredicts magnesite solubility in H_2O-CO_2 solutions and imply that one or more Mg species is more stable than is predicted.
3. At 1.0 GPa and 800 °C modification of logK for the reaction $MgOH^+ = Mg^{+2} + OH^-$ to -6.4, consistent with values measured by Macris et al. (2020) and resulted in magnesite solubility of 0.019 molal at an initial $X_{CO2} = 0.05$, the same within error as in experiment DC_1.
4. The small addition of NaCl (NaCl < 1 molal) resulted in $MgCl^+$ becoming the predominant Mg species in the modeled fluids.

5. EQ3 attributes the cubic behavior of magnesite solubility the association of Na^+ and Cl^- to form $NaCl_{aq}$. This implies that association of NaCl is the primary explanation for the pattern of magnesite solubility increase
6. Calcite and magnesite solubility require a cubic equation to capture the dissolution of carbonate

These findings present the first experimental solubility measurements of magnesite at high P and T from $X_{NaCl} = 0$ to halite saturation and can be utilized in new calculations to constrain the carbon cycle. The experimental data also provides a new mechanism responsible for the enhancement of carbonate dissolution in NaCl fluids.

2 Figures

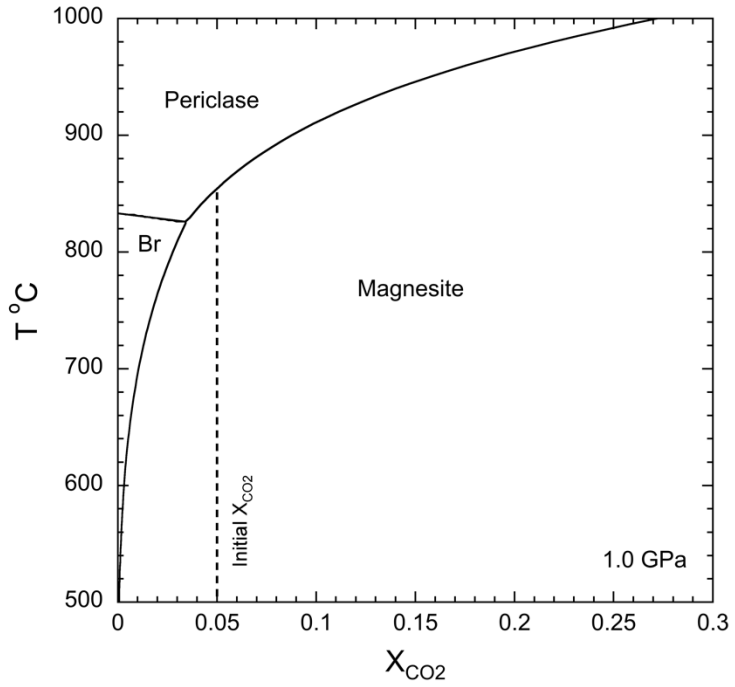

Figure. 2.1. Temperature - X_{CO2} section showing phase relations in the system MgO-H_2O-CO_2 at 1 GPa. At all T, brucite (br) or periclase are stable with pure H_2O fluids. A fluid in equilibrium with only magnesite must have CO_2 mole fraction (X_{CO2}) greater than the magnesite + H_2O = brucite + CO_2 or 2) magnesite = periclase + CO_2 phase boundaries. The dashed vertical curve shows the initial X_{CO2} used in the present study (see text).

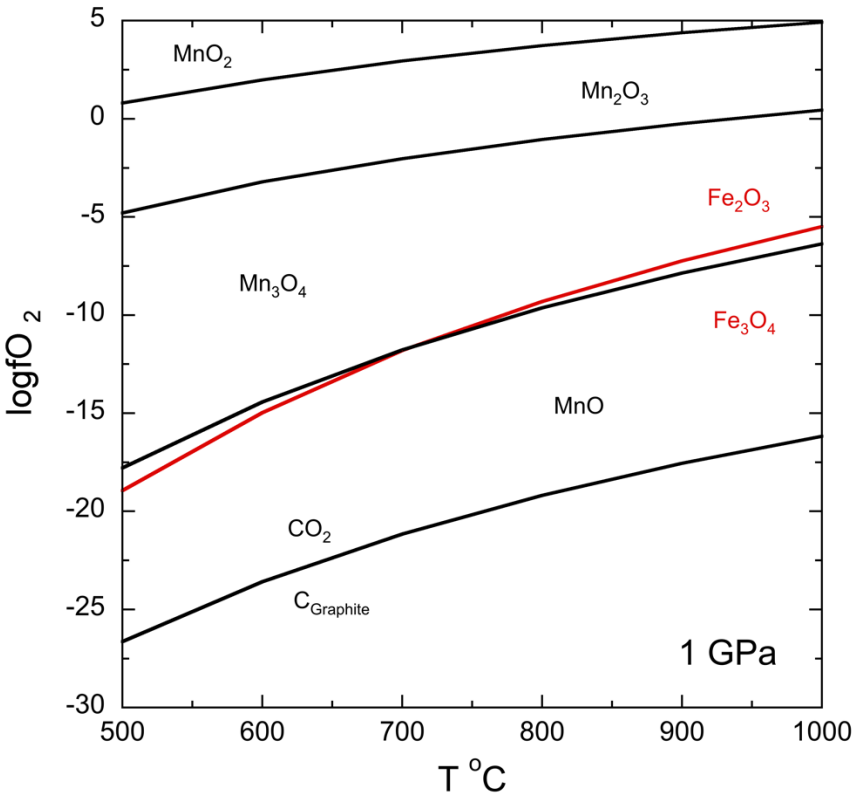

Figure. 2.2. Plot showing log f_{O2} vs temperature at 1 GPa comparing relevant manganese oxide buffering reactions, the hematite-magnetite buffer (HM) and the graphite-CO_2 buffer (CCO).

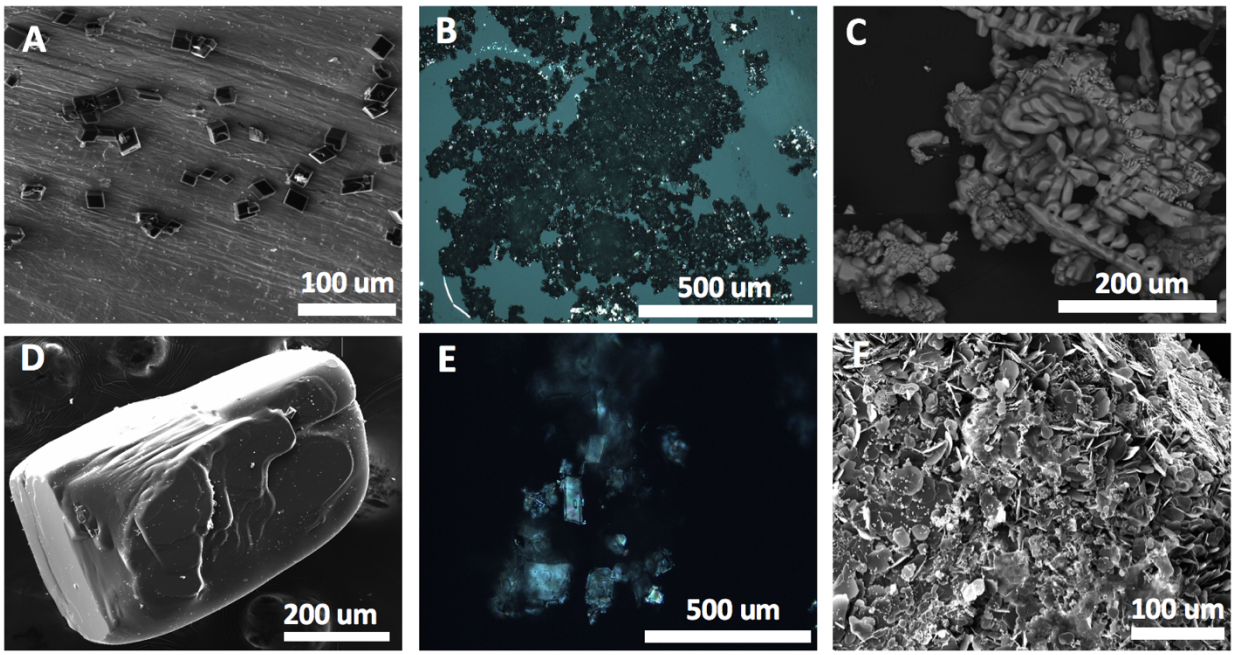

Figure. 2.3. Scanning electron microscope (SEM) and high-dispersion oil microscopy of products of selected experiments. (A) vapor transported crystals from run DC_67 (Table 2.1), 600 °C at X_{NaCl} = 0.00 at X_{CO2} = 0.05. (B) Oil immersion microscopy photograph. Polarized light viewed under high-dispersion oil 1.5400, run number DC_65 (Table 2.1), 800 °C at X_{NaCl} = 0.594 at X_{CO2} = 0.05. Precipitation of quench magnesite quench in NaCl demonstrated disordered masses of birefringent carbonate. (C) NaCl displaying an interesting hopper texture with magnesite outlining the NaCl. This texture is typical where magnesite solubility is high. (D) Recrystallized solution polished magnesite crystal from run DC_2 (Table 2.1), 800 °C at X_{NaCl} = 0.00 at X_{CO2} = 0.05. Secondary electrons. (E) Oil immersion microscopy photo. Polarized light view of grain mount in high-dispersion oil (n=1.5400), run DC_66 (Table 2.1), 800 °C at X_{NaCl} = 0.601 at X_{CO2} = 0.05. Large, recrystallized magnesite crystal from powdered magnesite approximately 110 x 30 microns in length. The crystal and fluid inclusion bearing NaCl and vapor bubble indicate growth during the run. (F) Incongruent dissolution of magnesite to brucite, run DC_51 (Table 2.1), 700 °C at X_{NaCl} = 0.199 at X_{CO2} = 0.00. The results indicate that suppression of H_2O activity alone is insufficient to prevent brucite formation in initially CO_2-free fluids.

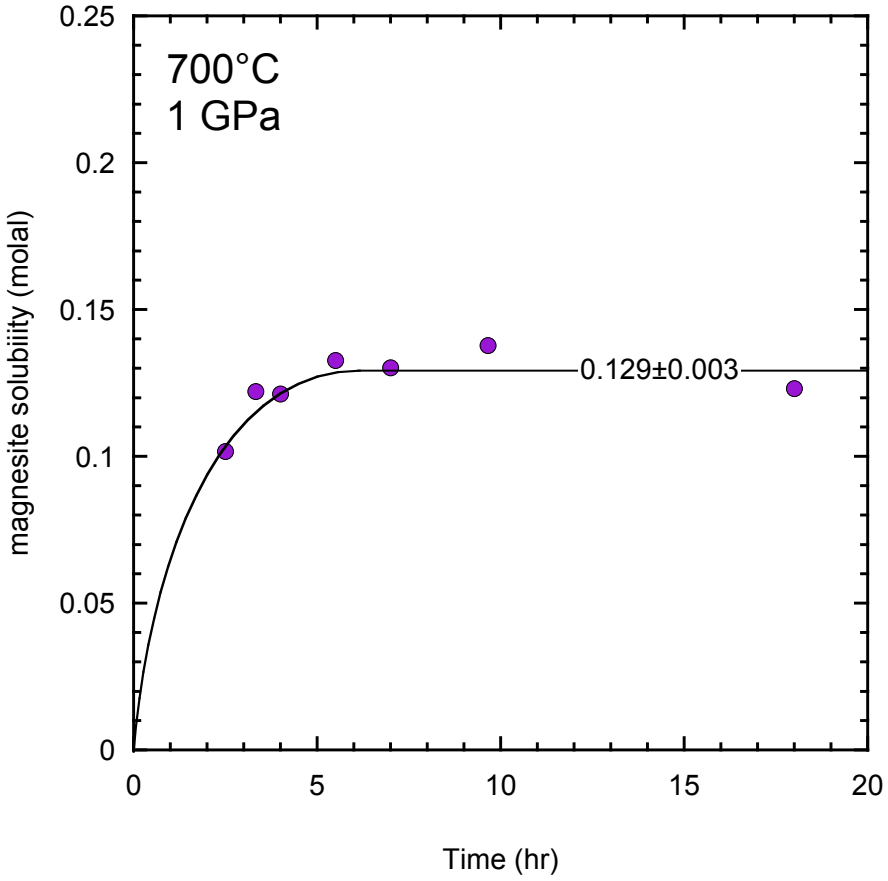

Figure. 2.4. Variation in magnesite solubility with time at 1.0 GPa, 700 °C, X_{NaCl} = 0.15 and X_{CO2} = 0.05. The dashed line represents the average solubility in runs > 3.15 hr, which are interpreted to be at equilibrium.

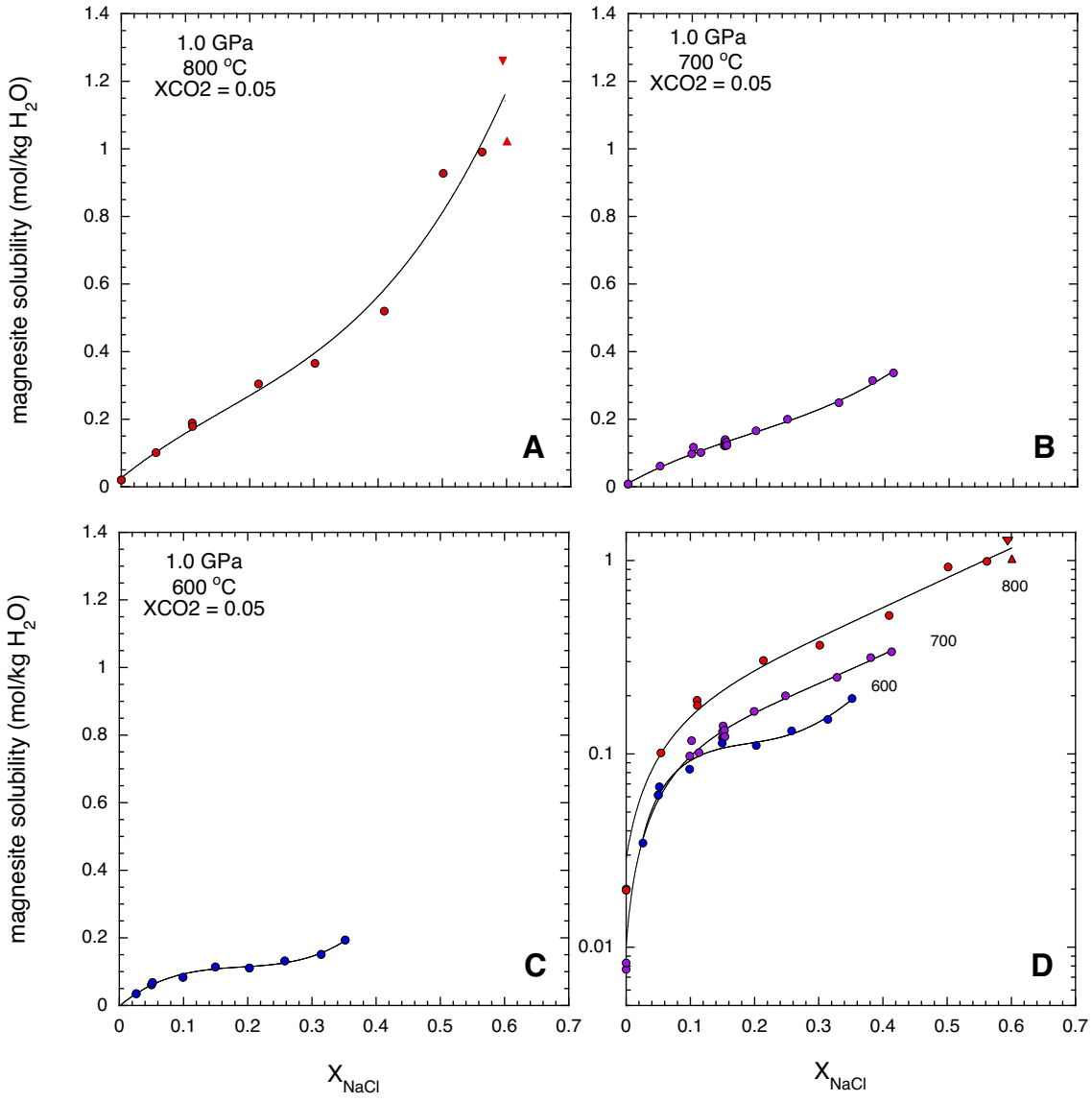

Figure. 2.5. Experimentally determined $MgCO_3$ solubility (in moles $MgCO_3$ dissolved per kg H_2O) at 1.0 GPa, as a function of X_{NaCl}. Triangles represent experiments DC_65 and DC_66 where runs using powered magnesite to bracket solubility.

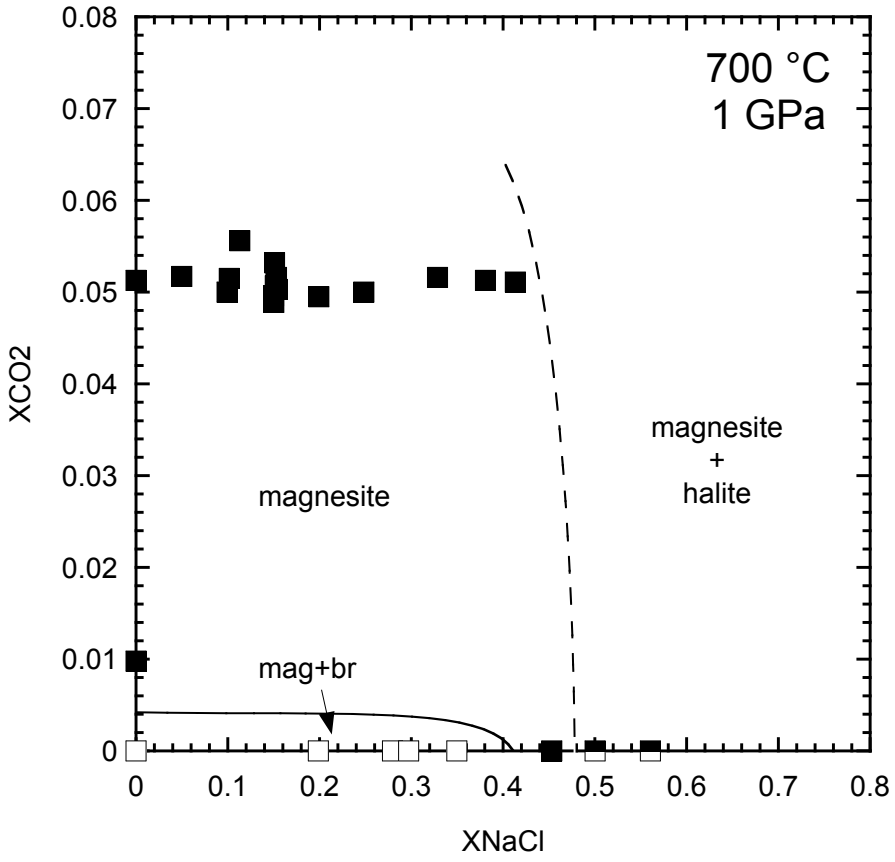

Figure. 2.6. Phase relations in the system MgO-H_2O-CO_2-NaCl at 700 °C, 1.0 GPa, as constrained by experimental results (Table 2.1). Halite saturation was identified by a rounded halite crystal which formed during the run. This was easily distinguishable from halite crystal which form upon the opening and drying of the experimental capsule, which were skeletal to cubic and substantially smaller.

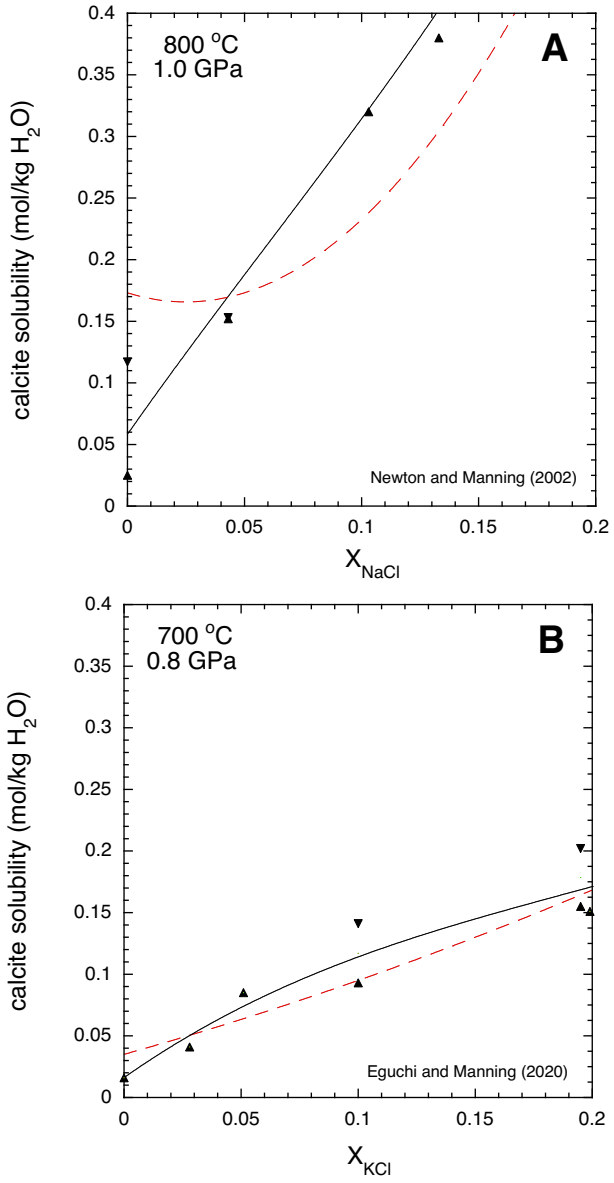

Figure. 2.7. Experimentally determined calcite solubility as a function of alkali halide mole fraction. (A) Data from Newton and Manning (2002); (B) data from Eguchi and Manning (2022). Solid black lines represent a 3rd order polynomial fit and dashed red lines represent the 2nd order fit given by least-squares regressions of the salt-undersaturated solubilities published in each study. At all experimental conditions the 2nd order fit overpredicts carbonate solubility at low X_{salt} consistent with a change in speciation in the fluid phase as salt concentrations increases.

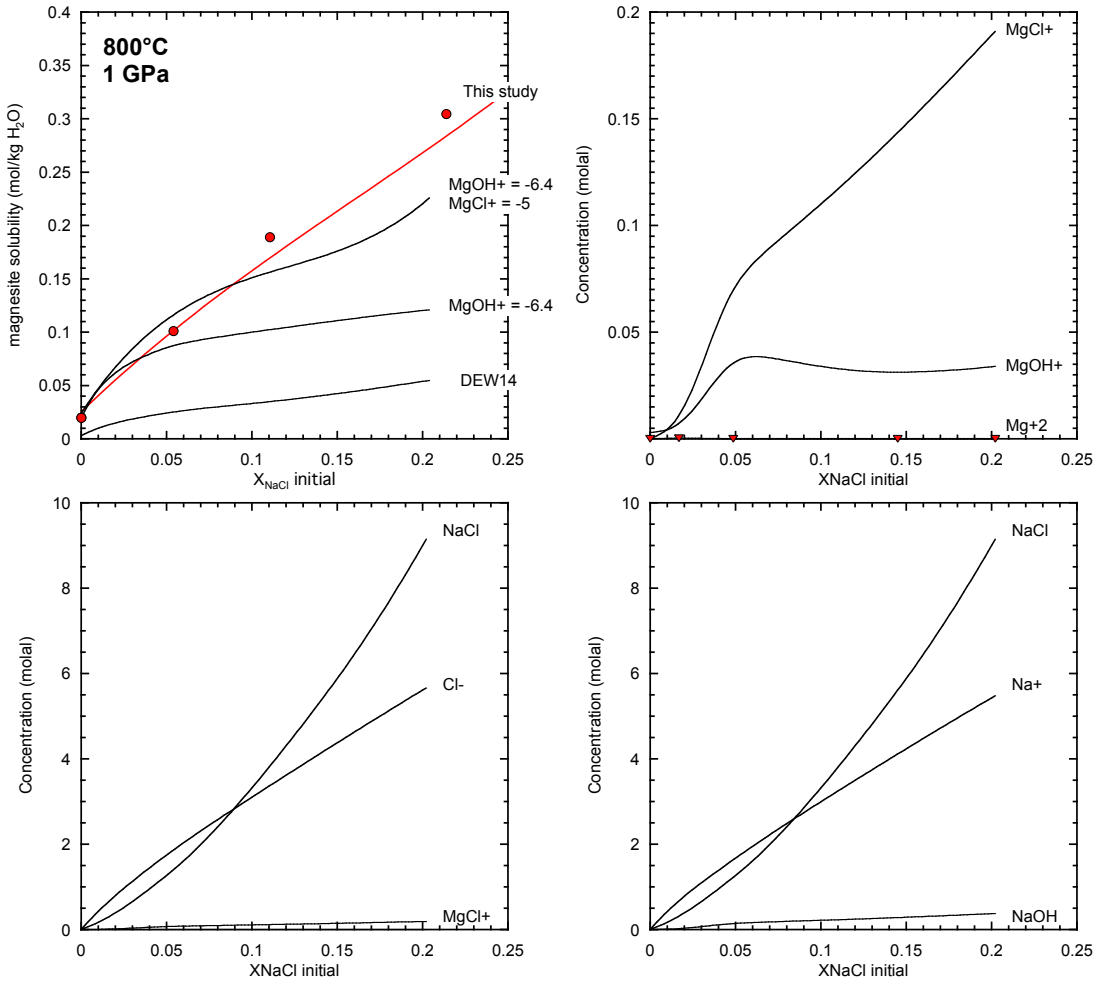

Figure. 2.8. Experimental solubility data at 1.0 GPa and 800 °C compared to aqueous species predicted by the aqueous speciation-solubility code EQ3 (Wolery, 1992), adapted to include equilibrium constants calculated with the Deep Earth Water (DEW) model (Sverjensky et al. 2014). (A) Comparison of this studied data to species predicted by the Deep Earth Water model. (B) The concentration of the three most abundant Mg species predicted by the modified logK values presented in panel A. (C and D) Predicted change in abundances of Cl and Na species, respectively, with NaCl concentration, using $\log K_{MgCl^+} = -5$ and $\log K_{MgOH^+} = -6.4$. The two panels demonstrate the correlation between the inflection point of magnesite solubility with the change from Na^+ and Cl^- predominance to $NaCl_{aq}$ predominance.

Table. 2.1. Results of magnesite solubility experiments at 1.0 GPa.

Expt. No.	Temp °C	Duration hr	NaCl mg	OAD mg	H_2O mg	H_2O_{tot} mg	X_{CO2}	X_{NaCl}	wt change µg	$MgCO_3$ molal	Buffer	Notes
DC_95	600	5.00	2.5101	5.2319	25.7523	27.2475	0.051	0.026	79.5	0.0346(06)	MW	
DC_68	600	6.00	4.1394	4.4785	21.6806	22.9605	0.050	0.050	118.7	0.0613(07)	MW	
DC_81	600	3.00	4.7562	4.9946	23.9780	25.4054	0.051	0.052	144.9	0.0676(06)	MW	
DC_69	600	6.00	7.3555	3.9687	18.3803	19.5146	0.050	0.010	137.2	0.0833(08)	MW	
DC_96	600	5.00	11.5342	4.4385	17.6731	18.9416	0.054	0.150	176.7	0.1106(08)	MW	
DC_70	600	7.00	12.7918	3.4125	13.5555	14.5307	0.050	0.203	139.2	0.1137(12)	MW	
DC_99	600	5.50	16.7644	3.4888	12.8873	13.8844	0.050	0.258	154.1	0.1316(14)	MW	
DC_72	600	6.00	17.0251	2.9178	9.7845	10.6184	0.050	0.314	135.0	0.1508(13)	MW	
DC_103	600	6.00	20.3075	3.0683	9.7768	10.6537	0.049	0.352	173.6	0.1933(19)	MW	
DC_38	700	22.00	0.0000	0.00	31.4496	31.4496	0.000	0.000	260.1	-	M	mag+br
DC_51	700	70.00	15.6549	0.00	19.4624	19.4624	0.000	0.199	314.0	-	M	mag+br
DC_52	700	28.00	19.2289	0.00	15.2642	15.2642	0.000	0.280	296.9	-	M	mag+br
DC_53	700	17.50	20.4308	0.00	14.8957	14.8957	0.000	0.297	737.0	-	M	mag+br
DC_54	700	27.00	22.2803	0.00	12.7818	12.7818	0.000	0.345	295.5	-	M	mag+br
DC_56	700	27.00	20.7073	0.00	7.7006	7.7006	0.000	0.453	207.6	0.3198(14)	M	mag
DC_47	700	not recorded	26.7625	0.00	8.2366	8.2366	0.000	0.500	207.1	0.2982(27)	M	mag+hal
DC_49	700	9.75	32.0416	0.00	7.7434	7.7434	0.000	0.561	205.9	0.3154(24)	M	mag+hal
DC_43	700	5.00	0.0000	1.1471	32.6420	32.9700	0.010	0.000	23.1	0.0083(06)	M	
DC_15	700	6.00	0.0000	3.3506	16.7684	17.7260	0.051	0.000	11.5	0.0077(17)	M	
DC_55	700	6.50	4.2640	4.7655	22.2933	23.6552	0.052	0.050	121.9	0.0611(08)	M	
DC_16	700	4.00	7.4886	4.0743	18.6389	19.8034	0.050	0.010	162.6	0.0974(09)	HM	
DC_77	700	3.00	8.4793	4.6210	20.4311	21.7518	0.052	0.102	214.6	0.1170(07)	MW	
DC_80	700	6. 00	9.0100	4.7617	19.0191	20.3800	0.056	0.113	174.5	0.1015(08)	MW	
DC_78	700	2.50	12.197	4.3877	18.3472	19.6012	0.051	0.153	168.0	0.1017(07)	M	ts
DC_87	700	3.25	11.8890	4.2708	18.0337	19.2543	0.051	0.153	198.2	0.1221(06)	M	ts
DC_79	700	4.00	12.2535	4.6486	18.5933	19.9212	0.053	0.151	203.8	0.1213(08)	M	ts
DC_88	700	5.50	11.9582	4.3390	17.8989	19.1390	0.052	0.153	214.8	0.1331(08)	M	ts
DC_84	700	7.00	11.7904	4.1356	18.2026	19.3845	0.049	0.150	212.8	0.1302(05)	M	ts
DC_86	700	9.75	11.6976	4.1637	18.0648	19.2547	0.050	0.150	226.4	0.1395(08)	M	ts
DC_89	700	18.00	12.1074	4.2652	18.1010	19.3200	0.050	0.154	200.6	0.1231(10)	M	ts
DC_98	700	4.00	14.2576	3.8178	15.4891	16.5802	0.050	0.199	231.9	0.1659(08)	MW	
DC_83	700	5.00	16.6878	3.6157	13.5083	14.5417	0.050	0.248	245.0	0.1999(10)	MW	
DC 104	700	6.00	19.0358	3.2166	10.1547	11.0740	0.052	0.329	232.4	0.2490(15)	MW	
DC_57	700	5.00	19.7923	2.8723	8.2735	9.0944	0.051	0.381	241.2	0.3145(17)	MW	
DC_105	700	5.50	23.0104	3.0630	8.3122	9.1876	0.051	0.413	261.2	0.3372(16)	MW	
DC_1	800	96.00	0.0000	20.0261	19.7553	25.4788	0.183	0.000	43.0	0.0200(05)	HM	
DC_22	800	19.45	0.0000	3.2652	16.6415	17.5747	0.050	0.000	29.1	0.0197(07)	M	
DC_3	800	3.00	4.2886	4.5528	20.5264	21.8276	0.053	0.054	186.3	0.1012(04)	HM	
DC_4	800	4.00	7.6495	4.1349	16.5958	17.7775	0.055	0.111	283.6	0.1892(08)	HM	
DC_5	800	5.00	13.0147	3.4780	12.7617	13.7557	0.053	0.214	343.2	0.3046(12)	HM	
DC_12	800	1.50	16.8917	3.0577	10.3114	11.1853	0.051	0.302	344.3	0.3651(13)	HM	
DC_58	800	5.75	20.6246	2.6912	7.6184	8.3875	0.050	0.410	367.8	0.5201(09)	MW	
DC_59	800	6.75	23.2031	2.4835	5.6938	6.4036	0.050	0.501	500.6	0.9272(30)	MW	
DC_60	800	6.75	25.7213	2.4746	4.7664	5.4736	0.050	0.562	450.8	0.9769(35)	MW	
DC_66	800	6.00	26.6656	2.4563	4.0554	4.7574	0.051	0.601	410.4	1.0232(02)	MW	no mag
DC_65	800	5.00	26.5538	2.4047	4.2149	4.9022	0.050	0.594	521.0	1.2605(03)	MW	mag

Explanation: Weights of NaCl, Oxalic acid dihydrate, and H_2O are initial values prior to experiment; H_2O_{tot} is sum of H_2O added and H_2O derived from breakdown of oxalic acid dihydrate. Abbreviations: OAD, oxalic acid dihydrate; mag, magnesite; br, brucite; hal, halite; ts, time series. Buffers: M, initially dry Mn oxides; MW, Mn oxides + H_2O; HM, initially dry hematite + magnetite.

2. References

Aranovich, L. Y., & Newton, R. C. (1996). H2O activity in concentrated NaCl solutions at high pressures and temperatures measured by the brucite-periclase equilibrium. Contributions to Mineralogy and Petrology, 125(2), 200-212.

Burton, M. R., Sawyer, G. M., & Granieri, D. (2013). Deep carbon emissions from volcanoes. Reviews in Mineralogy and Geochemistry, 75(1), 323-354.

Brooker, R., Holloway, J. R., & Hervig, R. (1998). Reduction in piston-cylinder experiments: The detection of carbon infiltration into platinum capsules. American Mineralogist, 83(9-10), 985-994.

Bohlen, S. R. (1984). Equilibria for precise pressure calibration and a frictionless furnace assembly for the piston-cylinder apparatus. Neues Jahrbuch für Mineralogie, Monatshefte, 404-412.

Caciagli, N. C., & Manning, C. E. (2003). The solubility of calcite in water at 6–16 kbar and 500–800 C. Contributions to Mineralogy and Petrology, 146(3), 275-285.

Chou, I. M., (1978) Calibration of oxygen buffers at elevated P T using the hydrogen fugacity sensor. American lite. Mineralogist, 63, 690–703.

Dasgupta, R., & Hirschmann, M. M. (2010). The deep carbon cycle and melting in Earth's interior. Earth and Planetary Science Letters, 298(1-2), 1-13.

Ellis, A. J. (1959). The solubility of calcite in carbon dioxide solutions. American Journal of Science, 257(5), 354-365.

Eguchi, J., Li, Y., & Manning, C. E. (2020). Experimental Determination of Calcite Solubility in H2O-KCl-NaCl-LiCl Solutions at 700° C and 8 kbar. Carbon in Earth's Interior, 245-257.

Eugster , H. P., & Wones , D. R., (1962) Stability relations of the ferruginous biotite, annite. Petrol. 3, 82-125.

Facq, S., Daniel, I., Montagnac, G., Cardon, H., & Sverjensky, D. A. (2016). Carbon speciation in saline solutions in equilibrium with aragonite at high pressure. Chemical Geology, 431, 44-53.

Fein, J. B., & Walther, J. V. (1987). Calcite solubility in supercritical CO2- H2O fluids. Geochimica et Cosmochimica Acta, 51(6), 1665-1673.

Ferrando, S. (2012). Mg-metasomatism of metagranitoids from the Alps: genesis and possible tectonic scenarios. Terra Nova, 24(6), 423-436.

Falk, E. S., & Kelemen, P. B. (2015). Geochemistry and petrology of listvenite in the Samail ophiolite, Sultanate of Oman: Complete carbonation of peridotite during ophiolite emplacement. Geochimica et Cosmochimica Acta, 160, 70-90.

Helgeson, H. C. (1969). Thermodynamics of hydrothermal systems at elevated temperatures and pressures. American journal of science, 267(7), 729-804.

Helgeson, H. C., & Kirkham, D. H. (1976). Theoretical prediction of thermodynamic properties of aqueous electrolytes at high pressures and temperatures. III. Equation of state for aqueous species at infinite dilution. Am. J. Sci.;(United States), 276(2).

Huang, F., & Sverjensky, D. A. (2019). Extended Deep Earth Water Model for predicting major element mantle metasomatism. Geochimica et Cosmochimica Acta, 254, 192-230.

Isshiki, M., Irifune, T., Hirose, K., Ono, S., Ohishi, Y., Watanuki, T., ... & Sakata, M. (2004). Stability of magnesite and its high-pressure form in the lowermost mantle. Nature, 427(6969), 60-63.

Jarrard, R. D. (2003). Subduction fluxes of water, carbon dioxide, chlorine, and potassium. Geochemistry, Geophysics, Geosystems, 4(5).

Kaminsky, F. V., Wirth, R., & Schreiber, A. (2013). Carbonatitic inclusions in deep mantle diamond from Juina, Brazil: new minerals in the carbonate-halide association. The Canadian Mineralogist, 51(5), 669-688.

Kelemen, P. B., & Manning, C. E. (2015). Reevaluating carbon fluxes in subduction zones, what goes down, mostly comes up. Proceedings of the National Academy of Sciences, 112(30), E3997-E4006.

Macris, C. A., Newton, R. C., Wykes, J., Pan, R., & Manning, C. E. (2020). Diopside, enstatite and forsterite solubilities in H2O and H2O-NaCl solutions at lower crustal and upper mantle conditions. Geochimica et Cosmochimica Acta, 279, 119-142.

Manning, C. E., & Boettcher, S. L. (1994). Rapid-quench hydrothermal experiments at mantle pressures and temperatures. American Mineralogist, 79(11-12), 1153-1158.

Manning, C. E. (2013). Thermodynamic modeling of fluid-rock interaction at mid-crustal to upper-mantle conditions. Reviews in Mineralogy and Geochemistry, 76(1), 135-164.

Menzel, M. D., Garrido, C. J., & Sánchez-Vizcaíno, V. L. (2020). Fluid-mediated carbon release from serpentinite-hosted carbonates during dehydration of antigorite-serpentinite in subduction zones. Earth and Planetary Science Letters, 531, 115964.

Newton, R. C., & Manning, C. E. (2002)a. Solubility of enstatite+ forsterite in H2O at deep crust/upper mantle conditions: 4 to 15 kbar and 700 to 900 C. Geochimica et Cosmochimica Acta, 66(23), 4165-4176.

Newton, R. C., & Manning, C. E. (2002). Experimental determination of calcite solubility in H2O-NaCl solutions at deep crust/upper mantle pressures and temperatures: Implications for metasomatic processes in shear zones. American Mineralogist, 87(10), 1401-1409.

Newton, R. C., & Manning, C. E. (2006). Solubilities of corundum, wollastonite and quartz in H2O–NaCl solutions at 800 C and 10 kbar: interaction of simple minerals with brines at high pressure and temperature. Geochimica et Cosmochimica Acta, 70(22), 5571-5582.

Pan, D., Spanu, L., Harrison, B., Sverjensky, D. A., & Galli, G. (2013). Dielectric properties of water under extreme conditions and transport of carbonates in the deep Earth. Proceedings of the National Academy of Sciences, 110(17), 6646-6650.

Plank, T., & Manning, C. E. (2019). Subducting carbon. Nature, 574(7778), 343-352.

Sapienza, G. T., Scambelluri, M., & Braga, R. (2009). Dolomite-bearing orogenic garnet peridotites witness fluid-mediated carbon recycling in a mantle wedge (Ulten Zone, Eastern Alps, Italy). Contributions to Mineralogy and Petrology, 158(3), 401-420.

Scambelluri, M., & Philippot, P. (2001). Deep fluids in subduction zones. Lithos, 55(1-4), 213-227.

Sverjensky, D. A., Harrison, B., & Azzolini, D. (2014). Water in the deep Earth: The dielectric constant and the solubilities of quartz and corundum to 60 kb and 1200 C. Geochimica et Cosmochimica Acta, 129, 125-145.

Tropper, P., & Manning, C. E. (2007). The solubility of corundum in H2O at high pressure and

temperature and its implications for Al mobility in the deep crust and upper mantle. Chemical Geology, 240(1-2), 54-60.

Wolery, T. J. (1992). EQ3/6, a software package for geochemical modeling of aqueous systems: package overview and installation guide (version 7.0) (No. UCRL-MA--110662-PT. 1). Lawrence Livermore National Lab

Chapter 3. Experimental investigation of quartz solubility in H_2O-CO_2 fluids at 10 kbar, 500–800 °C: implications for aqueous speciation and silica mobility

Abstract

The dissolution and transport of SiO_2 by H_2O plays a central role in fluid-mediated mass transfer in Earth's crust. At elevated pressures (P) and temperatures (T), dissolved SiO_2 can reach over 10 wt% of a quartz-saturated metasomatizing fluid. However, crustal fluids are commonly mixtures of H_2O, CO_2 and salts, which can have complex effects on solute dissolution and transport. Critical to quantifying silica dissolution is understating its interactions with the H_2O component of any mixed crustal fluid. Walther and Orville (1983) developed novel experimental methods to investigate the nature of silica hydration and solvation by H_2O, which can explicitly be accounted for by writing the reaction:

$$\underset{\text{quartz}}{SiO_{2,s}} + nH_2O = \underset{\text{hydrated monomer}}{Si(OH)_4 \cdot (n-2)H_2O_{(aq)}}$$

where n is the "hydration number", which corresponds to the total number of H_2O molecules consumed in the transfer of SiO_2 from minerals to the fluid. They concluded that n = 4 at investigated P and T. Since their findings, the value of n has been a matter of debate, with alternate proposals of n = 3.5 (Shmulovich et al. 2006) and 2 (Akinviev and Diamond 2009). Using an improved thermodynamic framework accounting for silica polymerization and H_2O activity, Newton and Manning (2009) supported the original finding of n = 4. I conducted new quartz solubility experiments in H_2O-CO_2 fluids using hydrothermal piston-cylinder methods at

10 kbar, 800-500 °C, and X_{CO2} = 0.0 to 0.5, to further investigate the nature of silica hydration. H_2 fugacity was buffered by hematite-magnetite equilibrium. Quartz solubility declines exponentially with rising CO_2 at all temperatures investigated. I find that n cannot be a constant independent of P and T, and that it increases from 4.1 to 7.3 as temperature declines from 800 to 500 °C at 10 kbar. I calibrated a simple exponential relationship between the dielectric constant of pure water (ε_{H2O}) and n. Our new model accurately reproduces all previous experimental results from 500 – 800 °C and 0.3 to 10 kbar. The apparently constant values of n in previous studies arise from the narrow range of H_2O dielectric constant investigated. The results provide a foundation for thermodynamically robust prediction of silica mass transfer in crustal metasomatic systems.

3.1 Introduction

Earth's endowment of water (H_2O) makes it unique compared to the other terrestrial planets in our solar system. In addition to its important role in biology and climate, H_2O also influences a wide array of geologic processes. It facilitates earth's changing topography, triggers energetic volcanic eruptions, mediates certain earthquake activity, controls the concentration of many of our most economically important mineral resources, and has profound structural and rheological effects within the crust and mantle (Getsinger et al., 2013; Wang et al., 2020). Where water is present in the crust and mantle, it acts as a powerful solvent for rock-forming elements. At these conditions of elevated pressure and temperature, the most soluble rock component in H_2O is silica, which can reach over 10 wt% in certain settings (e.g., Manning 2018).

In order to understand aqueous silica transportation by hydrothermal fluids, a quantitative understanding of its dissolution in H_2O is required. The simplest way of characterizing the chemistry of dissolved silica is through the study of quartz solubility, which has been an important subject of experimental investigation since the pioneering work of Kennedy (1944, 1950) three quarters of a century ago. Since then, numerous studies have demonstrated that key factors influencing the amount and speciation of aqueous silica are temperature (T), pressure (P), and fluid composition. In general, H_2O saturated with quartz will contain increasing dissolved silica as pressure and temperature rise, or as pH increases (Anderson and Burnham 1965; Manning 1994; Aranovich et al., 2020). The higher concentrations arise in part from the polymerization (Newton and Manning 2008) and/or deprotonation of aqueous silica (Aranovich et al., 2020).

On the molecular scale, the transfer of silica from a mineral, e.g. quartz, into H_2O can be understood as a sequence of reactions at the mineral surface, in which Si-O bonds are successively broken by H_2O (e.g., Lasaga and Gibbs, 1990). In the simplest case, the result is a hydrated silica monomer, $Si(OH_4)$, in which each of the four oxygens bonded to a silicon is also bonded to a hydrogen atom, forming four hydroxyl groups that tetrahedrally coordinate the silicon atom. In addition to these four hydroxyl groups, the hydrated silica monomer is held in solution via its interactions with H_2O molecules which form a solvation shell around the silica ion. Silica solvation can be visualized through Gurney's (1962) co-sphere model of hydration, applied to a neutral solute. The model assigns zonation of water molecules surrounding a solute. Zone 1 corresponds to highly ordered H_2O molecules which are statistically associated with the solute in solution. The subsequent zones increase in disorder until exhibiting the bulk water normal structure (see Gurney, 1962).

The silica monomer derived from dissolving quartz gains H and O from water as it is transferred to the solvent, which can explicitly be accounted for by writing:

$$\mathrm{SiO_{2,s}} + \mathrm{nH_2O} = \mathrm{Si(OH)_4} \cdot (\mathrm{n} - 2)\mathrm{H_2O} \qquad (3.1)$$

quartz solvated and hydrated monomer

where n is the "hydration number", which corresponds to the total number of H_2O molecules consumed in the transfer of SiO_2 from minerals to the fluid: 2 H_2O consumed in producing the

hydrated silica monomer, and n-2 molecular H_2O in a solvation shell and subscript s refers to the crystalline phase.

Using a standard state for quartz of unit activity of the pure phase at any P and T, the equilibrium constant for Eq. (3.1) is:

$$K_{qm} = \frac{a_m}{a_{H2O}^n} \tag{3.2}$$

where a denotes activity and m stands for the solvated and hydrated monomer. Taking logarithms and rearranging leads to

$$\log a_m = n \log a_{H2O} + \log K_{qm} \tag{3.3}$$

Equation (3.3) shows that, at a given P and T, the activity of the monomer in mixed fluids is a function of the hydration number, a_{H2O}, and K_{qm}. If at this P and T n is a constant independent of a_{H2O}, then Eq. (3.3) is the equation for a straight line with slope n and an intercept of $\log K_{qm}$. Equation (3.3) illustrates that the hydration of silica monomer can be determined by conducting multiple experiments at constant P and T and varying the activity of H_2O.

Numerous early studies investigated the changes in quartz solubility with addition of solvent components to H_2O (e.g., Sommerfeld 1967; Novgorodov 1975; Anderson and Burnham 1967; Fournier et al., 1982 Red'kin and Chevichelova r1988). While solubility changes may be quite complex depending on the diluent, it was found that addition of simple molecular gases

(e.g., CO_2, Ar) systematically decreases quartz solubility. Walther and Orville (1983) developed experimental methods to study quartz solubility in H_2O-CO_2 and H_2O-Ar fluids at metamorphic P and T to quantify the nature of silica hydration and solvation by H_2O. At the time there was a poor understanding of H_2O activity in mixed fluids and of silica polymerization and the activities of relevant species. This required Walther and Orville (1983) to assume all dissolved SiO_2 was present as the silica monomer and that H_2O-CO_2 mixed ideally (i.e. the activity of H_2O was equal to its mole fraction, X). With these crude assumptions they found that at a range of P and T, their data and those of previous workers were consistent with a constant n of 4.

Subsequent studies modified and extended the results of Walther and Orville while retaining their assumptions. Shmulovich et al. (2006) concluded that n = 3.5, whereas Akinviev and Diamond (2009) argued that n = 2. However, as seen in Eq. (1.3), an accurate prediction of silica hydration explicitly depends on the activity of the silica species (i.e. monomer, dimer… etc) and an accurate H_2O-CO_2 mixing model. Newton and Manning (2009) improved the thermodynamic framework for silica dissolution by using updated models for H_2O and silica activity. The ability of silica to polymerize (e.g., Wendltant and Glemser 1963; Zhang and Frantz 2000, Zotov and Keppler, 2000, 2002; Newton and Manning 2002 ,2003, 2008) helps explain its high solubility in H_2O at crustal and mantle conditions. Equation (3.2) can be modified to account for polymerization using the generalized reaction:

$$y\mathrm{SiO}_{2,s} + n\mathrm{H}_2\mathrm{O} = (\mathrm{SiO}_2)_y \cdot n_y\mathrm{H}_2\mathrm{O}_{(aq)} \qquad 3.4$$

quartz

where y is the number of Si atoms in a solute polymer, n denotes the hydration number, and subscripts s and aq refer to the crystalline and aqueous phases, respectively. Again, assuming pure quartz, the equilibrium constant for reaction 3.4,

$$K_{qp} = \frac{a_{(SiO_2)_y \cdot nH_2O_{(aq)}}}{a^n_{H2O}} \tag{3.5}$$

is similar to Eq. (3.2) and implies that the activity of any given silica polymer in solution depends on H_2O activity and hydration number.

Newton and Manning (2009) conducted high-precision piston-cylinder experiments at 800 °C and 10 kbar in fugacity-controlled H_2O-CO_2 fluids. They used a thermodynamic mixing model for silica species (Newton and Manning, 2003, 2004) and H_2O-CO_2 (Aranovich and Newton, 1999) to constrain activities of silica and H_2O. After evaluation of their data and reevaluation of previous solubility measurements in CO_2-H_2O solutions, they concluded that, for the silica monomer, n = 4 independent of P and T, supporting Walther and Orville's (1984) original finding. In response to these studies, numerous density-based quartz solubility models have assumed a fixed hydration state (Akinfiev and Diamond, 2009; Newton and Manning, 2016; Brooks and Steele-MacInnis, 2019).

The finding of a fixed hydration number independent of P and T is surprising. This can be seen from the Born equation (Born, 1920), which links the Gibbs free energy of ion solvation ($\Delta\overline{G}^{\circ}_{solvation}$) to the dielectric constant of pure H_2O (ε_{H2O}) via:

$$\Delta\overline{G}^{\circ}_{solvation} = \omega\left(\frac{1}{\varepsilon_{H2O}} - 1\right) \quad (3.6)$$

where ω represents the conventional Born solvation coefficient of the ion. It has been shown that Eq. (3.6) is also applicable to neutral aqueous species, for which ω is a constant independent of P and T (e.g., Walther and Helgeson 1977; McKenzie and Helgeson, 1982; Sverjensky et al. 1997; 2014). Thus, $\Delta\overline{G}^{\circ}_{solvation}$ of a neutral species depends solely on ε_{H2O}. Because ε_{H2O} varies strongly with P and T, reflecting changes in the shielding strength of H_2O dipoles, the energetics of solvation should scale with ε_{H2O} (and P and T), and – to the extent that hydration number reflects solute solvation – the value of n ought to be variable as well.

This problem motivates additional research into the nature of silica hydration. Analysis of previous work was mostly conducted over a narrow range in the dielectric constant of water despite the span of pressure and temperature investigated. A better understanding of the solvation of aqueous silica can be attained from additional experiments over a broader range of water dielectric conditions. Here, I conducted high precision quartz solubility measurements in fugacity-controlled H_2O-CO_2 solutions at 10 kbar from 500-800 °C, which corresponds to ε_{H2O} of 12 to 24. The results allow a more detailed examination of silica solvation than has previously been possible. Additionally, this work provides a foundation to explore solvation state as a function of P, T, and fluid composition, and to derive, for the first time, correlations between solvation and the dielectric constant and density of H_2O. These results establish a new simplified empirical model, which allows accurate predictions of silica in CO_2-H_2O solutions over a range P and T.

3.2 Methods

Hydrothermal piston-cylinder experiments were performed on the solubility of quartz in H_2O-CO_2 fluids at high pressure and temperature. The methods of Manning (1994) and Newton and Manning (2000, 2009) were generally followed, with modifications as described below.

3.2.1. Oxygen fugacity considerations

Experiments on quartz solubility in CO_2-bearing H_2O require special measures to maintain desired solvent composition. Hydrous oxalic acid (OAD: $(COOH)_2 \cdot 2H_2O$) was used as a CO_2 source to generate fluids on the H_2O-CO_2 join. During initial heating of an experiment, OAD breaks down to produce CO_2, H_2O and H_2 through the reaction

$$(COOH)_2 \cdot 2H_2O \rightarrow 2CO_2 + 2H_2O + H_2 \quad (3.7)$$

The H_2 produced in Eq. (3.7) is a complication in experiments where CO_2 is a desired fluid component. In the absence of any external control on oxidation state, the H_2 reacts with CO_2 at the conditions of the present study, leading to graphite precipitation via:

$$CO_2 + 2H_2 \rightarrow C + 2H_2O \quad (3.8)$$

Graphite

(e.g., Brooker et al. 1998), for which the equilibrium constant Kcco is

$$K_{cco} = \frac{a_{H2O}^2}{a_{CO2} f_{H2}^2} \quad (3.9)$$

To prevent the reduction of CO_2 to graphite, low fugacity of hydrogen (i.e., high fugacity of oxygen) must be maintained over the duration of an experiment. In the present study, this was achieved using conventional double-capsule methods. At experimental conditions, Pt is permeable to H_2 but Au is not (Chou et al. 1978; Eugster and Wones 1962). Accordingly, a Pt inner capsule is used in combination with an Au outer capsule, along with a chemical system capable of controlling H_2 fugacity. The inner capsule, containing the CO_2-H_2O-bearing fluid phase and quartz, was placed inside an outer capsule containing hematite (Fe_2O_3) and H_2O. During the experiment, H_2 diffusion from the inner capsule causes hematite reduction to magnetite (Fe_3O_4). While both hematite and magnetite are present, the equilibrium

$$3Fe_2O_3 + H_2 = 2Fe_3O_4 + H_2O \tag{3.10}$$

holds. The equilibrium constant for Eq. (3.10), K_{hm}, is:

$$K_{hm} = \frac{a_{H_2O}\, a_{Fe_2O_3}^2}{f_{H_2} a_{Fe_3O_4}} \tag{3.11}$$

Adopting standard states of unit activity for pure minerals, H_2O and CO_2 at any temperature and pressure, and unit fugacity of H_2 and O_2 at 1 bar at any temperature, and assuming pure hematite and magnetite, the value of f_{H2} imposed by the equilibrium in the outer capsule is

$$f_{H2} = K_{hm}^{-1} \tag{3.12}$$

In the inner capsule, homogeneous equilibrium among the H-O components of the fluid phase is described by

$$H_2O = H_2 + 1/2O_2 \quad (3.13)$$

for which the equilibrium constant Kw is

$$K_w = \frac{f_{O_2}^{1/2} f_{H_2}}{a_{H_2O}} \quad (3.14)$$

Combining Eq. (3.12) and (3.14) leads to:

$$f_{O_2} = (K_w K_{hm} a_{H_2O})^2 \quad (3.15)$$

Equation (3.15) shows how fixed hydrogen fugacity in the outer capsule relates to the oxygen fugacity in the inner capsule. Provided that this value is greater than that of CO_2-graphite equilibrium Eq. (3.8),

$$f_{O_2} = K_{cco} K_w^2 a_{CO_2} \quad (3.16)$$

then effectively all carbon will be present as CO_2 in the inner capsule. Figure 3.1 shows that hematite + magnetite equilibrium always keeps f_{O2} many orders of magnitude higher than the value at which CO_2 reduces to graphite, consistent with the absence of graphite in any run products (see below).

3.2.2. Experimental Apparatus and Assembly

All experiments were conducted in an internally heated piston cylinder apparatus with 2.54 cm diameter piston, NaCl pressure medium, and a graphite heater sleeve. Temperature was controlled using a Pt-Pt90Rh10 thermocouple with an estimated accuracy of ±3 °C (Bohlen 1984; Manning and Boettcher 1994), and pressure was measured with a Heise Bourdon tube gauge. Final experimental pressure is achieved using the piston-out technique, in which assemblies were first cold pressurized to 70% of the final value before temperature was increased. Thermal expansion of the assemblies during the subsequent heating raised the pressure to the target pressure of 10 kbar. Pressure was held within ±150 bars of the desired pressure through the duration of the experiment by bleeding excess pressure when necessary. At final run conditions, the NaCl cells are frictionless and require no pressure correction (Manning and Boettcher 1994). The estimated pressure uncertainty of ±3 kbar.

3.2.3. Starting material and loading of experimental charges

The experiments employed natural high-purity quartz from Brazil (Manning 1994). Small equant chips were rounded with a diamond file and then rolled between sandpaper until rounded and smooth. The quartz crystals were then sonicated in water to remove any adhering fragments and dried in an oven at 100 °C. The fluid components included ultra-pure 18-MΩ-cm water and 99.998% oxalic acid (Fisher Chemical).

As noted above, the capsule assembly consists of an outer gold capsule containing hematite + H_2O buffer, and an inner platinum capsule containing the fluid phase and quartz. All

capsules were cleaned with acetone prior to use, welded shut on one side with an PUK-15 welder, and annealed at ~ 1000 °C in a Bunsen burner flame.

All weightings were done using a Mettler Toledo UMX2 analytical balance with an uncertainty of ± 0.1 μg. All weighing's were made in triplicate and were within ~1.5 μg of the mean weight. The inner Pt capsule measured 10 mm in length and 2.5-mm in diameter. The sealed Pt capsule was then loaded into the Au outer capsule which measured 18 mm in length and 4.5 mm in diameter. After first weighing the inner Pt capsule, crystalline oxalic acid then a quartz sphere was loaded and the capsule reweighed. H_2O was then added with a syringe and allowed to evaporate until the desired water weight was obtained. The capsule was then pinched shut, weighed, and welded. Typical weight loss due to Pt evaporation on welding was approximately 0.01 mg, which has a negligible effect on the solubility measurements. The sealed Pt capsules were then loaded into Au capsule segments fallowed by hematite, and 5 mg of H_2O, and welded shut. The addition of H_2O promotes buffer effectiveness at experimental conditions.

3.2.4. Capsule opening and run-product analysis

At the conclusion of the piston/cylinder runs, power to the apparatus was cut, resulting in quench times of 87 seconds from run temperature to ~110°C. Pressures typically declined by 25 % (or to ~7.5 kb) during the quench. After extracting the inner Pt capsule from the retrieved outer Au buffer capsule, retention of volatiles was verified by (1) visually checking that Pt capsules were inflated due to elevated CO_2 gas pressure associated with H_2O-CO_2 unmixing on quenching, and (2) cleaning and weighing to check for weight loss that would signal capsule rupture. Successful f_{O2} buffering requires that both hematite and magnetite are present at the end of an experiment. The buffer material was always black and magnetic, indicating magnetite

presence. To verify the presence of hematite, the buffer was ground on a porcelain plate to check for the diagnostic red streak.

After the experiment the inner capsule was washed in deionized water and weight to check for volatile loss during the experiment. Capsules were carefully opened with a razor blade and the quartz crystal was retrieved and sonicated in deionized water to remove any loosely bound material. The quartz crystal was then placed in 110 °C oven to dry for approximately ten minutes. Silica solubilities were calculated from the change between initial and final quartz weight. Samples were then mounted onto carbon tape for SEM analysis.

3.3 Results

Results are presented in Table 3.1 Textures of partly dissolved crystal were examined optically and by SEM. Quartz crystals in pure-H_2O runs showed euhedral growth faces Figure 3.2a. However, the addition of CO_2 resulted in subhedral morphology Figure 3.2b. In all reported runs, hematite and magnetite were present in the f_{O2} buffer assemblage, and no graphite was present in run products.

Reaction equilibrium is assumed based on: (1) only ~ 2 hours are needed for equilibrium between quartz and H_2O at 700 °C and 10 kbar (Newton and Manning 2000); (2) Newton and Manning (2009) report run times as low as 5 hours at 10 kbar, 800 °C and $X_{CO2} = 0.5$; and (3) at 500 °C and 10 kbar a 4-hour experiment yielded a solubility result within 5% of Manning's (1994) results for run times of 25.25 and 261.5 hours. All reaction run times in this study exceeded four hours.

Figure 3.3 shows mole fraction of SiO_2 (X_{SiO2}) vs mole fraction of H_2O (X_{H2O}) for all experiments of the present study, where the X_{SiO2} was determined by:

$$X_{SiO2} = \frac{n_{SiO2}}{n_{H2O}+n_{CO2}+n_{SiO2}} \quad (3.17)$$

and where n_i is the number of moles of the subscripted component. At constant P and T, X_{SiO2} decreases exponentially with increasing mole fraction of CO_2 (X_{CO2}), as illustrated by the linear trends in the data at each temperature. As X_{CO2} approaches 1.0, the concentration of silica at all temperatures converges, because silica is effectively insoluble in pure CO_2. For consistency, where no pure water runs were conducted, the predicted solubilities of Dolejs and Manning (2010) were plotted.

3.4. Discussion

The new quartz solubility data at 800 °C, 10 kbar, agree closely with previous results of Newton and Manning (2009) in H_2O-CO_2 fluids (Fig 3.3A). The results confirm Newton and Manning's observation of an exponential decline in quartz solubility with increasing X_{CO2} at this P and T. My new data indicate similar exponential decline in X_{SiO2} with X_{CO2} at all T from 500-800 °C (Fig. 3.3), allowing a more robust understanding of silica-H_2O interactions to be obtained.

3.4.1 Calculating activity of the silica monomer

Equation (3.5) demonstrates that the activity of a silica complex is required to determine its hydration number. This requires that an experimental solubility measurement must be converted from its concentration into an activity. At the conditions of the present study and pH near neutral, Zhang and Frantz (2000), Zotov and Keppler (2000, 2002); and Newton and

Manning (2002, 2003), have shown that aqueous silica in otherwise pure H_2O exists as a mixture of monomers, $Si(OH)_4 \bullet (n\text{-}2)H_2O$, and dimers, $Si_2O_4 \bullet (2n\text{-}1)H_2O$. Higher order silica oligomers are negligible (<<1%). The presence of the dimer in addition to the monomer demonstrates that the assumptions of Walther and Orville (1983) were invalid.

Newton and Manning (2002, 2003) derived a simple mixing model for monomers and dimers, which adequately describes H_2O-SiO_2 fluids to >20 kbar and approximately 800 °C. Equilibrium between hydrated and solvated monomer and dimer molecules is

$$2Si(OH)_4 \bullet (n\text{-}2)H_2O = Si_2O(OH)_6 \bullet 2nH_2O + H_2O \quad (3.18)$$

Monomer dimer

Notably, Eq. (3.18) shows that the formation of the dimer from two monomers is a dehydration reaction, as is generally the case for all silica polymerization reactions. Thus, silica speciation depends on H_2O activity. The equilibrium constant for Eq. (3.18) is:

$$K_{md} = \frac{X_d a_{H2O}}{X_m^2} \quad (3.19)$$

where subscripts m, d, and md denote, respectively, monomer, dimer, and monomer-dimer equilibrium. Following Newton and Manning (2009), the standard state for aqueous SiO_2 is taken to be unit activity of the pure hypothetical solution of monomers, and the activities of neutral silica monomers and dimers are equal to their mole fractions. Hence,

$$a_{SiO_2} = \gamma_{SiO2} X_{SiO2} = X_m = a_m \quad (3.20)$$

where γ_{SiO2} is the activity coefficient of aqueous SiO_2. Thus, using the above definitions, the activity of aqueous SiO_2 corresponds to the mole fraction of the monomer. Combination of Eqs. (3.19) and (3.20) gives:

$$a_{SiO_2} = \frac{(1+8X_{SiO_2}K_{md}/a_{H_2O})^{1/2} - 1}{4K_{md}/a_{H_2O}} \quad (3.21)$$

Equation (3.21) shows that the monomer concentration (a_{SiO2}) can be derived from an experimental measurement of total silica in solution (X_{SiO2}), as in the present study, knowing a_{H2O} and K_{md}. In this work, I used the Aranovich and Newton (1999) model for H_2O-CO_2 mixing to derive a_{H2O}. This model yields the greatest consistency with experimental studies of mixed fluid equilibria at the conditions of my experiments.

There are two alternate models for the variation of K_{md} with P and T. Newton and Manning (2009) used experimental data on silica buffering systems from Newton and Manning (2002, 2003) to obtain an empirical model for the variation in K_{md}:

$$\log K_{md} = 1.480 + 0.0012T + (0.000119T - 0.165)P \quad (3.22)$$

where T is in Kelvin and P is in kbar (Newton and Manning, 2016). This equation agreed well with previous experimental results of Zotov and Keppler (2002). In contrast, K_{md} values derived by the DEW model of Sverjensky et al. (2014) differ significantly. K_{md} values were calibrated based on speciation derived from Raman spectroscopy (Mysen, 2010). Fig (3.4) compares K_{md} values from Newton and Manning (2009) and DEW. The differences in K_{md} values results in

distinctive a_{SiO2} between the two models and a different ratio of monomer and dimer concentration. The consequences of the different K_{md} formulations will be considered below.

3.4.2 Calculating the hydration number of the silica monomer

At a given P and T, the silica monomer hydration number can be calculated by rearranging Eq. (3.3) to give

$$n = \log \frac{a_{SiO2}}{K_{qm} a_{H2O}} \tag{3.23}$$

Because K_{qm} varies with P and T, comparison of results at different conditions is simplified by recognizing that in pure H_2O, a_{H2O} can be taken to be unity, and K_{qm} is thus equal to the monomer concentration. Defining the monomer concentration in pure H_2O as a'_{SiO2}, Eq. (3.23) can be rewritten as:

$$n = \log \frac{a_{SiO2}}{a'_{SiO2}} - \log a_{H2O} \tag{3.24}$$

(Newton and Manning, 2009). The value of n and any variation with fluid composition can thus be compared at different P and T using a series of plots portraying the variation of $\log a_{SiO2}/a'_{SiO2}$ with $\log a_{H2O}$.

Figure 1.5 shows results of the present solubility measurements in H_2O-CO_2 solutions using K_{md} values determined from Newton and Manning (2009) (Eq. 3.22). I did not measure quartz solubility in pure H_2O in this study. Values of a'_{SiO2} were determined from the model of Dolejs and Manning (2010), which accurately reproduces experimental results over a wide range

of P and T. The data at each T display linear variation with a_{H2O}, as indicated by high R^2 at each T. As noted above, my new data agree with Newton and Manning's (2009) results at 800 °C and 10 kbar, yielding a similar value for n of 4.1. However, Fig. 3.5 shows that n systematically increases with decreasing T, from 4.1 at 800 °C to 7.4 at 500 °C.

Fig. 3.6 shows results calculated using K_{md} values from DEW. For consistency, a_{SiO2} is normalized to a'_{SiO2} using X_{SiO2} in pure water calculated using the thermodynamic data for silica species in the DEW model (Sverjensky et al., 2014). Differences from Dolejs and Manning (2010) are minor. The results are similar to those shown in Fig. (3.5): the data describe linear arrays R^2, and n values increase with decreasing temperature from 4.6 at 800 °C to 6.7 at 500 °C.

Figure 3.7 shows n values calculated from the experimental data using the two alternate K_{md} formulations (Fig. 3.5 and 3.6). It can be seen that the contrasting K_{md} values lead to a maximum of only ~10% difference at the highest and lowest T of 500 and 800 °C, even though at these conditions K_{md} values differ by 135 and 92%, respectively (Figure. 3.4). This indicates that n is relatively insensitive to K_{md}, as previously discussed by Newton and Manning (2009). Accordingly, I use the K_{md} model of Newton and Manning (Eq. 3.23) for all further comparisons to other data sets and model derivations. Use of DEW K_{md} values would result in slightly different equations but would not change any of the conclusions.

The results shown in Figs. 3.5 to 3.7 demonstrate that slopes are linear at all T from 500-800 °C. This implies that n is a constant at 10 kbar and a fixed T for H_2O-CO_2 fluids. However, the slopes vary systematically with T, and the best-fit n values at each T are not integers. This contravenes the interpretations of Newton and Manning (2009) and Walther and Orville (1983), who advocated a constant integer value of 4 for all P and T. Figs 3.5 and 3.6 clearly demonstrate that n = 4 does not adequately reproduce the data at T below 800°C. Assuming that two H_2O

molecules are consumed in making silicic acid monomers ($Si(OH)_4$), this implies that H_2O of solvation systematically decreases with increasing T. Notably, integer values of n are not required thermodynamically, as n can simply be interpreted to reflect a time and spatial average of the number of solvating H_2O molecules per mole of silica. A decrease in n with increasing T is sensible in light of a decreases in H_2O dielectric constant (see below).

3.4.3 Pressure and Temperature dependence of n

Numerous studies have investigated quartz solubility in H_2O-CO_2 solutions from 2 – 10 kbar and 500 – 800 °C, (Novgorodov, 1975; Shettel, 1974, ms; Walther and Orville, 1983; Shmulovich et al., 2001, 2006; Newton and Manning, 2009); however, not all data sets provide adequate information to determine n accurately. Shettel (1974 ms) provided large data sets at 2-5 kbar, 500-900 °C, but the work was never published so I omitted these data from my analysis. In many of the remaining studies, only 2-3 experiments were conducted at a particular P and T. When coupled with large scatter and limited X_{CO2} range, many of these earlier data sets do not provide adequate constraints on n and its variation with P and T. Accordingly, to ensure an accurate determination of slopes (n), I only consider data sets containing four or more data points and solubility determinations at $X_{CO2} > 0.4$. Our preliminary results show all 2 kbar data are inconsistent with the determined trend and further consideration of a_{H2O} and K_{md} values are required.

Using the above criteria, experiments by Novgoradov (1975) and Shmulovich (2001) at pressures between 5 and 9 kbar and 500 to 800 °C allow for a more thorough investigation of P and T effects on n. Their experimental data lack the precision of the current data, but they provide sufficient accuracy to identify trends. Figure 3.8 plots the calculated monomer activity

relative to that in pure H_2O, at 10 kbar, using the Newton and Manning (2009) equation for K_{md}. Linear least-squares fitting yields n = 4.2 at 800 °C, 9 kbar, n = 3.9 at 700 °C, 5 kbar, and n = 3.2 at 700 °C, 3 kbar. In this analysis I used quartz solubilities in pure H_2O as published by Novgoradov (1974) and Shmulovich et al. (2001), which agree well with values predicted by Dolejs and Manning (2010). The evaluation of monomer hydration number from 3 – 10 kbar and 500 – 800 °C confirm that n is best taken as a variable dependent on P and T.

3.4.4 Hydration number in empirical density-based models of quartz solubility

There are a number of published empirical approaches to computing the solubility of quartz in H_2O-CO_2 fluids. These models are designed only to predict total silica in solution and do not account for silica speciation. They use the density of H_2O as a primary independent variable. Here I evaluate the degree to which these "density-based models" agree with my new data and the earlier data sets shown in Fig. 3.8, and I invert the models for the hydration number they would predict at my experimental conditions.

Figure 3.9 compares the X_{SiO2} determined experimentally in the present study to values predicted by the density-based models of Akinfiev and Diamond (2009), Brooks and Steele-MacInnis (2019), and Shi et al (2019), along with the thermodynamic model of Newton and Manning (2009). All models reproduce the bulk solubility measurements at 800 °C, 10 kbar, at high accuracy because the Newton and Manning (2001, 2009) results at this condition were part of the calibrating data set. At lower T, the Shi et al. (2019) model underpredicts bulk solubility at all compositions and T, with the exception of 500 °C. The Akinfiev and Diamond (2009) model tends to yield higher solubilities than those measured at low to moderate X_{CO2}. Only the Brooks and Steele-MacInnis (2019) model accurately predicts the variation in quartz solubility with

increasing CO_2 over the investigated T range. The Newton and Manning (2009) model is also shown for reference. While thermodynamically rigorous, it can be seen that the assumption of constant n = 4 leads to significant overprediction of quartz solubility at T < 800 °C.

The solubilities calculated from the empirical models can be combined with activity models for dissolved silica and H_2O-CO_2 to determine values of n implied by the models. Figure 3.10 plots log a_{SiO2} normalized to the predicted pure water runs of each model vs. log a_{H2O}, using Newton and Manning (2009) and Aranovich and Newton (1999) for silica speciation and H_2O-CO_2 mixing, as above. Fig. 3.10 shows that the three models predict nonlinear variation in a_{SiO2} with a_{H2O}. At 800°C, the nonlinearity is minor, and all models accurately reproduce the data, as expected for a data set used in model calibration. However, at lower T, it is only at 500 °C that the empirical models succeed in predicting measured solubilities. At 550-700 °C there are significant mismatches between model prediction and measure solubility, especially low a_{H2O} less than about 0.7. Notably, the 500°C data set where there is otherwise good agreement does not extend to such low a_{H2O}.

The experimental data sets shown in Fig. 3.8 were used as part of the calibration data for the empirical models of Akinfiev and Diamond (2009), Brooks and Steele-MacInnis (2019), and Shi et al (2019). As expected, the density-based models fit nearly all the data points with reasonable accuracy (Fig. 3.11). Calculated a_{SiO2} and a_{H2O} (Fig. 3.12) again reveal that the implied n varies with fluid composition at all three P and T, along with strongly divergent predictions of a_{SiO2} at low a_{H2O}.

3.5 A new model for silica hydration:

The important control played by the dielectric constant of water (ε_{H2O}) in solute hydration (Eq. 3.6) motivates a new empirical approach to predicting quartz solubility in H_2O-CO_2 fluids. The dielectric constant measures the degree of polarization of water molecules in an electrical field and largely governs water's ability to solvate dissolved species. At ambient conditions water has an extremely high ε_{H2O} of 78.9; however, it strongly varies with P and T. At high pressure the ε_{H2O} decreases as T rises, and it strongly increases with P along isotherms (Sverjensky et al., 2014). Decreasing ε_{H2O} results in weaker solute solvation and stronger electrostatic and chemical interactions between oppositely charged ions, as well as net-neutral solutes with weakly nonuniform surface charge distribution, such as aqueous silica.

Fig 3.13 shows hydration numbers derived from all experiments considered above plotted against the dielectric constant of pure H_2O. The data can be fit with a simple exponential equation:

$$n = 2.0 \exp(0.0545 * \varepsilon_{H2O}) \quad (3.24)$$

($R^2 = 0.994$). Here, the pre-exponential factor 2 forces n to approach 2 at very low values of ε_{H2O}, consistent with the expectation that in the limit of low densities where minimal solvation is likely, two water molecules will still be consumed to form the hydroxyl groups of an unsolvated silica monomer. It is important to note that Eq. (3.24) has the advantage of only a single empirical parameter.

Figure 3.14 compares measured solubilities with those calculated from Eq. (3.24), along with empirical models discussed above. The dielectric constant-based formulation yields an

improved reproduction of the data. This is emphasized in Fig. 3.15, which shows deviations between the experimental data and each model.

Overall, the new model yields improved accuracy for predicting quartz solubility in H_2O-CO_2 fluids. However, I note that Fig. 3.14 shows that Eq. (3.24) slightly underpredicts solubility at the lowest X_{CO2} at all T, 10 kbar. It is possible that this is due to slight inaccuracy in the Aranovich and Newton (1999) model at these conditions. I used the values of n predicted by Eq. (3.24) along with experimental values of quartz solubility to assess the a_{H2O} at each X_{H2O}. Figure 3.16 demonstrates the model's failure to predicted silica solubility at low X_{CO2} can be explained by only a slight inaccuracy in a_{H2O}. The H_2O-CO_2 model of Holland and Powell (1991, "CORK") is shown for reference.

A key question arising from this analysis is: why did Newton and Manning (2009) obtain constant n = 4 at all P and T, in support of Walther and Orville's (1984) early proposal? The answer likely lies in the narrow range of the ε_{H2O} of pure water for the experimental data sets that were available at the time. Figure 3.17 plots the hydration numbers calculated from the individual data sets in Newton and Manning (2009). The shaded envelope plots the predicted hydration states from table (2). Newton and Manning (2009) and Walther and Orville (1983) conclusions can be explained by the narrow ε_{H2O} between 11.5 and 13 (table 3.3) for the experimental data sets analyzed, which corresponds to hydration states $n = 4 \pm 0.3$: Shmulovich et al (2001), 9 kbar, 800 °C, n = 4.17; Novgorodov (1975), 5 and 3 kbar, 700 °C, n = 4.06 and 3.33; and Walther and Orville (1983), 2 kbar, 600 °C, n = 3.80. Fig 3.13 demonstrates why Newton and Manning (2009) reached their conclusion. Values of $\varepsilon_{H2O} > 17.5$ were required in experiments to more fully understand the effects of P and T on silica hydration.\

3.6. Conclusions:

I conclude in this study that at 5-10 kbar and 500-800 °C in CO_2-H_2O solutions,

- The hydration and solvation of aqueous silica are P and T dependent non-integer values of n can simply be interpreted to reflect a time and spatial average of the number of solvating H_2O molecules per mole of silica
- I demonstrated that the empirical density-based based models of; Akinfiev and Diamond (2009), Brooks and Steele-MacInnis (2019) and Shi et al (2019) are only designed to predict total silica in solution and do not account for silica speciation. Inversion of these density based models to obtain activity of silica vs activity of H_2O demonstated that they do not predict a constant n at fixed P and T.
- I derived a simple exponential relationship linking the dielectric constant of pure water to n. When combined with models for SiO_2 and H_2O activity, this new, simple model can predict X_{SiO2} from 3 to at least 10 kbar, and from 500-800 °C.
- The model's slight but systematic underprediction of solubility at low X_{CO2} can be explained by only a slight inaccuracy in a_{H2O}. Failure of the model at 2 kbar likely stems from inaccuracies in the silica speciation model of Newton and Manning (2009) at low P.
- The apparently constant values of n in previous studies arise from a narrow range of pure water dietetic constant investigated.

3. Figures

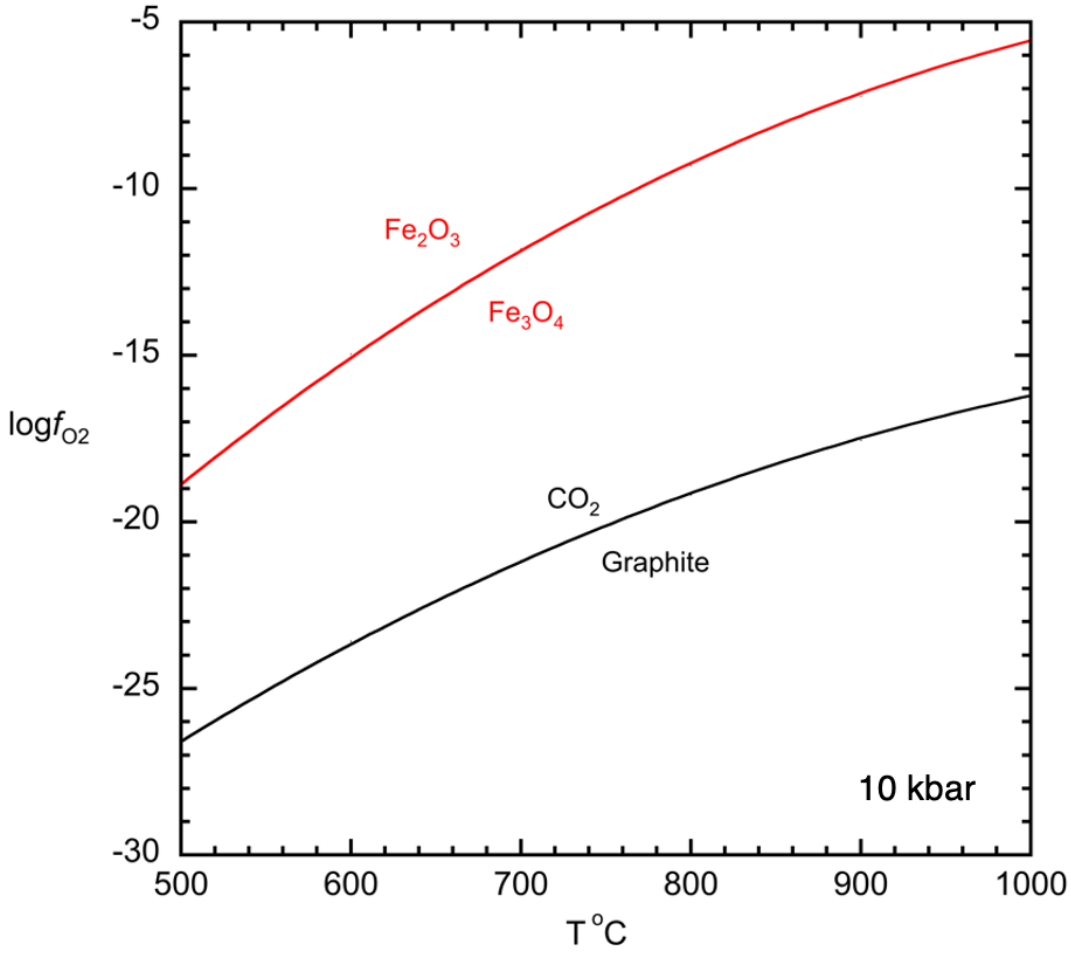

Figure. 3.1. plot of log f_{O2} vs temperature (°C) at 10 kbar, showing the relationship between the oxygen fugacity defined by magnetite and hematite (HM) and graphite and CO_2 (CCO). The diagram was calculated from equations (3.8 – 3.16).

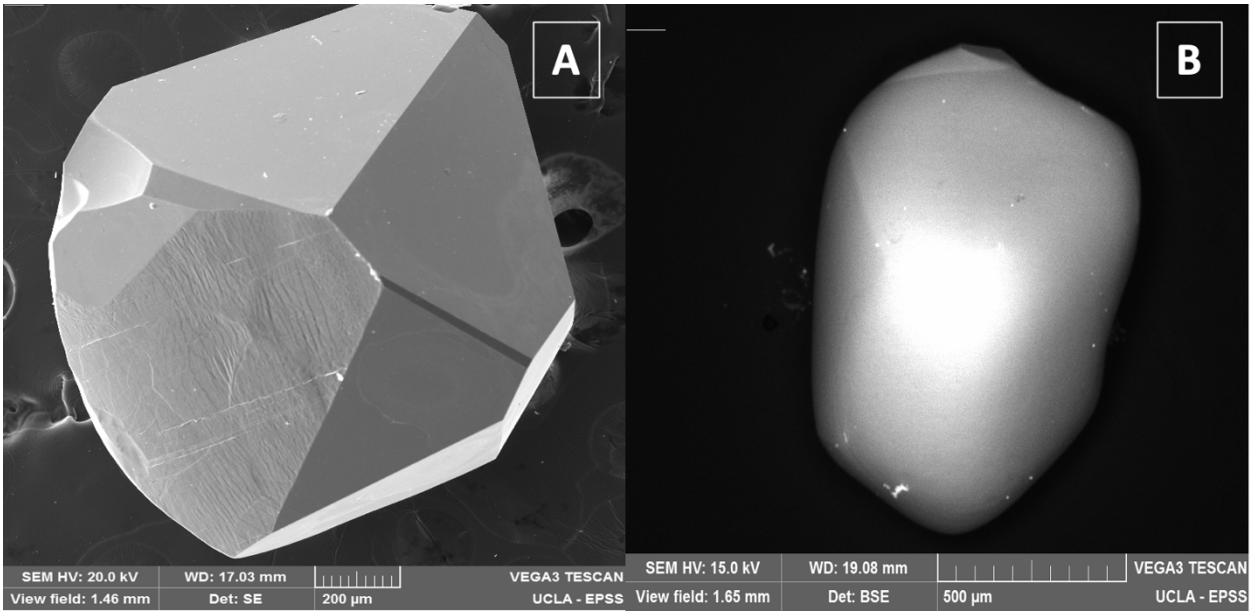

Figure. 3.2. (A) Backscattered electron image of a quartz crystal run in pure water exhibiting a euhedral texture consistent with strong recrystallization and growth of new faces despite net dissolution. (B) Backscattered electron image of a quartz crystal in X_{CO2} exhibiting a rounded texture, suggesting less recrystallization and faceting during dissolution (QT30, Table 3.1).

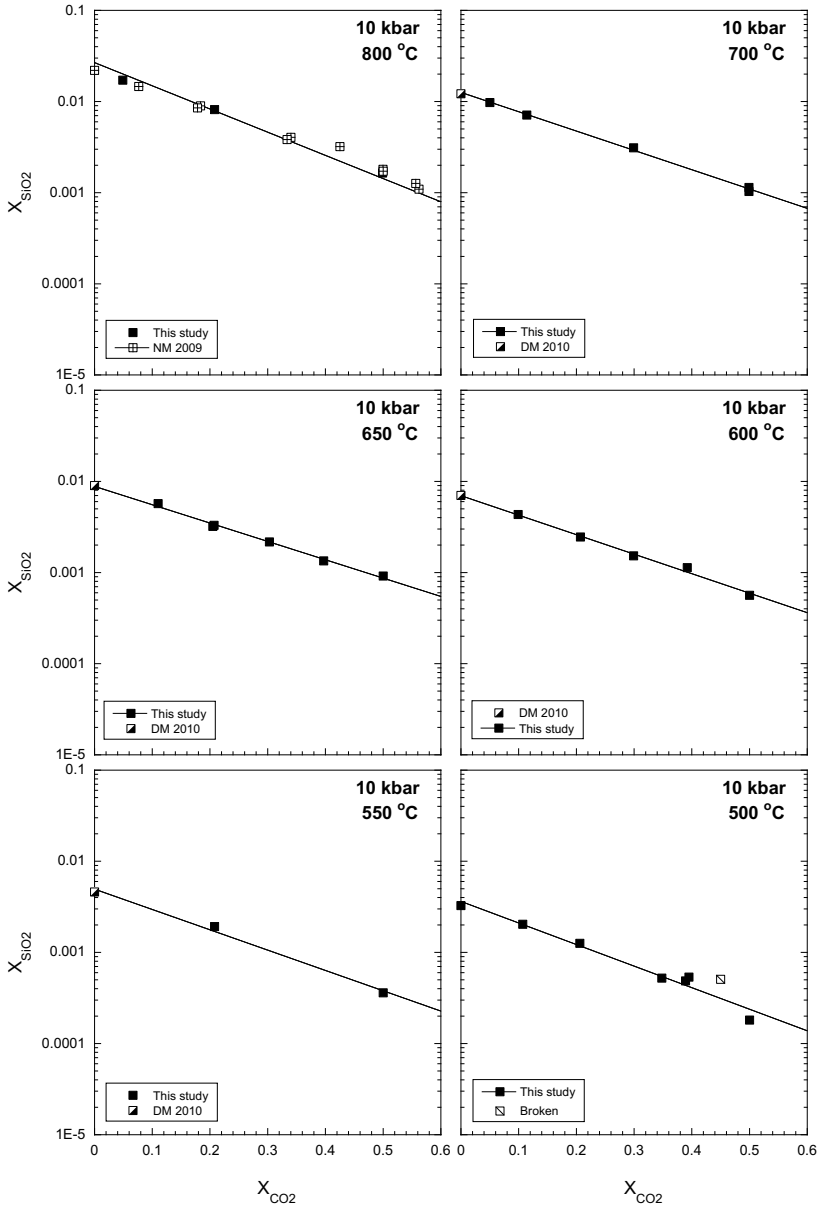

Figure. 3.3. Experimentally determined quartz solubility vs X_{CO2} at 500-800 °C, 10 kbar. Data are presented as mole fraction of total SiO2 in solution. The logarithmic scale suggests an exponential dependence of X_{SiO2} on X_{CO2}. At 800 °C, data from Newton and Manning (2009) are plotted with data from this study to demonstrate consistency between the two data sets. At temperatures where quartz solubility in pure water has not been measured, X_{SiO2} calculated from the equation of Dolejs and Manning (2010) are plotted.

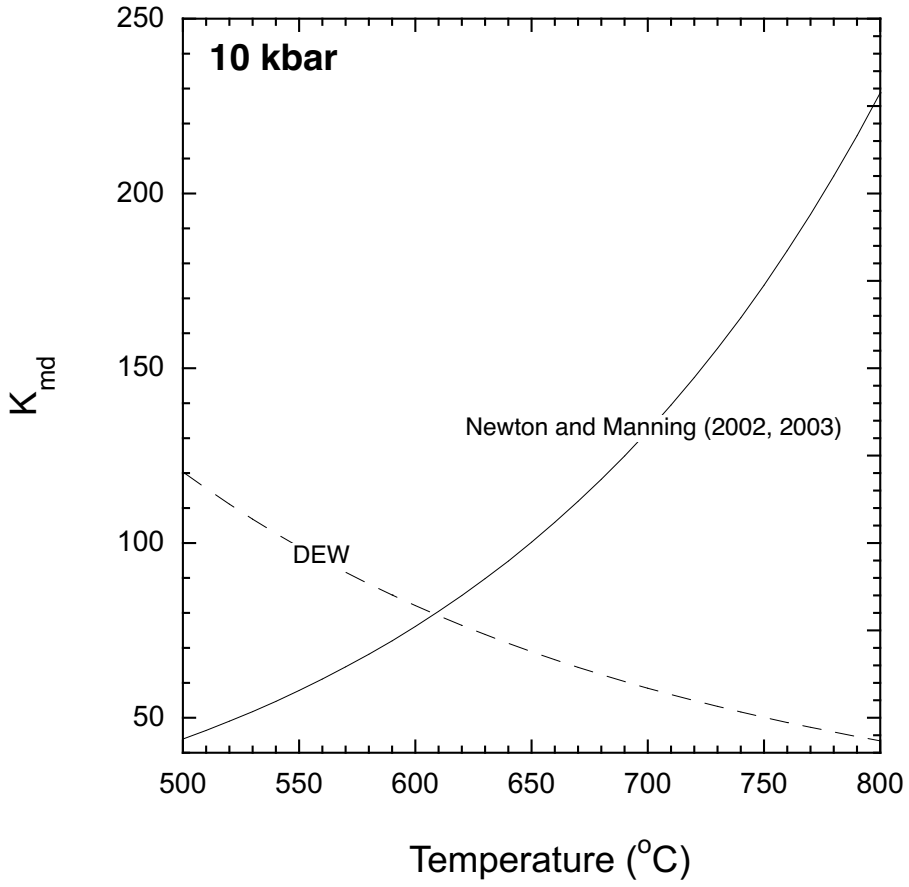

Figure. **3.4**. A comparison between calculated K_{md} values from Newton and Manning (2002, 2003) and the Deep Earth Water model (DEW, version 11.02, Sverjensky et al. 2014), from 500 – 800 °C and 10 kbar.

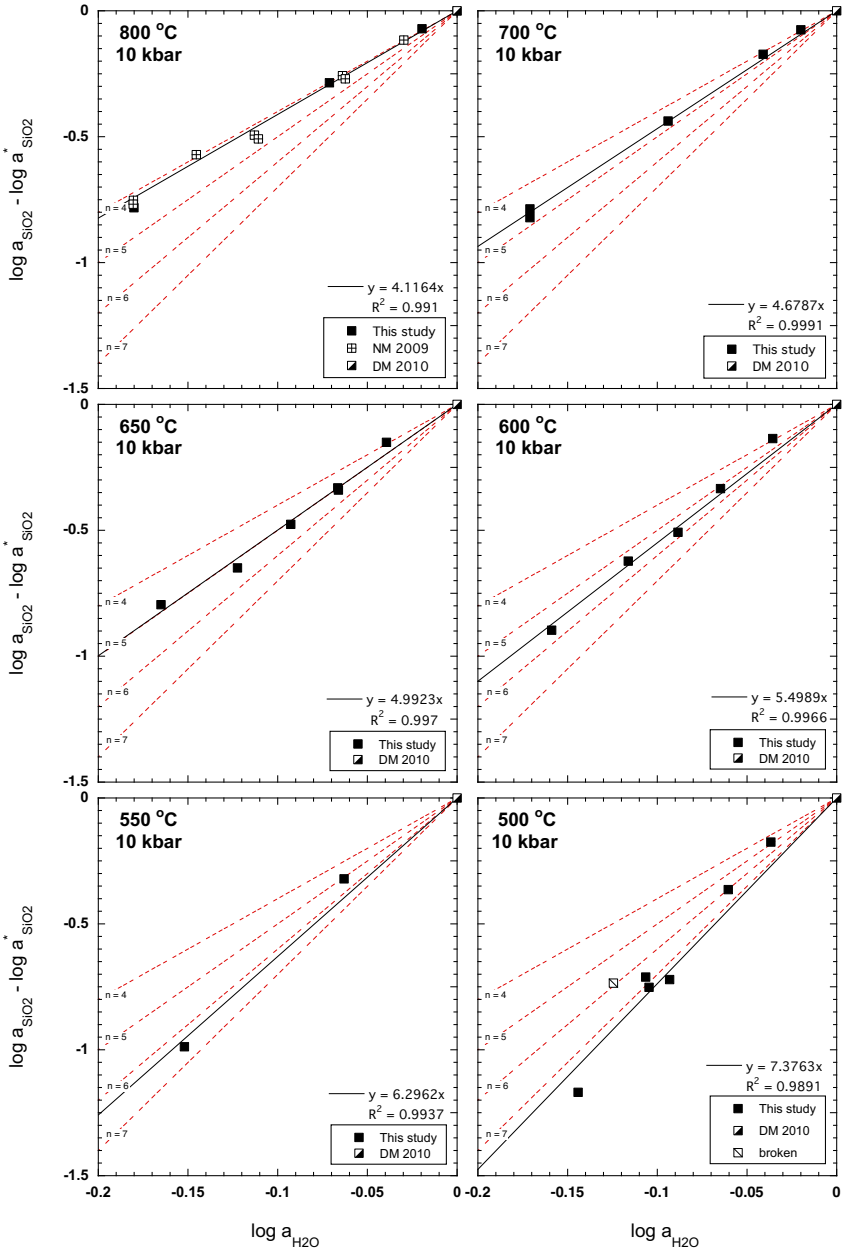

Figure. 3.5. Logarithmic plot of the ratio of a_{SiO2} in mixed fluids to that in pure H_2O (a^*_{SiO2}). Values of a_{SiO2} were calculated from experimental results using Eq. (3.22) and K_{md} values from Newton and Manning (2016), and using X_{SiO2} in pure water runs from Dolejs and Manning (2010). The activity of H_2O was calculated using the model of Aranovich and Newton (1999). Linear fits were forced through an intercept of zero. Red dashed lines of fixed slopes of 4, 5, 6 and 7 are plotted for reference.

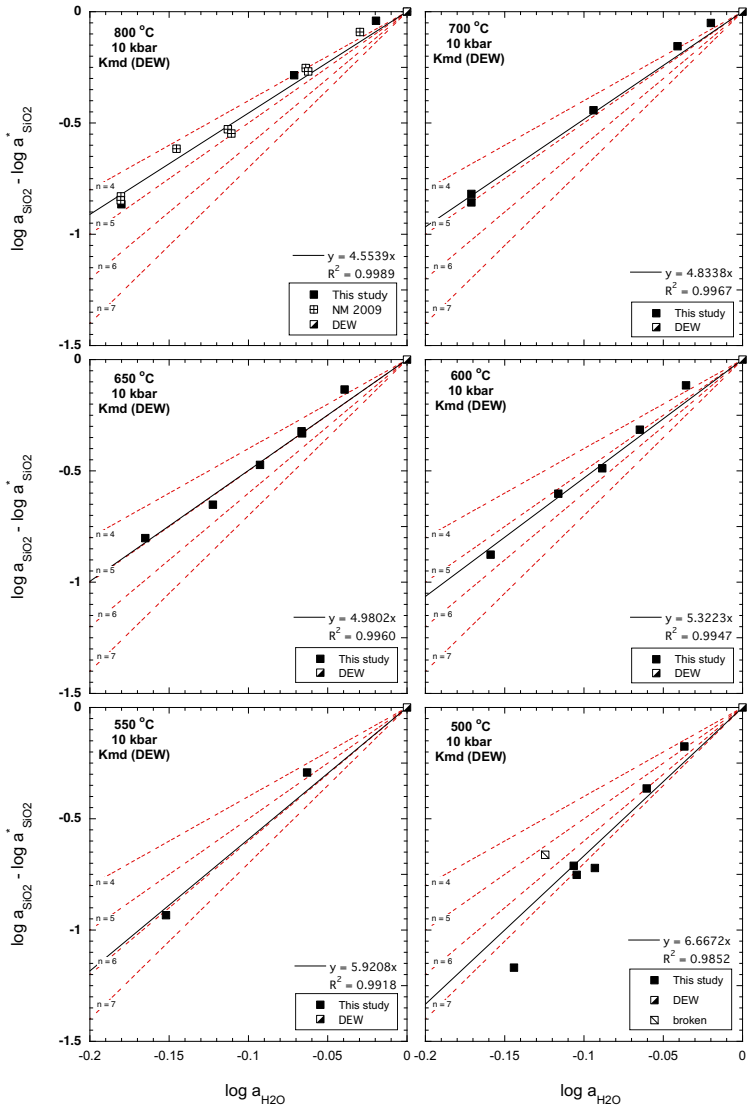

Figure. 3.6. As in Fig. 3.5, except X_{SiO2} and K_{md} were taken from DEW (version 11.02, Sverjensky et al. 2014).

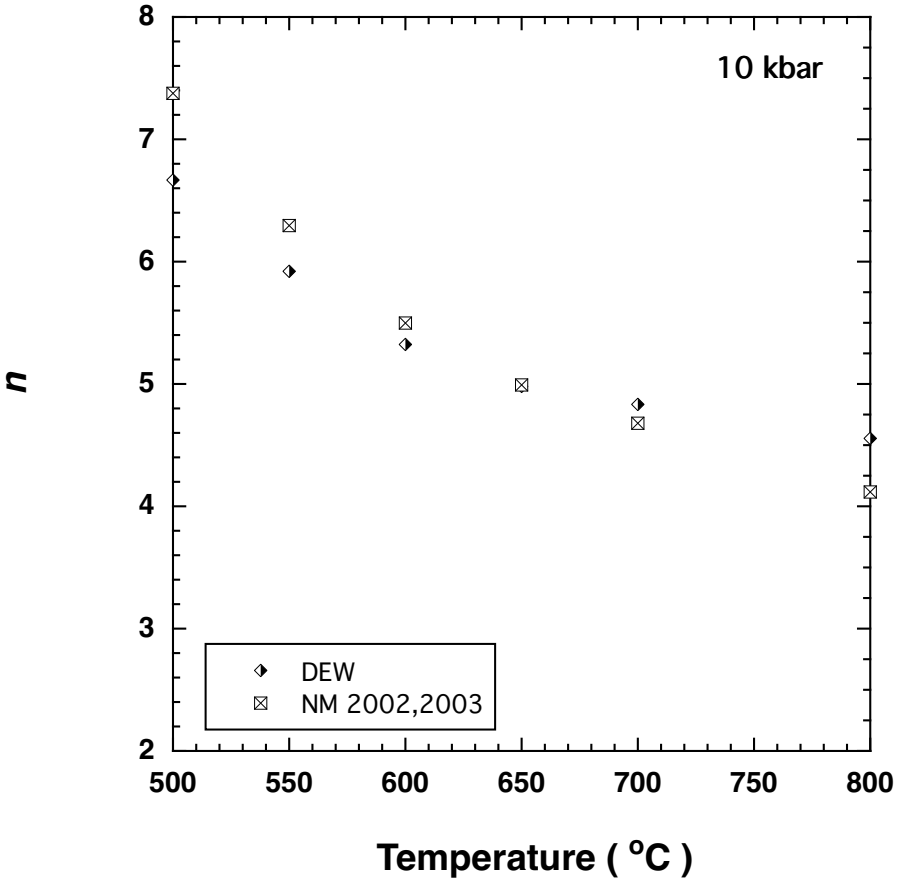

Figure. 3.7. Comparison between hydration state of the aqueous monomer determined in Figures. 3.5. and 3.6 at 10 kbar, 500-800 °C.

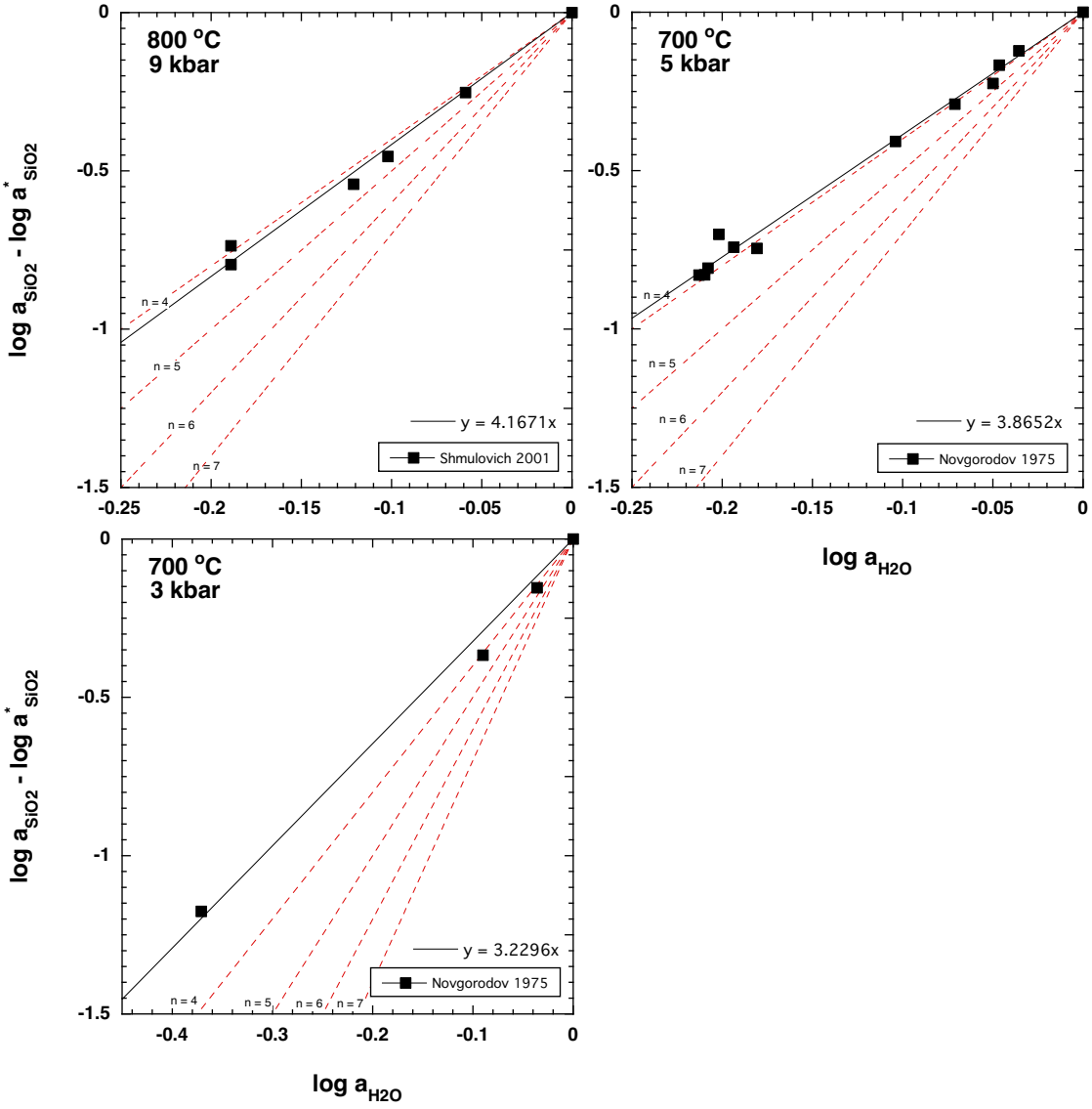

Figure. 3.8. Logarithmic plot of the ratio of a_{SiO2} in mixed fluids to that in pure H_2O (a^*_{SiO2}) vs a_{H2O}. The three panels display the data of Shmulovich (2001) 800 °C, 9 kbar, Novgorodov (1974) 700 °C, 3 kbar and Novgorodov (1974) 700 °C, 5 kbar. Activities of SiO_2 and H_2O calculated by as in Fig. 3.5. Linear fits were forced through an intercept of zero. Red dashed lines of fixed slopes of 4, 5, 6 and 7 are plotted

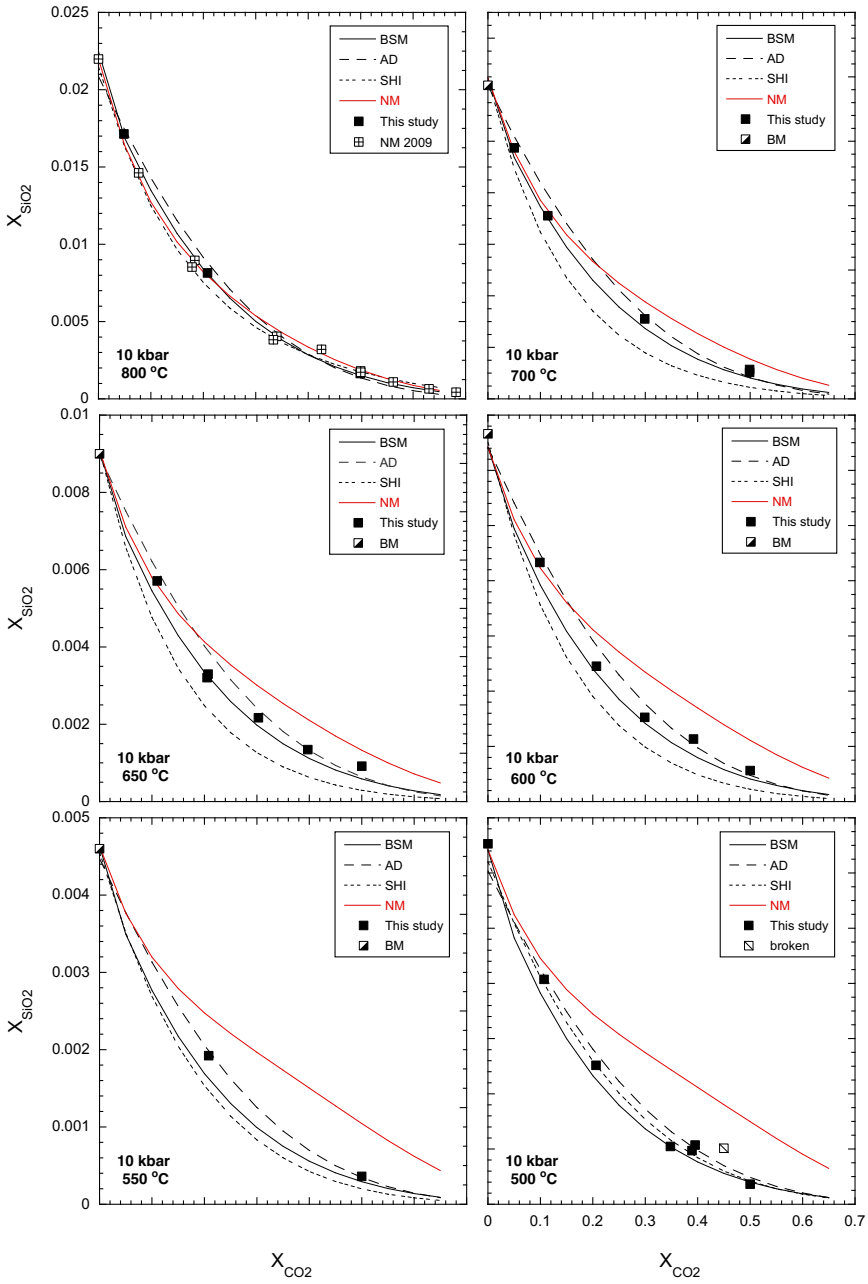

Figure. 3.9. Comparison of quartz solubility measurements from this study to X_{SiO2} calculated by the models of Brooks and Steele-MacInnis (2019), Akinfiev and Diamond (2009), Shi et al., (2019) and Newton and Manning (2002, 2003, 2016) at 10 kbar, 800-500 °C.

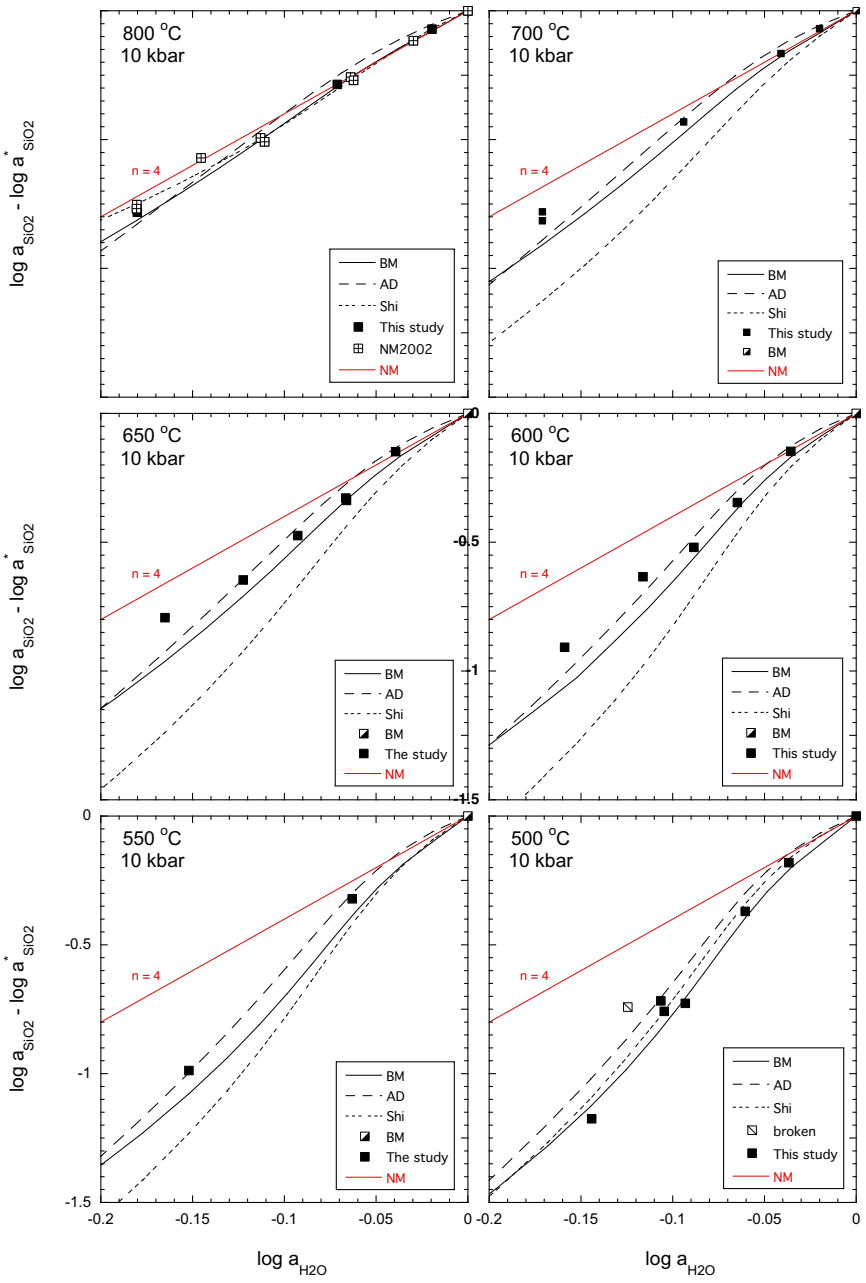

Figure. 3.10. Logarithmic plot of the ratio of a_{SiO2} in mixed fluids to that in pure H_2O (a_{SiO2}) vs. a_{H2O}. This study's high-precision, data at 800, 700, 650, 600, 550 and 500 °C, 10 kbar are compared to the calculated X_{SiO2} of Brooks and Steele-MacInnis (2019), Akinfiev and Diamond (2009), Shi et al., (2019) and Newton and Manning (2002, 2003, 2016). Activities of SiO_2 and H_2O calculated as in Fig. 3.5.

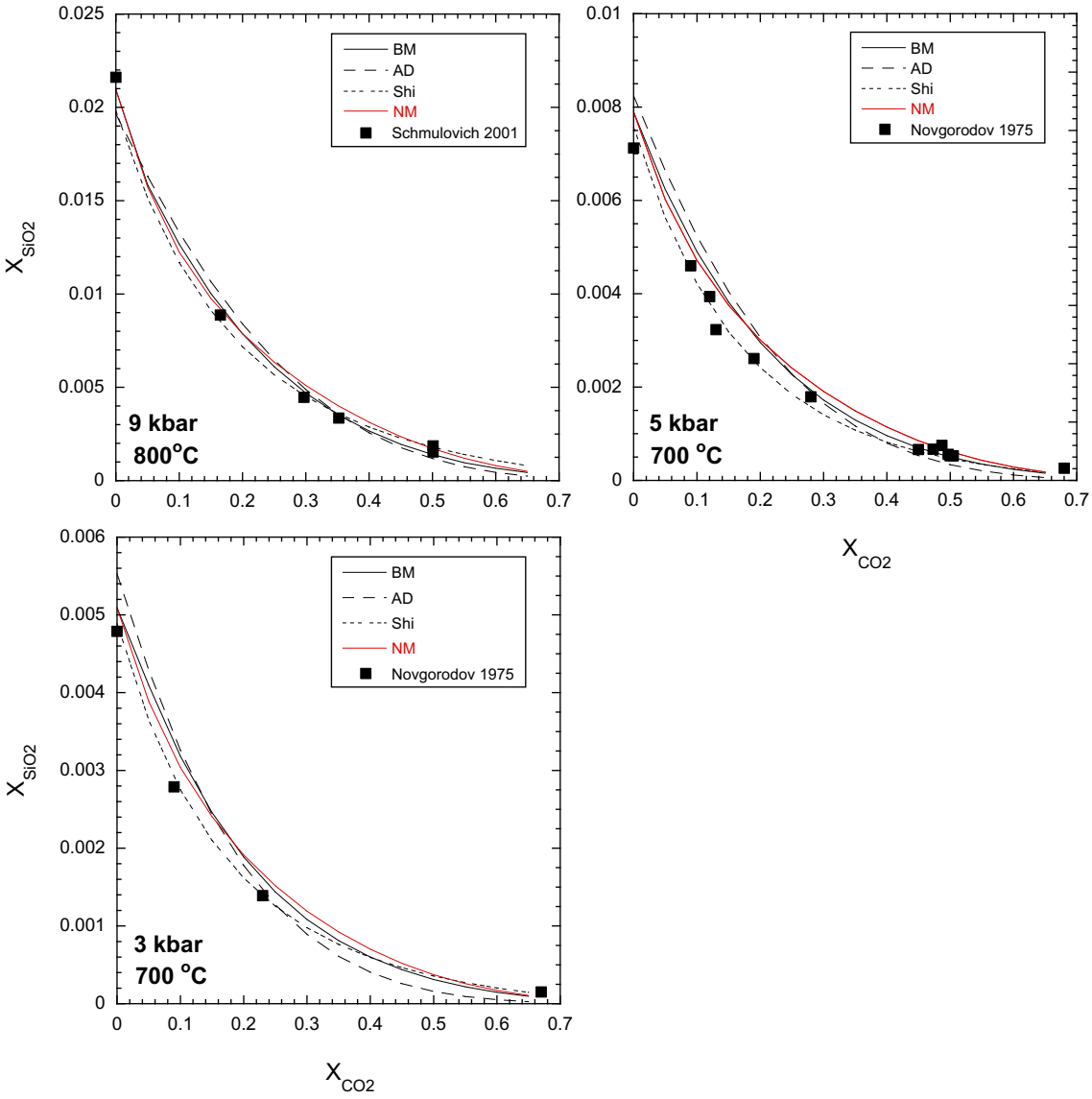

Figure. 3.11. Quartz solubility data of Schmulovich (2001, 9 kbar, 700 °C) and Novgordov (1975, 5 kbar, 700 °C, and 3 kbar, 700 °C) compared to the models of Brooks and Steel-MacInnis (2019), Akinfiev and Diamond (2009), Shi et al., (2019) and Newton and Manning (2016).

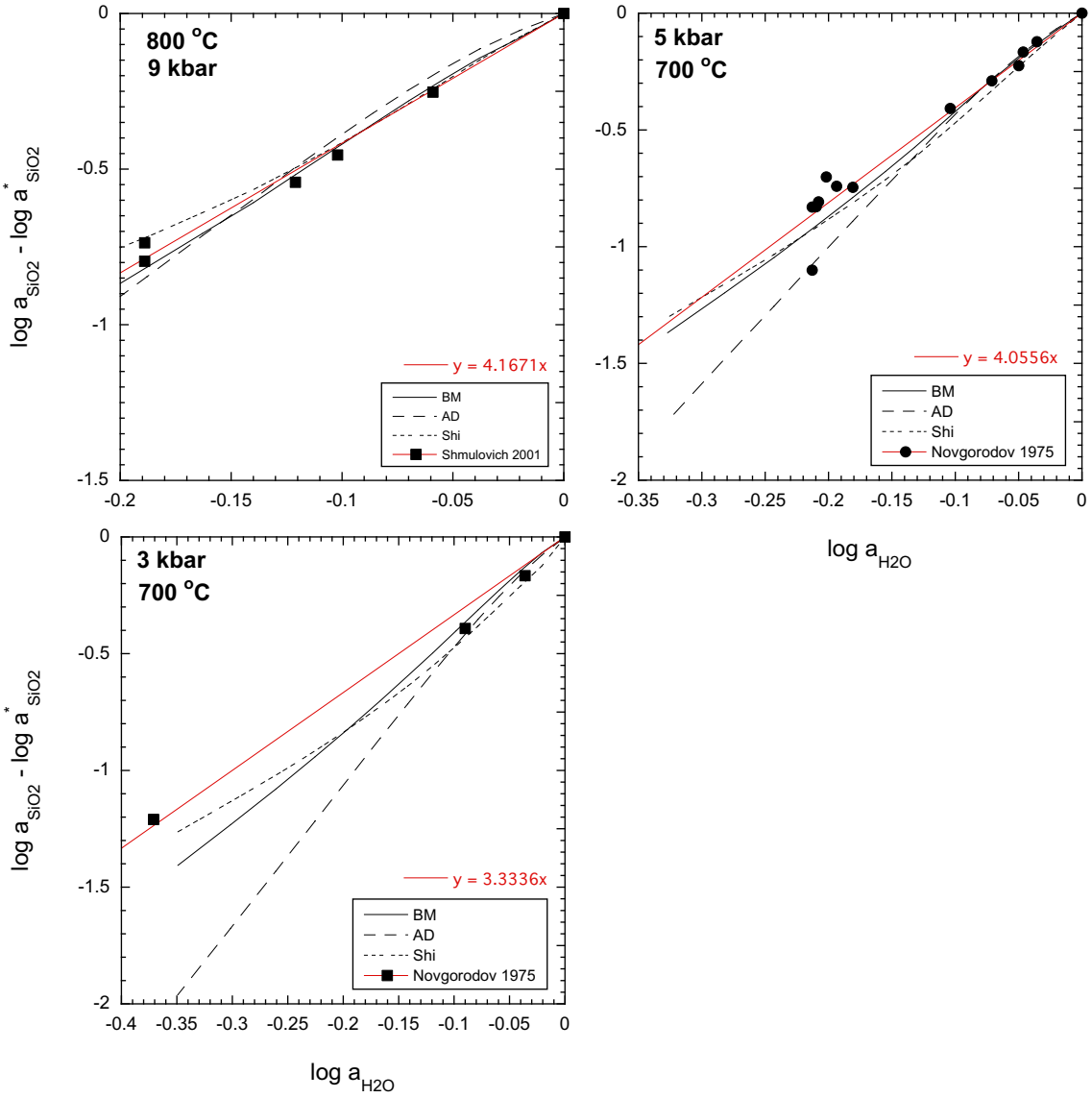

Figure. 3.12. Logarithmic plot of the ratio of a_{SiO2} in mixed fluids to that in pure H_2O (a_{SiO2}) vs. a_{H2O}. Data from Fig. 3.11 are shown, and activities of SiO_2 and H_2O were calculated as in Fig. 3.5.

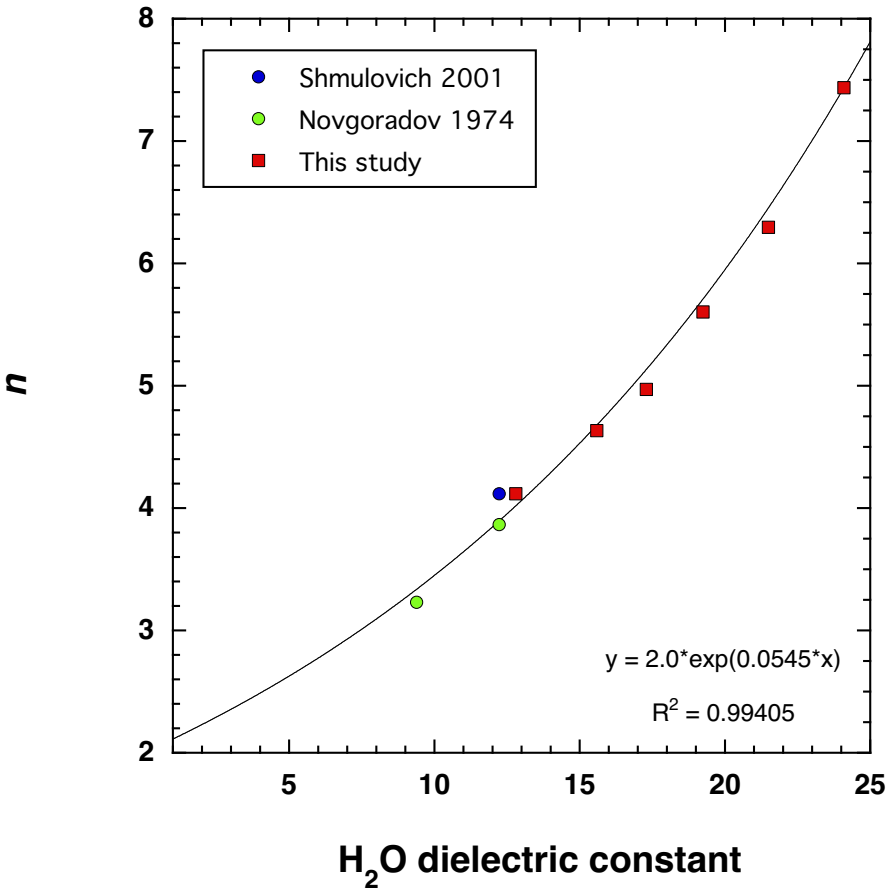

Figure. 3.13. The hydration number of silica vs dielectric constant of pure H_2O. Hydration numbers are from slopes derived in Figs. 3.5 and 3.8. The dielectric constant was calculated from DEW model version (11.0.1, Sverjensky et al. 2014).

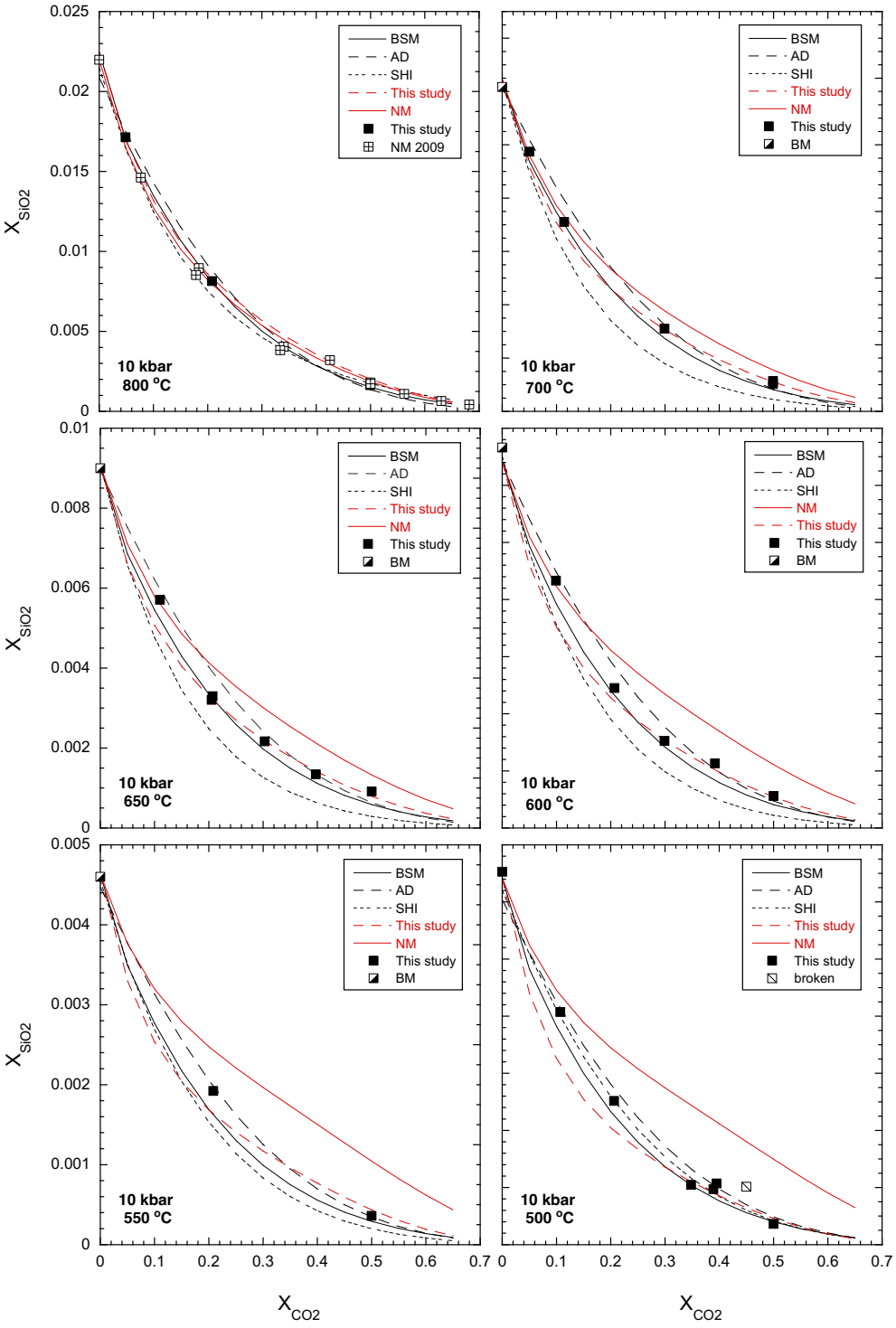
BSM
AD
SHI
This study
NM
This study
NM 2009
BM
broken
10 kbar
800 °C
700 °C
650 °C
600 °C
550 °C
500 °C
X_SiO2
X_CO2

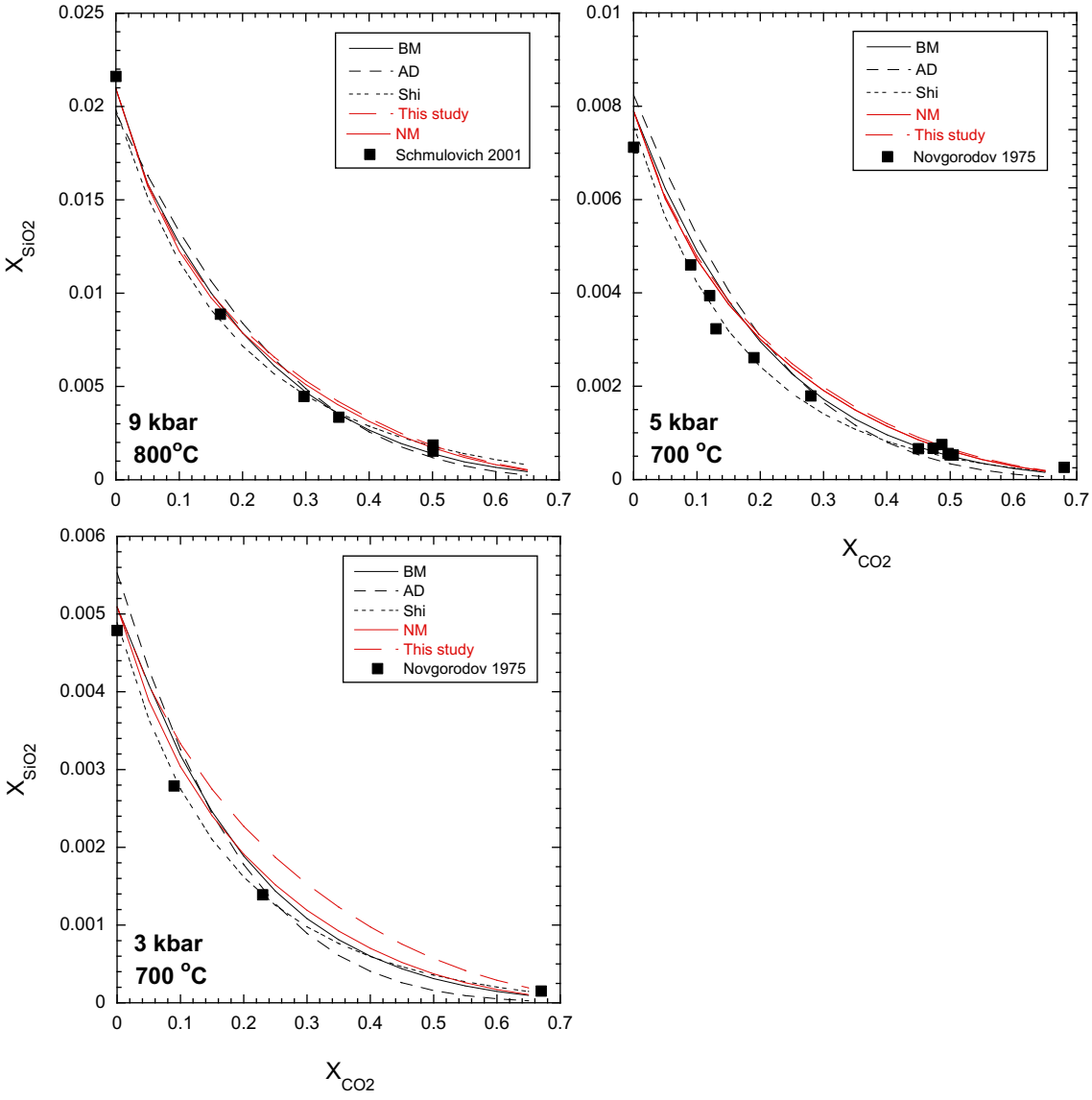

Figure. 3.14. Comparison of quartz solubility data of from this study, Schmulovich (2001) and Novgordov (1975) with models of Brooks and Steel-MacInnis (2019), Akinfiev and Diamond (2009), Shi et al., (2019) and Newton and Manning (2016) and the present investigation.

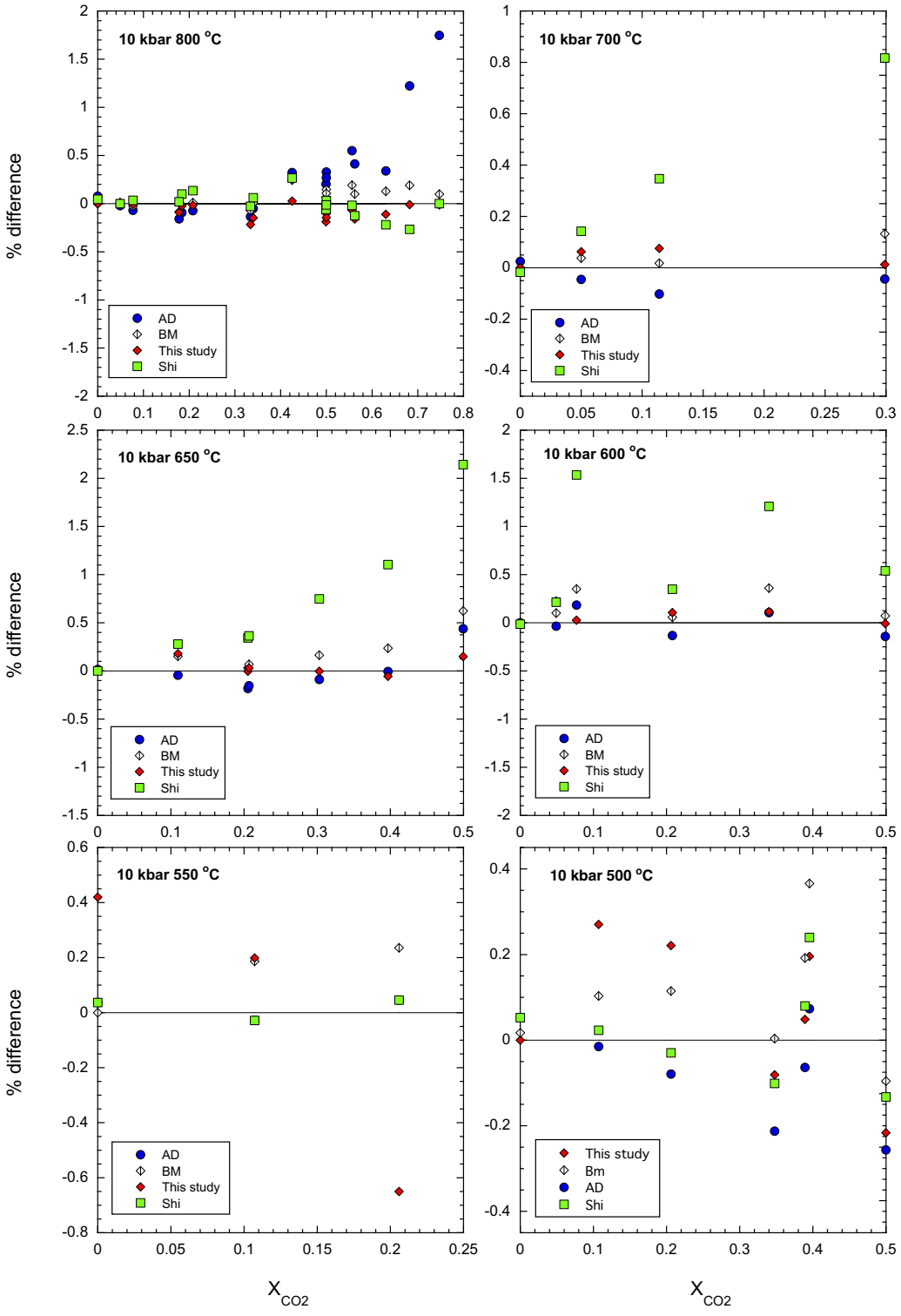
10 kbar 800 °C
10 kbar 700 °C
10 kbar 650 °C
10 kbar 600 °C
10 kbar 550 °C
10 kbar 500 °C
AD
BM
This study
Shi
Bm
% difference
X CO2

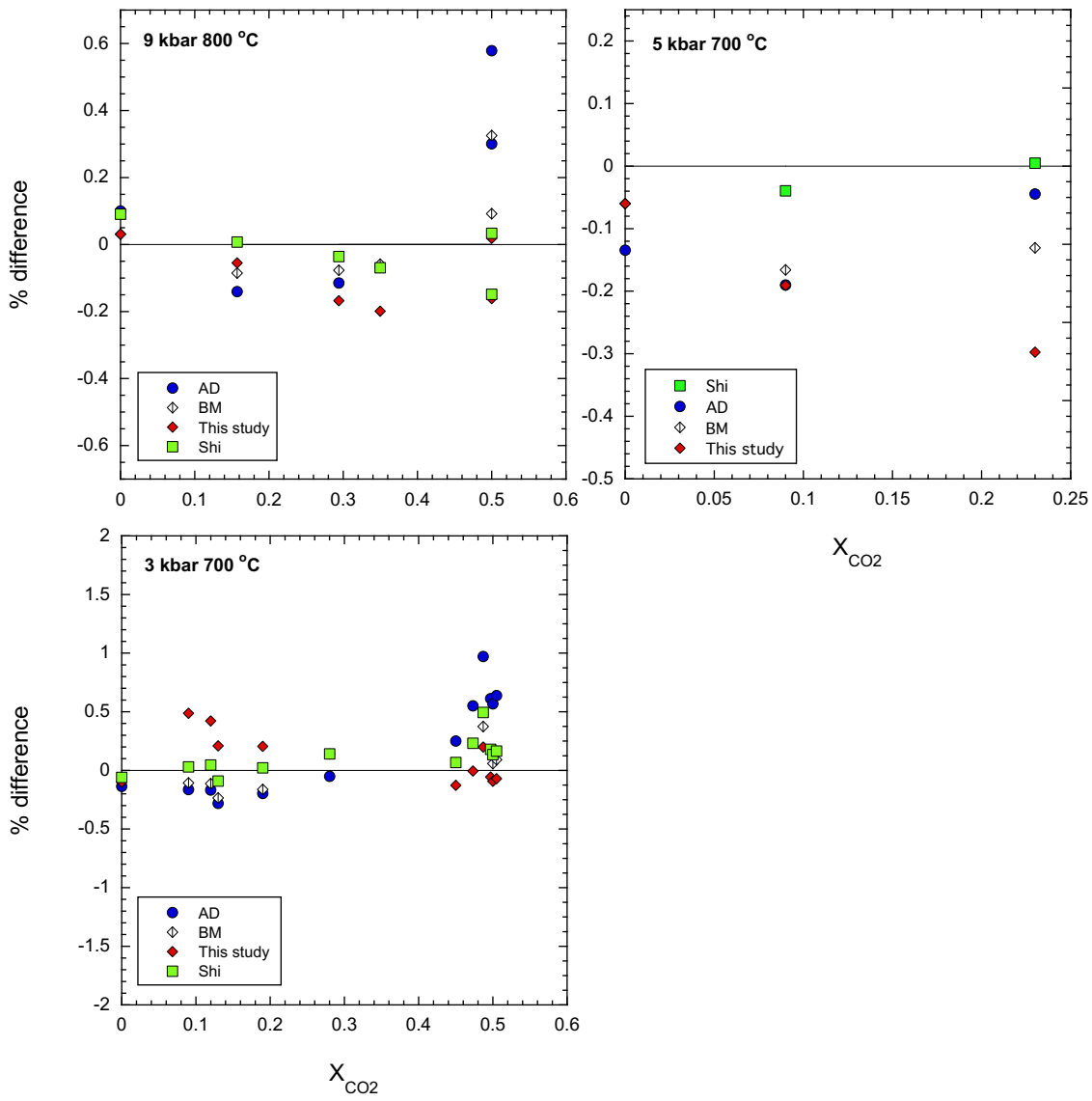

Figure. 3.15. Percentage difference between experimental data and predicted X_{SiO2} from the in Fig. 3.14. At 10 kbar, 800-500 °C, the model developed in the present study shows the smallest deviation from experimental data at T > 600 °C. With decreasing temperature, an increase error occurs at X_{CO2} < 0.8. At 9 kbar, 800 °C this study's model shows the smallest deviation from the data of Schmlovich 2001. At 5 and 3 kbar, 700 °C Shi et al., (2019) shows the smallest deviation while all other models result in slightly larger differences.

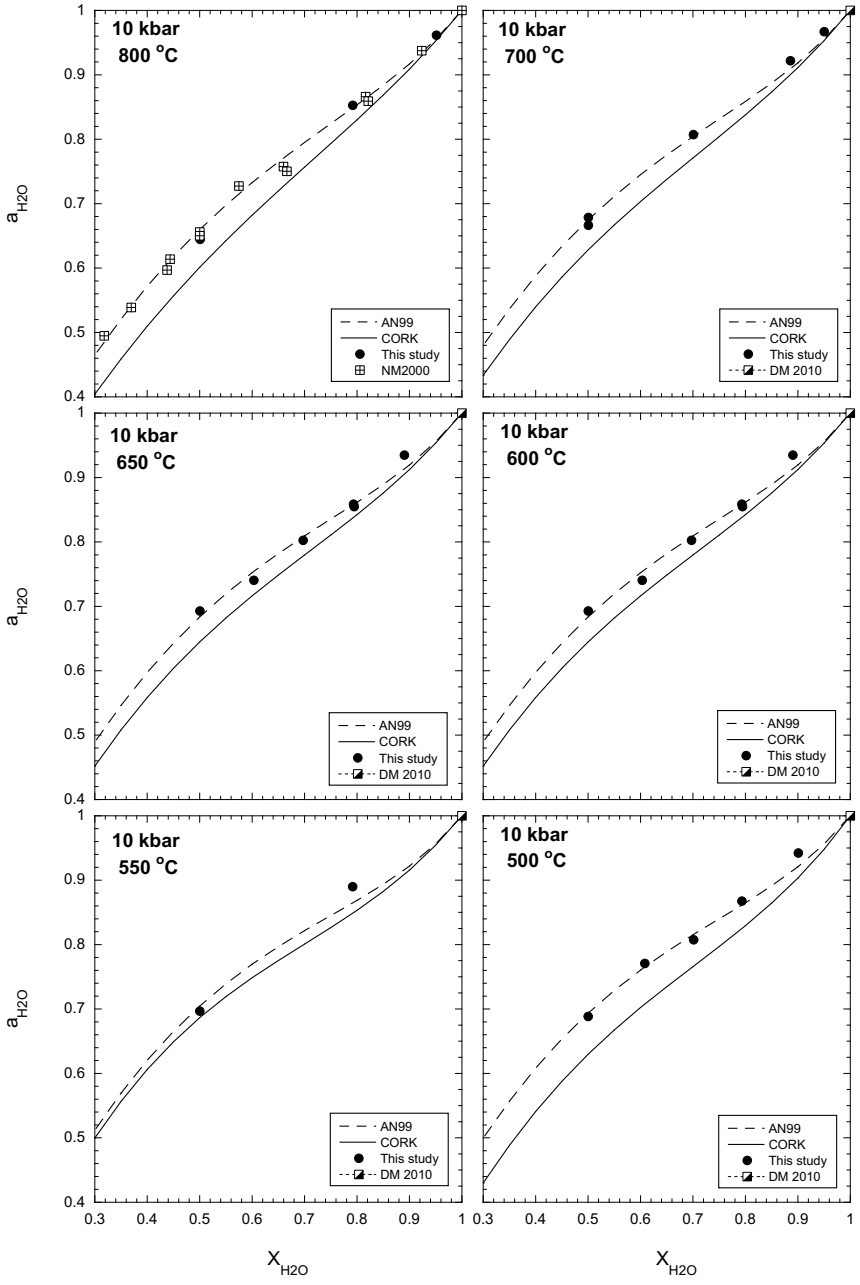

Figure. 3.16. Plot of a_{H2O} versus X_{H2O} calculated by Aranovich and Newton (1999) and CORK at 10 kbar, 500-800 °C compared to the a_{H2O} required for Eq. (3.22) to reproduce X_{SiO2} of the experimental runs in this study. At 800 °C, 10 kbar, the runs of Newton and Manning (2009) are plotted. At all temperatures, the a_{H2O} calculated by Aranovich and Newton (1999) reproduced X_{SiO2} best, whereas a_{H2O} calculated by CORK underpredicted X_{SiO2}. At $X_{CO2} < 0.9$, both models systematically underpredicted the a_{H2O} required to reproduce the experimental data.

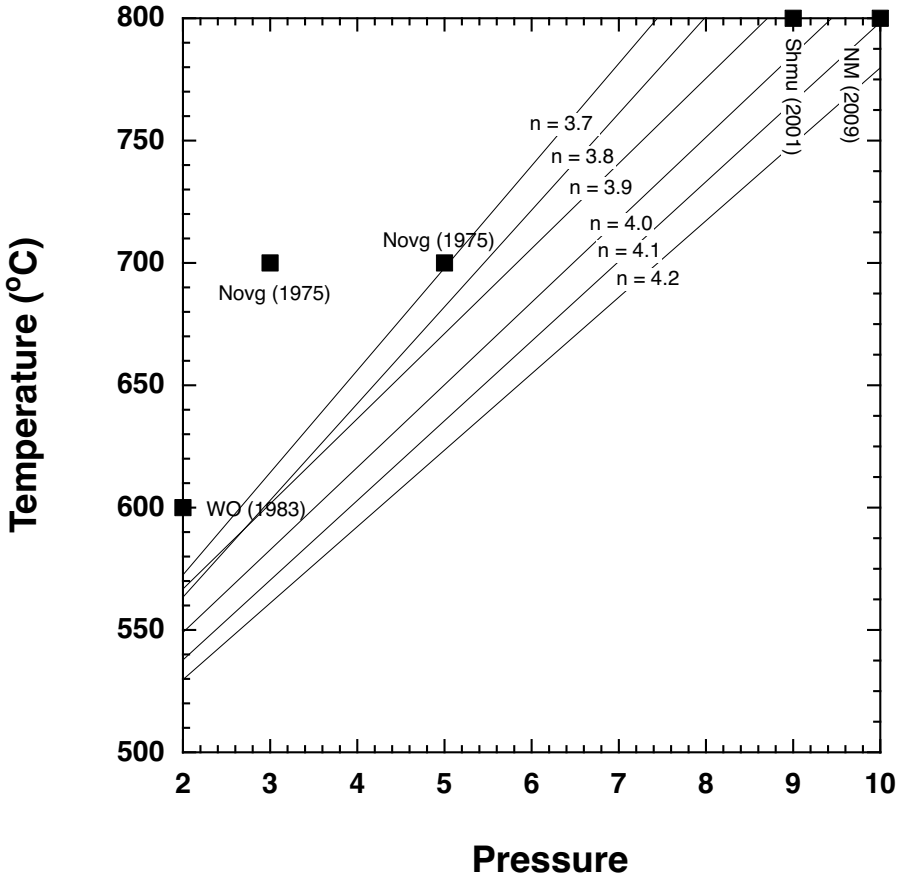

Figure. 3.17. P-T diagram showing hydration number isolines (P in kbar). Previously published interpretations of Walther and Orville (1983) and Newton and Manning (2009) were based on experiments limited to a narrow range of n because they sampled only a small variation in H_2O dielectric constant.

3 Tables

Table. 3.1. Experimental result: Quartz solubility 500 – 800 °C, 10 kbar in H_2O-CO2 solutions

Expt No.	T °C	P Kbar	Duration hrs	OAD mg	H_2O added	H_2O total	Qtz in	Qtz out	X_{H2O}	X_{CO2}	X_{SiO2}	a_{H2O}	$loga_{SIO2} - loga'_{SIO2}$	Notes
DM 2010	500	10								0.000	3.211E-03	1.000	0.000	
QT54	500	10	4	0	29.693	29.693	2.53117	2.20673	0.000	0.000	3.265(05)E-03	1.000	0.000	
QT44	500	10	48	2.127	4.439	5.047	0.66163	0.62313	0.891	0.107	2.037(47)E-03	0.917	-0.038	
MFGO_89	500	10	69	5.373	4.689	6.225	0.61310	0.58180	0.801	0.198	1.259(02)E-03	0.884	-0.054	
QT31	500	10	48	7.293	1.824	3.908	0.48443	0.47397	0.652	0.348	5.231(37)E-04	0.804	-0.095	
QT48	500	10	46	8.040	1.305	3.603	0.98460	0.97503	0.610	0.389	4.860(50)E-04	0.783	-0.106	
QT32	500	10	20	13.085	1.973	5.713	0.47195	0.45503	0.604	0.395	5.364(07)E-04	0.780	-0.108	
QT30	500	10	48	10.620	0.000	3.035	0.48953	0.48587	0.500	0.500	1.807(53)E-04	0.717	-0.145	
QT33	500	10	24	14.183	0.894	4.947	0.45400	0.43877	0.549	0.450	5.071(37)E-04	0.749	-0.126	crystal broke
DM 2010	550	10								0.000	4.600E-03	1.000	0.000	
MGFO_90	550	10	45	5.481	4.377	5.943	2.74450	2.69627	0.790	0.208	1.922(38)E-03	0.865	-0.063	
QT41	550	10	72	11.987	0.000	3.426	1.25237	1.24413	0.500	0.500	3.605(41)E-04	0.705	-0.152	
DM 2010	600	10								0.000	6.418E-03	1.000	0.000	
QT45	600	10	27	2.002	4.594	5.166	2.02457	1.94130	0.896	0.099	4.332(54)E-03	0.921	-0.036	
QT35	600	10	34	6.316	5.100	6.905	1.07840	1.00700	0.791	0.207	2.452(21)E-03	0.862	-0.065	
QT36	600	10	48	8.028	3.080	5.375	1.00517	0.96610	0.700	0.299	1.525(36)E-03	0.816	-0.088	
QT34	600	10	28	13.081	2.051	5.790	0.55833	0.52230	0.607	0.392	1.133(22)E-03	0.765	-0.116	
QT37	600	10	72	10.151	0.000	2.901	0.96390	0.95300	0.500	0.500	5.629(44)E-04	0.694	-0.159	
DM 2010	650	10								0.000	9.079E-03	1.000	0.000	
QT43	650	10	27	2.198	4.443	5.071	2.13400	2.02483	0.885	0.110	5.710(24)E-03	0.913	-0.039	
MGFO_102	650	10	20	5.429	4.427	5.979	2.7568	2.676	0.791	0.205	3.207(06)E-03	0.859	-0.066	
MGFO_103	650	10	23	5.630	4.537	6.146	2.67377	2.5882	0.790	0.207	3.296(31)E-03	0.880	-0.055	
QT39	650	10	21	8.131	3.011	5.335	1.30870	1.25320	0.695	0.303	2.168(33)E-03	0.808	-0.093	
QT42	650	10	48	10.939	1.617	4.743	1.24450	1.20920	0.602	0.397	1.343(32)E-03	0.754	-0.122	
QT38	650	10	24	9.950	0.000	2.844	0.95560	0.93823	0.500	0.500	9.149(40)E-04	0.684	-0.165	
DM 2010	700	10								0.000	1.245E-02	1.000	0.000	
QT49	700	10	6	8.1647	3.1126	5.4461	0.51450	0.43367	0.698	0.299	3.10(18)6E-03	0.805	-0.094	
QT50	700	10	6	2.3778	4.5427	5.2222	1.35137	1.21040	0.879	0.114	7.111(39)E-03	0.909	-0.041	
QT51	700	10	6	1.1578	5.9323	6.2632	0.65983	0.44350	0.941	0.050	9.741(50)E-03	0.956	-0.020	
QT52	700	10	6	14.9905	0.0000	4.2842	0.83033	0.7977	0.500	0.500	1.141(41)E-03	0.675	-0.171	
QT40	700	10	18	10.2382	0.0000	2.9261	0.93753	0.91737	0.500	0.500	1.032(39)E-03	0.675	-0.171	
DM 2010	800	10								0.000	2.248E-02	1.000	0.000	
MGFO_100	800	10	48	1.505	7.840	8.270	2.53477	2.02870	0.934	0.049	1.714(09)E-02	0.956	-0.020	
MGFO_105	800	10	5	5.814	4.600	6.262	2.54833	2.33118	0.784	0.208	8.157(26)E-03	0.849	-0.071	
QT29	800	10	5.5	7.194	0.000	2.056	0.51210	0.48953	0.499	0.499	1.643(89)E-03	0.661	-0.180	

Explanation: Weights of Oxalic acid dihydrate, and H_2O are initial values prior to experiment; H_2O_{tot} is sum of H_2O added and H_2O derived from breakdown of oxalic acid dihydrate. Abbreviations: OAD, oxalic acid dihydrate. All runs were f_{O2} – buffered at hematite-magnetite equilibrium.

Table. 3.2. Hydration number from Eq. (3.24) at discrete pressure (kbar) and temperature (°C)

	800	780	760	740	720	700	680	660	640	620	600	580	560	540	520	500
2	2.6	2.6	2.7	2.7	2.8	2.8	2.9	3.0	3.1	3.2	3.3	3.5	3.6	3.8	4.0	4.2
2.5	2.7	2.8	2.8	2.9	3.0	3.0	3.1	3.2	3.3	3.5	3.6	3.7	3.9	4.1	4.3	4.5
3	2.9	2.9	3.0	3.1	3.1	3.2	3.3	3.4	3.5	3.7	3.8	4.0	4.1	4.3	4.6	4.8
3.5	3.0	3.1	3.1	3.2	3.3	3.4	3.5	3.6	3.7	3.8	4.0	4.2	4.4	4.6	4.8	5.1
4	3.1	3.2	3.2	3.3	3.4	3.5	3.6	3.7	3.9	4.0	4.2	4.3	4.5	4.8	5.0	5.3
4.5	3.2	3.3	3.4	3.4	3.5	3.6	3.7	3.9	4.0	4.2	4.3	4.5	4.7	5.0	5.2	5.5
5	3.3	3.4	3.5	3.5	3.6	3.8	3.9	4.0	4.1	4.3	4.5	4.7	4.9	5.1	5.4	5.7
5.5	3.4	3.5	3.6	3.6	3.8	3.9	4.0	4.1	4.3	4.4	4.6	4.8	5.1	5.3	5.6	5.9
6	3.5	3.6	3.6	3.7	3.9	4.0	4.1	4.2	4.4	4.6	4.8	5.0	5.2	5.5	5.8	6.1
6.5	3.5	3.6	3.7	3.8	3.9	4.1	4.2	4.4	4.5	4.7	4.9	5.1	5.4	5.6	5.9	6.3
7	3.6	3.7	3.8	3.9	4.0	4.2	4.3	4.5	4.6	4.8	5.0	5.2	5.5	5.8	6.1	6.5
7.5	3.7	3.8	3.9	4.0	4.1	4.3	4.4	4.6	4.7	4.9	5.1	5.4	5.6	5.9	6.3	6.6
8	3.8	3.9	4.0	4.1	4.2	4.3	4.5	4.7	4.8	5.0	5.3	5.5	5.8	6.1	6.4	6.8
8.5	3.8	3.9	4.0	4.2	4.3	4.4	4.6	4.8	4.9	5.2	5.4	5.6	5.9	6.2	6.6	7.0
9	3.9	4.0	4.1	4.2	4.4	4.5	4.7	4.9	5.0	5.3	5.5	5.8	6.0	6.4	6.7	7.1
9.5	4.0	4.1	4.2	4.3	4.4	4.6	4.8	4.9	5.1	5.4	5.6	5.9	6.2	6.5	6.9	7.3
10	4.0	4.1	4.2	4.4	4.5	4.7	4.8	5.0	5.2	5.5	5.7	6.0	6.3	6.6	7.0	7.4

All hydration states are calculated by Eq. (3.24)

Table. 3.3. Dielectric constants used in calculating hydration states in table. 3.2

	800	780	760	740	720	700	680	660	640	620	600	580	560	540	520	500
2	4.64	4.94	5.27	5.63	6.03	6.47	6.96	7.49	8.07	8.70	9.39	10.14	10.95	11.82	12.76	13.76
2.5	5.72	6.06	6.43	6.82	7.26	7.73	8.24	8.79	9.39	10.03	10.73	11.48	12.28	13.14	14.07	15.06
3	6.62	6.98	7.37	7.79	8.25	8.74	9.27	9.83	10.44	11.10	11.80	12.55	13.36	14.22	15.14	16.13
3.5	7.38	7.76	8.17	8.61	9.08	9.59	10.13	10.70	11.32	11.99	12.70	13.46	14.27	15.13	16.06	17.05
4	8.04	8.44	8.87	9.32	9.80	10.32	10.87	11.46	12.09	12.76	13.48	14.25	15.06	15.94	16.87	17.86
4.5	8.63	9.04	9.48	9.94	10.44	10.97	11.53	12.13	12.77	13.45	14.18	14.95	15.78	16.66	17.59	18.59
5	9.17	9.59	10.03	10.51	11.01	11.55	12.13	12.73	13.38	14.07	14.81	15.59	16.42	17.31	18.25	19.26
5.5	9.65	10.08	10.54	11.02	11.54	12.09	12.67	13.29	13.94	14.64	15.39	16.18	17.02	17.91	18.86	19.88
6	10.09	10.53	11.00	11.50	12.02	12.58	13.17	13.80	14.46	15.17	15.92	16.72	17.57	18.47	19.43	20.45
6.5	10.51	10.96	11.43	11.93	12.47	13.03	13.63	14.27	14.95	15.66	16.42	17.23	18.09	19.00	19.96	20.99
7	10.89	11.35	11.83	12.35	12.89	13.46	14.07	14.71	15.40	16.12	16.89	17.71	18.57	19.49	20.46	21.50
7.5	11.25	11.72	12.21	12.73	13.28	13.86	14.48	15.13	15.82	16.56	17.33	18.16	19.03	19.96	20.94	21.98
8	11.59	12.07	12.57	13.10	13.65	14.24	14.87	15.53	16.23	16.97	17.75	18.58	19.46	20.40	21.39	22.44
8.5	11.92	12.40	12.91	13.44	14.01	14.60	15.24	15.90	16.61	17.36	18.15	18.99	19.88	20.82	21.82	22.88
9	12.23	12.71	13.23	13.77	14.34	14.95	15.59	16.26	16.98	17.73	18.53	19.38	20.28	21.23	22.23	23.30
9.5	12.52	13.01	13.53	14.08	14.66	15.28	15.92	16.61	17.33	18.09	18.90	19.75	20.66	21.61	22.63	23.70
10	12.80	13.30	13.83	14.39	14.97	15.59	16.24	16.93	17.66	18.43	19.25	20.11	21.02	21.99	23.01	24.09

*All dielectric constants are calculated by the model DEW of Sverjensky et al. (2014)

3. Reference

Akinfiev, N.N. and Diamond, L.W. (2009) A simple predictive model of quartz solubility in water-salt-CO2 systems at temperatures up to 1000 °C and pressures up to 1000 MPa. Geochimica et Cosmochimica Acta, 73, 1597–1608.

Anderson, G.M., Burnham, C.W., (1965) The solubility of quartz in supercritical water. Am. J. Sci. 263, 494–51.

Aranovich, L., Akinfiev, N.N., Golunova, M., (2020) Quartz solubility in sodium carbonate solutions at high pressure and temperature. Chem. Geol. 550, 119699.

Aranovich, L.Y. and Newton, R.C. (1999) Experimental determination of CO_2-H_2O activity-composition relations at 600–1000 °C and 6–14 kbar by reversed decarbonation and dehydration reactions. American Mineralogist, 84, 1319–1332.

Bohlen, S.R. (1984) Equilibria for precise pressure calibration and a frictionless furnace assembly for the piston-cylinder apparatus. Neues Jahrbuch fur Mineralogie Monatshefte, 404-412.

Born M (1920) Volumen und Hydratationswa¨rme der Ionen. Zeitschrift fu¨r Physik, 1, 45–8.

Brooker, J.R. Holloway, R. Herving (1998) Reduction in piston-cylinder experiments: the detection of carbon infiltration into platinum capsules. Am. Mineral., 83 pp. 985-994.

Brooks H. L. and Steele-MacInnis M. (2019) A model for the solubility of minerals in saline aqueous fluids in the crust and upper mantle. Amer. Jour. Sci. 319, 754–787.

Bunham, C. W., (1967) Hydrothermal fluids at the magmatic state, in Barnes, H. L., ed., Geochemisty of Hydrothermal Ore Deposits, 1st ed.: New York, Holt, Rinehart and Winston, p. 34-76.

Chou, I. M., (1978) Calibration of oxygen buffers at elevated P T using the hydrogen fugacity sensor. American lite. Mineralogist, 63, 690–703.

Connolly JAD (1990) Multivariable phase-diagrams an algorithm based on generalized based on generalized thermodynamics American Journal of Science 290:666-718.

Dolejˇ s D, Manning CE. (2010) Thermodynamic model for mineral solubility in aqueous fluids: theory, calibration and application to model fluid-flow systems. Geofluids 10:20–40

Eugster , H. P., & Wones , D. R., (1962) Stability relations of the ferruginous biotite, annite. Petrol. 3, 82-125.

Fournier R. O., Rosenbauer R. J., and Bischoff J. L. (1982) The solubility of quartz in aqueous sodium chloride solutions at 350 °C and 180 to 500 bars. Geochim. Cosmochim. Acta 46, 1969 –1978.

Getsinger, A.J., Hirth, G., Stünitz, H., and Goergen, E.T., 2013, Influence of water on the rheology and strain localization in the lower continental crust: Geochemistry Geophysics Geosystems, v. 14, p. 2247–2264

Harvey, A.H., Lemmon, E.W., (2005) Method for estimating the dielectric constant of natural gas mixtures. Int. J. Thermophys. 26, 31–46.

Heger K., Uematsu M. and Franck E. U. (1980) The static dielectric constant of water at high pressures and temperatures to 500 MPa and 550 °C. Ber. Bunsenges. Phys. Chem. 84, 758–762.

Kennedy, G. C. (1944). Hydrothermal solubility of silica. Econ. Geol., 39, 25-36.

Kennedy G. C. (1950) A portion of the system silica-water. Econ. Geol. 45, 629 – 653.

Keppler, H., (2000) In-situ Raman spectra of dissolved silica species in aqueous fluids to 900 °C and 14 kbar. Am. Mineral. 85, 600–604. 28.

Lasaga AC, Gibbs GV (1990) Ab-initio quantum mechanical calculations of water-rock interactions: adsorption and hydrolysis reactions. American Journal of Science 190: 263-295.

Manning, C.E., (1994) The solubility of quartz in H_2O in the lower crust and upper mantle. Geochim. Cosmochim. Acta 58, 4831–4839.

Manning, C.E., Boettcher, S.L., (1994) Rapid-quench hydrothermal experiments at mantle pressures and temperatures. Am. Mineral. 79, 1153–1158.

Manning, C. E. (2018). Fluids of the lower crust: deep is different. Annu. Rev. Earth Planet. Sci. 46, 67–97.

McKenzie W. F. and Helgeson H. C. (1984) Estimation of the dielectric constant of H_2O from experimental solubilities of quartz and the calculation of the thermodynamic properties of aqueous species to 900 °C at 2 kb. Geochim. Cosmochim. Acta 48, 2167–2177.

Mountain RD, Harvey AH. (2015), Molecular dynamics evaluation of dielectric constant mixing rules for H_2O–CO_2 at geologic conditions. J. Solut. Chem. 44:2179–93.

Mysen BO. (2010) Speciation and mixing behavior of silica-saturated aqueous fluid at high temperature and pressure. Am. Mineral. 95:1807–16.

Newton RC, Manning CE (2000) Quartz solubility in H_2O-NaCl and H_2O-CO_2 solutions at deep crust-upper mantle pressures and and temperatures: 2–15 kbar and 500–900 C. Geochimica et Cosmochimica Acta, 64, 1993–3005.

Newton RC, Manning CE (2002) Solubility of silica in equilibrium with enstatite, forsterite, and H_2O at deep crust/upper mantle pressures and temperatures and an activity- concentration model for polymerization of aqueous silica. Geochimica et Cosmochimica Acta, 66, 4165–76.

Newton RC, Manning CE (2003) Activity coefficient and polymerization of aqueous silica at 800 °C, 12 kbar, from solubility measurements on SiO_2-buffering mineral assemblages. Contributions to Mineralogy and Petrology, 146, 135–43.

Newton RC, Manning CE (2008) Thermodynamics of SiO_2-H_2O fluid near the upper critical end point from quartz solubility measurements at 10 kbar. Earth and Planetary Science Letters, 274, 241–9.

Newton RC, Manning CE (2009) Hydration state and activity of aqueous silica in H_2O-CO_2 fluids at high pressure and temperature. American Mineralogist, 94, 1287–90.

Newton RC, Manning CE (2016) Evidence for SiO_2–NaCl complexing in H_2O–NaCl solutions at high pressure and temperature. Geofluids

Novgorodov, P.G. (1975) Solubility of quartz in H_2O-CO_2 mixtures at 700 °C and pressures of 3 and 5 kbar. Geochemistry International, 12, 122–126.

Pan D., Spanu L., Harrison B., Sverjensky D. A. and Galli G. (2013) The dielectric constant of water under extreme conditions and transport of carbonates in the deep Earth. Proc. Nat. Acad. Sci. 110, 6646–6650.

Shi X., Mao S., Hu J., Zhang J. and Zheng J. (2019) An accurate model for the solubilities of quartz in aqueous NaCl and/or CO2 solutions at temperatures up to 1273 K and pressures up to 20,000 bar. Chem. Geol. 513, 73–87.

Shock, E.L. & Helgeson, H.C. (1988) Calculation of the thermodynamic and transport properties of aqueous species at high pressures and temperatures: Correlation algorithms for ionic aqueous species and equation of state predictions to 5 kb and 1000 °C. Geochimica et Cosmochimica Acta, 52, 2009–2036.

Red'kin AF, Chevichelova TK (1988) Experimental study of solubility of quartz, diaspore and kaolinite with diaspore at 300 °C, 1 kbar and different ionic strength. In: Review of Physical-Chemical Petrology, Vol. 15 (eds Zharikov VA, Fed'kin VV), pp. 134– 142 (in Russian), Moscow, Nauka.

Shmulovich KI, Yardley BWD, Graham CM (2006) Solubility of quartz in crustal fluids:experiments and general equations for salt solutions and H_2O–CO_2 mixtures at 400–800 °C and 0.1– 0.9 GPa. Geofluids, 6, 154–67.

Shmulovich K, Graham C, Yardley BWD. (2001) Quartz, albite and diopside solubilities in H_2O-NaCl and H_2O-CO_2 fluids at 0.5–0.9 GPa. Contrib. Mineral. Petrol. 141:95–108.

Sommerfeld, R.A., (1967) Quartz solution reaction: 400–500 °C, 1000 bars. J. Geophys. Res. 72, 4253–4257.

Sverjensky DA, Harrison B, Azzolini D (2014) Water in the deep Earth: The dielectric constant and the solubilities of quartz and corundum to 60kb and 1200 °C. Geochim Cosmochim Acta 129:125–145.

Sverjensky D. A. (2019) Thermodynamic modelling of fluids from surficial to mantle conditions. Geol. Soc. 176(2), 348–374.

Walther JV, Helgeson HC (1977) Calculation of the thermodynamic properties of aqueous silica and the solubility of quartz and its polymorphs at high pressures and temperatures. American Journal of Science, 277, 1315–51.

Wang, Z., Shi, F., Zhang, J., 2020. Effects of water on the rheology of dominant minerals and rocks in the continental lower crust: a review. J. Earth Sci. 31, 1170–1182.

Walther, J.V., Orville, P.M., (1983) The extraction-quench technique for determination of the thermodynamic properties of solute complexes; applications to quartz solubility in fluid mixtures. Am. Mineral. 68, 731–41.

Wendlandt H. G. and Glemser O. (1963) Reaction of oxides with water at high pressures and temperatures (in German). Angew. Chem. 75, 949–957.

Zhang, Y.-G., Frantz, J.D., (2000) Enstatite–forsterite–water equilibria at elevated temperatures and pressures. Am. Mineral. 85, 918–925.

Zotov N, Keppler H (2000) In-situ Raman spectra of dissolved silica species in aqueous fluid to 900 °C and 14 kbar. American Mineralogist, 85, 600–604.

Zotov, N. and Keppler, H. (2002) Silica speciation in aqueous fluids at high pressures and temperatures. Chemical Geology, 184, 71–82.

Chapter 4. Experimental investigation of silica solubility in the system MgO-SiO_2-H_2O-CO_2: implications for silica and carbon metasomatism in the lower crust and subduction zones

Abstract

Traditional thermodynamic models of metamorphic decarbonation reactions show that they are inefficient at transferring carbon and solutes such as silica from subducting oceanic lithosphere, except at the highest temperatures. However, metasomatic lithologies such as listvenite (magnesite + quartz rocks) and soapstone (magnesite + talc rocks) found in some subduction settings signal Si and C mobility at high pressure. To better constrain this transport, I experimentally investigated the solubility of silica with magnesite in the system MgO-SiO_2-H_2O-CO_2. Aqueous Si concentrations in equilibrium with magnesite were determined by hydrothermal piston-cylinder experiments from 500-800 °C, X_{CO2}= 0.05 and 0.2 at 10 kbar. H_2 fugacity was buffered at hematite-magnetite equilibrium. The solubility of silica was determined through single crystal solubility measurements and a bracketing method to determine X_{Sio2} in equilibrium with magnesite + quartz, magnesite + talc and magnesite + forsterite. Quartz solubility experiments at 500, and 550 °C, in H_2O-CO_2 solutions yield identical values with or without magnesite, indicating no or negligible complexing between MgO and Si. The experimental results verified the new highly accurate thermodynamic model capable of predicting X_{SiO2} in the MSCOH system. The model shows that the small addition of CO_2 results in magnesite stability and increasing X_{SiO2} with decreasing temperature along key silica buffering

equilibria. The results provide a foundation for modeling coupled carbon and silica transport in high-pressure settings.

4.1 Introduction

Carbon is a major constituent in crustal and mantle fluids. It may be present as both dissolved ionic and molecular species. At modest pressures and temperatures, carbon species become fully miscible with H_2O, enabling deep crustal and mantle fluids to become highly enriched in carbon. Elevated carbon contents strongly influence the nature of fluid-rock interaction in deep environments. For example, carbon present as carbonate species influences pH, and thus the solubility of rock-forming components (e.g., Manning 2013). Carbon present as dissolved gases (CO_2 or CH_4) reduces H_2O activity and the solubilities of key minerals, such as quartz (e.g., Newton and Manning 2000, Fineman 2022, and other references from chapter 1).

Because silica is typically the most soluble major rock forming oxide, geologic environments where there are strong contrasts in silica content can be zones of significant metasomatic mass transfer. In practice, such settings typically involve juxtaposition of Si-poor ultramafic rocks and Si-rich quartz-saturated rocks. A key example is the slab-mantle interface in subduction zones, where subducted sediments are commonly in direct contact with ultramafic rocks of the mantle wedge. In cases where sediment derived fluids contain substantial carbon, complex carbon-silica mass transfer may arise leading to the development of well-known metasomatic rocks such as soapstone, ophicarbonates, listvenites, and sagvandites. In these rocks, mineral assemblages involving magnesite and a silicate mineral (quartz, talc, forsterite, enstatite) are common products of combined carbon and Si metasomatism. Thermodynamic modeling allows quantification of the extent of mass transfer associated with formation of these

assemblages; however, for high pressure environments in particular, the methods require substantial extrapolation of models and lack direct experimental constraints.

To provide quantitative constraints on CO_2 and silica metasomatism at high pressure and temperature, I carried out a series of experiments at 10 kbar, 500-800°C, in the system MgO-SiO_2-H_2O-CO_2 (MSCOH) at a range of silica and CO_2 activities. The experiments constrain silica solubility in mixed fluids at conditions relevant for mantle metasomatism. The results allow comparison to predictions from thermodynamic models and provide a basis for evaluating metasomatic mass transfer using classic reaction-progress methods (e.g., Ferry 1994).

4.2 Methods

Experiments were conducted at two starting fluid compositions, $X_{CO2} = 0.05$ and $X_{CO2} = 0.20$, where $X_{CO2} = n_{CO2}/(n_{CO2} + n_{H2O})$ and n stands for moles). These CO_2 compositions were chosen to (1) allow comparison to my results on magnesite solubility (Chapter 2), and (2) to cover the range of CO_2 contents thought to be relevant to subduction zones, where high pressure, modest temperature and lithologic controls limit fluid X_{CO2} to lower values than are common in crustal metamorphism. Dissolved silica concentrations were established using a combination of direct solubility measurements and phase-boundary bracketing methods.

As in Chapters 2 and 3, Oxalic acid dihydrate (OAD: $(COOH)_2 \cdot 2H_2O$) was used as a carbon source and during break down produces H_2, resulting in graphite precipitation if not removed. In selected experiments, silver oxalate ($Ag_2C_2O_4$, (AgOX) was used instead of OAD. Unlike OAD, AgOX does not produces H_2 when it breaks down to Ag + CO_2 upon initial run heating. However, an internal buffer must still be used to produce high oxygen fugacity (f_{O2}) and maintain an H_2O-CO_2 fluid. The principles of O_2 buffering are outlined in Chapter 2. In this

study, two different capsule configurations were used to achieve fixed f_{O2} in the experiments, as outlined below.

4.2.1. Starting materials

Experiments used various combinations of single crystals of magnesite, forsterite and quartz, along with additional SiO_2, H_2O, OAD and AgOX. All runs used ultra-pure 18-MΩ-cm water to minimize the introduction of contaminating ions. Oxalic acid dihydrate was from Fisher Chemical (99.998% pure). I used natural magnesite crystals from Pomba Pit, Serra das Eguas, Brumado, Brazil. Electron probe analysis showed a maximum departure from $MgCO_3$ composition of 0.217 wt% FeO and 0.008 wt% CaO. Magnesite single crystals were cleaved to rhombohedra with a razor blade and sonicated in ethanol to dislodge any small fragmentary crystals and impurities clinging to the sample. Cleaved magnesite crystals with visible fluid inclusions were discarded.

Starting forsterite crystals were chips from a large synthetic forsterite crystal grown by a flux-melt method by H. Takei (Takei and Hosoya, 1985). Forsterite chips were polished to roughly cylindrical shapes using a diamond file and abrasive paper, then cleaned with distilled H_2O in an ultrasonic bath. Synthetic forsterite chips with visible flux inclusions were discarded.

Quartz was taken from natural Brazilian crystals (Manning 1994). Individual crystals were ground and polished to roughly spherical shape using a diamond file and abrasive paper, then cleaned with distilled H_2O in an ultrasonic bath and dried in a 110 °C oven.

A key aspect of this study was tailoring the silica content of the fluid to identify phase boundaries or to force congruent dissolution for quantitative solubility measurements (see below). This was done by adding ultrafine silica “float” (Fisher Scientific). This synthetic

material is nanoscale amorphous silica, which rapidly dissolves on initial heating to provide a nominal starting solution of a desired SiO_2 concentration.

4.2.2. Capsule assembly

Two capsule configurations were used depending on the temperature. Capsule configuration 1 was employed between 500 – 600 °C and involved a double-capsule geometry similar to Eugster and Wones (1962). An inner Pt capsule containing starting materials was placed inside a gold outer capsule containing hematite + water. In contrast, capsule configuration 2, which was employed in experiments at >600 °C, used a triple-capsule approach similar to Manning and Boettcher (1994), in which two small inner capsules, one with starting materials and one with the f_{O2} buffer, were placed in a larger capsule containing H_2O and OAD or AgOX. Weighing of all materials was carried out with a Mettler Toledo UMX20 ultramicrobalance with an uncertainty of 1σ= 0.2 μg). Unless otherwise noted, welding was conducted with a LAMPERT PUK-5 precision welder, at 14% power and 4 ms. Details of the loading methods are given below.

4.2.2.1 Capsule configuration 1

Capsule configuration 1 employed a 4.5 mm outer diameter (OD) gold tube that was 18 mm long, and an inner capsule made of 2.5 mm OD Pt tubing 10 mm in length. All tubes were cleaned with acetone and annealed using a Bunsen burner. The inner Pt tubes were crimped and welded on one side. The desired weight of OAD, the silica source and a single rhombohedra magnesite crystal were then added. Depending on the run temperature, the silica source was silica float or a rounded quartz sphere. I then added H_2O by a microliter syringe and allowed it to

evaporate until the desired weight was achieved. The capsule was then immediately crimped shut, weighed, and welded shut. Typical weight loss upon welding was <0.02 mg.

The outer gold tubes were crimped on one side and welded shut. The inner Pt capsule was then placed within the outer capsule, and the remaining space was packed with hematite. 5.0 mg of H_2O was by a syringe, then the outer capsule was welded it shut. The addition of H_2O increases the rate of the f_{O2} buffer reaction. During the experiment, H_2 produced from OAD results in a large H_2 chemical potential difference between the inner capsule fluid and the surrounding hematite buffer. At experimental conditions, the Pt walls of the inner capsule are permeable to H_2 (Chou et al. 1978; Eugster and Wones 1962). This facilitates hydrogen diffusion into the surrounding hematite, which partially converts to magnetite, fixing the fugacity of O_2. Thus, the f_{O2} inside the Pt capsule is in equilibrium with the HM buffer, which is greater than that of the CO_2-graphite equilibrium, thus suppressing graphite formation and ensuring negligible H_2 within the H_2O-CO_2-SiO_2-MgO fluid. The outer gold capsule is less permeable to hydrogen infiltration than Pt and limits the introduction of hydrogen from the surroundings.

4.2.2.2 Capsule configuration 2

In capsule configuration 2, two inner capsules were used. Each was made from 1.5 mm OD Pt tubing 5 mm in length. One served as a magnesite or forsterite sample holder and the other as an f_{O2} buffer. The outer capsule was produced from a 3.5 mm OD Pt tube, 18 mm in length. All Pt tubes were cleaned with acetone and annealed using a Bunsen burner. This configuration was used to increase the fluid volume and maintain consistent $X_{SiO2,aq}$ at a greater weight of silica float in the experiment.

To make the crystal sample holder, I used an acetylene torch to melt the edges of one side of a 1.5 mm OD Pt tube, 5 mm in length. A single magnesite or forsterite crystal of measured weight was added and the capsule was crimped shut. The capsule was then perforated twice with a needle on the opposite side of the crimped end and burnished to remove any loose Pt slivers. The inner capsule was then weighed. The perforations allow fluid and the crystal to interact and equilibrate during the experiment. The inner capsule helped retain any crystal fragments that might dislodge during the experiment, and minimized consequences of quench precipitation.

The second inner capsule was crimped and welded on one side, packed with a MnO_2-water mixture, then crimped and welded shut. This capsule served as an internal buffer capsule, which was required to consume H_2 from the breakdown of hydrous oxalic acid and maintain oxidizing conditions.

Outer capsules were created by crimping at one end then welding. Pt was used in magnesite experiments. In these cases, I used a graphite arc welder. Experiments on forsterite solubility used a Au outer capsule; welding was done with the LAMPERT PUK-5 precision welder, but required 16% power and 5 ms. In all cases, outer capsules were filled with, in order, the desired weights of OAD and silica float, then the inner capsules, and finally H_2O, which was added with a microliter syringe and allowed to evaporate until the desired weight was achieved. The outer capsule was then crimped, weighed, and welded shut.

4.2.3. Experimental apparatus and assembly

All experiments were conducted in an end-loaded piston cylinder apparatus with 2.54 cm diameter piston, NaCl pressure medium, and a graphite heater sleeve. Temperature was controlled by a Pt-$Pt_{90}Rh_{10}$ thermocouple with an estimated accuracy of ±3 °C (Bohlen 1984;

Manning and Boettcher 1994), and pressure was measured with a Heise Bordon tube gauge that has an estimated uncertainty of ±3 kbar. All experiments were conducted at 10 kbar using the piston-out technique, in which assemblies were first cold pressurized to 70% of the final value before temperature was increased. Thermal expansion of the assemblies during the subsequent heating raised the pressure to the target pressure of 10 kbar . Pressure was held within ±150 bars of the desired pressure through the duration of the experiment by bleeding pressure when necessary. At final run conditions, the NaCl cells are frictionless and require no pressure correction (Manning and Boettcher 1994).

4.2.4 Quenching and run-product retrieval

Experiments were terminated by switching off the electrical heating power. Temperatures dropped to 200 °C in <35 seconds. Quenched capsules were retrieved from the furnace assembly and soaked in distilled water to dissolve any adhering NaCl. Retrieved capsules were inflated due elevated vapor pressure of CO_2 exsolved from the fluid on quenching. This provided a visual indication of a capsule integrity, which was the first step in verifying run success. The capsule was then weighed to provide a quantitative test to determine that no volatile loss occurred. Capsules that showed volatile loss were discarded. For experiments between 500 – 700 °C, the outer gold capsules were carefully cut open with a razor blade and inner Pt capsule was retrieved, cleaned and weighed to ensure no volatile loss. We then checked to ensure that f_{O2} buffer capacity had not been exhausted. Exhausted MnO_2 buffers displayed a pistachio green color, indicating a full conversion to MnO. Hematite buffers underwent a streak test and were ground dry using a pestle on a porcelain plate. The absence of a red color indicated the exhaustion of the hematite and full conversion to magnetite. In both cases, full conversion to

MnO or magnetite indicated that f_{O2} buffer capacity was exhausted. These runs were discarded due to the possibility that f_{O2} was low enough that other carbon species were non-negligible. In some cases, f_{O2} lower than graphite-CO_2 equilibrium was indicated by graphite in the charge; these runs were discarded. The inner capsules of successful runs were carefully punctured in a weighing boat and dried, ensuring no material was lost. All run products were carefully examined using optical and scanning electron microscopy.

4.2.5 Adaptation of experimental approach

Extensive initial experimentation showed that magnesite crystals could not reliably be retrieved and weighed at the completion of an experiment. The experimental approach was therefore modified such that, in experiments involving magnesite, its presence or absence was noted along with relevant textures. No further attempts were made to optimize experimental design for weighing magnesite after runs.

In light of this, I adapted my experimental methods so that, for most runs, a bracketing approach was used to establish the Si content of fluids saturated with magnesite and either talc or forsterite. The phase boundaries were determined by performing multiple runs at the same P, T and X_{CO2} but changing the concentration of silica float to establish where magnesite alone was stable as opposed to magnesite + talc or forsterite.

For experiments where quartz and magnesite are stable together, quartz could be retrieved and weighed to give a direct determination of Si concentration in the fluid. Several runs were also conducted at conditions where forsterite dissolved congruently, again allowing direct determination of Si (and Mg) content of the fluid.

4.3. Experimental results

Experimental results are presented in tables 4.1-4.2 and Figures 4.2A and B In the following discussion, the mole fraction of solvent component *i* in a solution is

$$X_i = \frac{n_i}{n_{SiO2}+n_{H_2O}+n_{CO_2}+n_{Sio2}} \quad (4.1)$$

Because all experiments were conducted at 10 kbar , the results constrain isobaric metasomatic phase relations at two nominal fluid compositions, X_{CO2} = 0.05 and 0.20. Results are presented below in terms of assemblages observed with increasing temperature.

4.3.1. Magnesite + quartz

Coexisting magnesite + quartz were observed at the lowest temperatures (Table 4.1): 500°C at X_{CO2} = 0.05 (Fig. 4.2A, and 500-550 °C at X_{CO2} = 0.20 (Fig. 4.2B) Run times needed for equilibrium were assumed the same as those established in Chapter 3. This was confirmed by comparing quartz solubility with and without magnesite at 500 °C. Figure 4.2C shows that results consistent with those in Chapter 3 were obtained when magnesite was present at X_{CO2} = 0.05 (MGFO_101, 72 hr) and X_{CO2} = 0.20 (MGFO_82, 30 hr; MGFO_87, 72 hr). Similar results were observed at 550 °C (MGFO_83, 24 hr: MGFO_90, 42hr). Textures of quartz crystals were similar to those described in Chapter 3.

4.3.2. Magnesite + talc

At intermediate temperatures, runs with excess silica yielded talc overgrowths on magnesite crystals (Table 4.1). Talc formed as hexagonal platelets (Fig. 4.1A/B, MGFO_77 and

54) and was confirmed by X-ray diffraction of selected run products based on the presence of diagnostic peaks at 28.59, 18.97 and 19.39 degrees 2θ. Talc formation was seen in as little as 0.5 hr at 600 °C and X_{CO2} = 0.2 (MGFO_56), indicating that comparatively short run times were sufficient to establish magnesite-talc equilibrium.

The magnesite-talc phase boundary (Fig. 4.2A and B) is constrained by these experiments to lie between runs in which X_{SiO2} was too low to form talc and those in which initial X_{SiO2} was sufficiently high that talc nucleated and grew. Reaction progress in the latter case was always incomplete because excess talc prevented full conversion. As noted above, the inability to separate the phases and weigh the magnesite (or talc) means that such runs provide only an indication that the phase boundary must lie below the initial X_{SiO2} value of the run. Thus, the lowest initial X_{SiO2} at which talc grew combined with the highest X_{SiO2} in which no talc was found bracket the phase boundary. Notably, experiments providing the upper bound to the talc + magnesite univariant line showed very small volumes of talc. However, even at small volumes talc formation was readily confirmed by reflected light optical microscopy, which clearly illuminated single talc crystals that often formed within dissolution grooves on the magnesite surface.

Results for bracketed magnesite + talc equilibrium are plotted in Fig. 4.2A and B as open upward facing triangles for undersaturated fluids and downward open facing arrows for silica oversaturated fluids. The silica concentrations in equilibrium with magnesite + talc was determined by using the midpoint between magnesite + fluid and magnesite + talc + fluid. At 600 and 550 °C, X_{CO2} = 0.05, the midpoints indicated $X_{SiO2,aq}$ = 1.32E-03 and 1.68E-03, respectively. At X_{CO2} = 0.2, 700, 650 and 600 °C, $X_{SiO2,aq}$ = 1.35e-3 , 1.54e-3 and 1.87e-3 respectively. The results indicate that the fluid SiO_2 concentration in equilibrium with magnesite

+ talc decreases as temperature rises at both CO_2 contents, in contrast to the solubility curve for quartz (Fig. 4.2A and B). Notably, at a given temperature, the experiments indicate that as X_{CO2} increases, the concentration of dissolved silica along the magnesite-talc phase boundary increases.

4.3.3. Forsterite and forsterite + magnesite

At the highest temperatures, forsterite is the stable phase with magnesite at the investigated X_{CO2}. Initial experiments using capsule configuration 2 with a magnesite-bearing inner capsule encountered multiple problems at ≥700 °C. First, use of a Pt outer capsule led buffer exhaustion before equilibration, however in highly oversaturated X_{si} fluids euhedral forsterite crystals where still seen (Fig. 4.1C, MGFO_13). It was found that Au could be used as an alternative, allowing experimental run times in excess of 30 hours. One experiment at 800 °C, X_{CO2} = 0.05 (MGFO_Gold, Table 4.1) yielded growth of forsterite crystals at low $X_{SiO2,aq}$ (Fig. 4.1D) (MGFO_Gold, Table. 2). However, the amount of excess Si needed to prevent forsterite growth was less than 12 μg, which was too low to be accurately weighed. Magnesite vapor transport crystals were also present in the fluid after the run. It was also found that experiments at X_{CO2} = 0.20 resulted in failure of the gold capsule due to the high internal pressure of CO_2 gas during decompression of the experiment which resulted in the explosion of the gold capsule during quenching. Evidently, Au is more brittle than Pt, and Au capsule cannot deform to accommodate the volume increase associated with CO_2 exsolution.

The problems encountered above led me to modify my experimental approach. Instead of starting with a single crystal of magnesite, an inner capsule with a single forsterite crystal was used, and further high-T runs were limited to X_{CO2} = 0.05. Initial experiments at 800 °C showed

that forsterite dissolved congruently without added SiO_2. I took advantage of this to confirm that Pt capsules resulted in rapid buffer exhaustion. Forsterite solubility was determined at 800 °C, $X_{CO2} = 0.05$, as a function of time. Figure 4.2D shows that the solubility increases to a maximum, then declines to a very low value, presumably because of change in the fluid composition due to buffer exhaustion. Experiments using a Au outer capsule appear to yield a constant solubility independent of run time. Au capsules and run times in excess of 38 hr were used for all subsequent runs.

Results are given in Table 4.2 and depicted in Fig. 4.2A and B. The congruent dissolution of forsterite without added silica at ≥750 °C gives X_{SiO2} greater than the forsterite-magnesite phase boundary at these T. Decreasing T to 725 °C yielded magnesite overgrowths on forsterite (e.g., Fig. 4.1E, FOCO_14), bracketing the phase boundary in terms of both T and X_{SiO2} (Fig. 4.2A). The phase boundary was located at T ≤725 °C by adding SiO_2 float until forsterite again dissolved congruently. The addition of silica yielded congruent forsterite dissolution; however, it often resulted in numerous, small forsterite crystals that grew throughout the capsule (Fig. 4.1F). When possible as many of the small crystals were collected. However, it proved impossible to ensure that all crystals were collected, so all such experiments must be considered maximum constraints on X_{Sio2}.

As with magnesite-talc, the results indicate that the fluid SiO_2 concentration in equilibrium with magnesite-forsterite decreases as temperature rises (Fig. 4.2B). Moreover, the forsterite + magnesite isotherm has a steeper negative slope than that of magnesite + talc. The change in slope indicates the location of the magnesite-talc-forsterite invariant point in the phase diagram.

4.4. Discussion

4.4.1 Comparison of experimental results to predictions

The experimental results provide constraints on Si concentrations in H_2O-CO_2 fluids in the MSCOH system. The data can be compared to predicted X_{si} concentrations for the relevant phase boundaries (univariant equilibria; Table 4.3) using thermodynamic models for dissolved silica. There are two sources of such data at the conditions of the experiments: (1) a model derived from a series of papers by Newton and Manning (2002, 2003, 2008, 2009) along with my results from Chapter 3, and (2) the Deep Earth Water model (Sverjensky et al 2014). I used both approaches to compute theoretical T-X_{SiO2} phase diagrams, as in Fig. 4.2A and B, for comparison with the experimental data.

4.4.1.1 The Newton and Manning model framework

This approach extends the model for dissolved SiO_2 discussed in Chapter 4.3 to quartz-undersaturated conditions. A first step involves modifying the Newton and Manning (2008) equation for the standard state Gibbs free energy of the SiO_2 monomer because my work (Chapter 4.3) indicates that it does not extrapolate well to T < 700 °C. I then use the new equation to compute Si concentrations for the relevant phase boundaries.

4.4.1.1.1 A new equation for the Gibbs free energy of the silica monomer

Calculating the standard state Gibbs free energy of aqueous silica at crustal and mantle conditions is a prerequisite for quantitatively describing the chemical equilibrium of

hydrothermal systems. Newton and Manning (2008) built on data from Newton and Manning (2002) for Si concentrations buffered by the following equilibria:

$$SiO_2 = SiO_{2,aq} \quad (4.2)$$

quartz monomer

and

$$Mg_2SiO_4 + SiO_{2,aq} = 2MgSiO_3 \quad (4.3)$$

forsterite monomer enstatite

to calculate the standard state Gibbs free energy of the silica monomer $\Delta G°_m$ between 700-900 °C and 10 kbar . In this derivation, the hydration state of the monomer (Chapter 3) is neglected because the experiments were in pure H_2O, for which $a_{H2O} = 1$. As outlined in Chapter 3, the standard state for $SiO_{2,aq}$ is taken to be the hypothetical solution with a unit mole fraction of monomers (X_m) referred to infinite dilution, which allows derivation of a model for speciation of silica monomers and dimers in mixed H_2O-CO_2 fluids. However, the Newton and Manning model does not extrapolate well to T < 700 °C. The determination of a new $\Delta G°_m$ at temperatures < 700 °C is required to accurately predict equilibrium between aqueous silica and rock-forming assemblages in the MSCOH system below 700 °C.

I followed the same approach as Newton and Manning (2008) to derive an equation for the standard Gibbs energy of Reaction 4.2 at 10 kbar , 500-800 °C, using my new quartz

solubility measurements described Chapter 3. A simple polynomial equation gives $\Delta G°_{qm}$ (Eq. 4.2) at 500 – 850 °C and 10 kbar :

$$\Delta G°_{qm} = 3.3162(T)^2 *10^{-5} - 1.89668*T*10^{-2} + 39.6453 \quad (4.4)$$

where T is in °C and $\Delta G°_{qm}$ is in kJ mol^{-1}.

Figure 4.3 compares Newton and Manning (2008) and Eq. (4.4). The two equations agree between 700 and 800 °C but diverge at lower T. Whereas Eq. (4.4) correctly predicts quartz solubility at 500 °C, the Newton and Manning (2008) equation is off by 80 %. The expanded range for $\Delta G°_{qm}$ can be used with values for $\Delta G°_{q}$ to calculate the standard state Gibbs free energy of the monomer ($\Delta G°_{m}$), which allows prediction of total silica concentrations in the MSCOH system.

4.4.1.1.2. X_{SiO2} of silica-buffering reactions

Following Newton and Manning (2002, 2008, 2016), I derived a modified thermodynamic approach capable of predicting $X_{SiO2,aq}$ for Si-buffering equilibria in the MSCOH system. The new model permits $X_{SiO2,aq}$ to be calculated in $a_{H2O} < 1$, and accounts for both silica polymerization and hydration as a function of P and T. The model relies on five important assumptions: 1) The activity of silica is ideal 2) quartz dissolves only as monomers and dimers 3) no complexing occurs between Mg and Si or C and Si 4) the activity of SiO_{2aq} is unaffected by the presence of other aqueous spices 5) CO_2 acts only as an inert diluent which lowers the a_{H2O}.

T-X_{SiO2} phase diagrams at fixed X_{CO2} were computed by calculating X_{SiO2} for all stable univariant reactions. The thermodynamic data set of Holland and Powell (1998; 2002 update;

hereafter referred to as HP02) was used for minerals because the results of Koziol and Newton (1995) on key decarbonation equilibria in the MSCOH system are better fit by the Holland and Powell (1998) data base compared to the Berman (1988). The activities of H_2O and CO_2 were derived using the model of Aranovich and Newton (1998). Standard states for minerals and fluids were unit activity of the pure phase at any P and T.

As an example of the approach, consider the magnesite-talc equilibrium neglecting SiO_{2aq} hydration:

$$3MgCO_3 + 4SiO_{2,aq} + H_2O = 3CO_2 + Mg_3Si_4O_{10}(OH)_2 \quad (4.5)$$

magnesite monomer talc

The equilibrium constant for Eq. (4.5) is

$$K_{mag-ta} = exp\left(\frac{-(G°_{talc}+3G°_{CO2}-3G°_{magesite}-4G°_{m}-G°_{H2O})}{RT}\right) \quad (4.6)$$

where *R* is the ideal gas constant and T is in Kelvins. The standard state Gibbs free energies of magnesite, talc, quartz, CO_2 and H_2O were calculated with the software package PERPLE_X version 6.8.3_OS_X_10.6 using the HP02 database. The standard Gibbs free energy of the silica monomer is calculated using Eq. (4.4) and $\Delta G°_q$. Assuming pure minerals, the law of mass action gives:

$$K_{mag-ta} = \frac{a_{CO2}^3}{a_m^4 a_{H2O}} \quad (4.7)$$

Where *a* is activity of the subscripted species. Equation (4.7) can be solved for SiO_{2aq} activity and, by the standard state convention, X_m

$$X_m = a_m = \left(\frac{a_{CO2}^3}{K_{mag-ta} a_{H2O}}\right)^{1/4} \quad (4.8)$$

Eq (4.8) is adequate for pure water; however, assessing variation in silica concentration in mixed fluids requires consideration of silica hydration. Because monomer hydration takes the form

$$SiO_{2,aq} + nH_2O = Si(OH)_4 \cdot (n-2)H_2O \quad (4.9)$$

Eq. (4.8) becomes

$$X_m = a_m = \left(\frac{a_{CO2}^3 a_{H2O}^{4n-1}}{K_{mag-ta}}\right)^{1/4} \quad (4.10)$$

The activity of H_2O and CO_2 are calculated from Aranovich and Newton (1998) and *n* is determined by

$$n = 2.0\ exp(0.0545 * \varepsilon) \quad (4.11)$$

(Chapter 3). The total mole fraction of dissolved silica at magnesite-talc equilibrium can then be determined as in Chapter 3 (Eq. 3.19-3.21). The same approach was used to compute X_{SiO2} for all stable phase boundaries (Table 4.3).

4.4.1.1.3. Calculating X_{SiO2}: The Deep Earth Water model

Unlike Newton and Manning (2002, 2003, 2016), the DEW model (Sverjensky et al. 2014; Fang and Sverjensky 2019) takes the standard state for aqueous species to be unity activity of a hypothetical 1.0 molal solution, referenced to infinite dilution at the temperature and pressure of interest. To compare the two models, the concentration of the aqueous silica species predicted by DEW must be converted into mole fractions. In addition, the DEW model is based on the Berman (1988) thermodynamic data set for minerals. However, for the purposes of comparison I use the HP02 data set instead. Using Berman (1988) for this study would result in trivially different invariant points and univariant lines for reactions in Table 2.1 and X_{SiO2}. Activities of H_2O and CO_2 were calculated with the CORK model (Holland and Powell 1991).

The DEW model includes thermodynamic data for the silica dimer and trimer, rather than the monomer and dimer alone as in the Newton and Manning model. Although the concentration of the trimer is negligible at these conditions, it was included for completeness. The molalities of the dimer and trimer were calculated as follows

$$2SiO_{2,aq} = Si_2O_{4,aq} \quad (4.12)$$

And

$$2SiO_{2,aq} = Si_3O_{6,aq} \tag{4.13}$$

The equilibrium constants for equation (4.12) and (4.13) are

$$K_{4.12} = \frac{a_d}{a_m^2} \tag{4.14}$$

and

$$K_{4.13} = \frac{a_t}{a_m^3} \tag{4.15}$$

The concentration of X_m can then be calculated through

$$X_m = \left(\frac{a_m^\circ}{a_m^\circ + a_d^\circ + a_t^\circ + 55.51}\right) a_{H2O}^n \tag{4.16}$$

where a_{H2O} is the activity of H_2O, n is the hydration state of the monomer (Eq. 4.11), and 55.51 is the number of moles of 1kg of H_2O. The mole fraction of the dimer and trimer are then

$$X_d = \left(\frac{K_{4.12} X_m^2}{a_{H2O}}\right) \tag{4.17}$$

and

$$X_t = \left(\frac{K_{4.13} X_m^3}{a_{H2O}}\right) \tag{4.18}$$

Where upper case $K_{4.12}$and $K_{4.12}$ are in the mole fraction scale. Finally, the total silica content of the fluid is determined from

$$X_{SiO2} = X_m + 2X_d + 3X_t \quad (4.19)$$

4.4.2 Comparison of predicted and measured X_{SiO2}

Figure 4.4 compares my experimental results to calculated T-X_{SiO2} phase relations for reactions in table (4.3) at 10 kbar , 500 to 800 °C, using the two approaches outlined above. The black lines represent the calculated $X_{SiO2,}$ using the modified Newton and Manning (2008) model and the red lines represent X_{SiO2} calculated using the DEW model. Overall, agreement between the experimental and predicted phase relations is excellent. Both models accurately reproduce the X_{SiO2} of the magnesite-talc and magnesite-forsterite phase boundaries. Similarly, the predicted positions of the magnesite-talc-quartz and magnesite-talc-forsterite phase boundaries are consistent with experimental results. Data from Chapter 3 on quartz solubility are also included in Fig. 4.4 and illustrate that both models yield generally accurate predictions of quartz solubility. The models confirm the negative slopes of the experimentally derived magnesite-talc and magnesite-forsterite phase boundaries, and also predict that increasing X_{CO2} at a given T enhances $X_{SiO2,total}$ at magnesite-talc and magnesite-forsterite equilibrium.

In detail, my modified Newton-Manning model is slightly more accurate at 700-800 °C, where it returns X_{SiO2} in better agreement with experimental results on quartz and magnesite-forsterite solubilities. Minor discrepancies between the experimental and predicted X_{SiO2} along

the magnesite + forsterite at 750-800, X_{CO2} = 0.05, may reflect degraded accuracy in the experiments, because of the challenges of working at very low X_{SiO2} and the abundance of forsterite vapor transport crystals that were too difficult to collect completely. The experimental data at X_{CO2} = 0.05, suggest that the magnesite + quartz invariant point is slightly greater then 500 °C, whereas the calculations predict that it is just under 500 °C. At X_{CO2} = 0.2 it is possible that my experiments are slightly metastable with respect to magnesite-enstatite equilibrium; no enstatite was observed in any run products.

In general, the significant agreement between the predicted and experimental T-X_{SiO2} phase relations is consistent with arguments above for chemical equilibrium in the runs, and form the basis for drawing three further conclusions. First, the nearly identical predicted and measured X_{SiO2} at quartz solubility in H_2O-CO_2 with and without magnesite (Figs. 4.2C and 4.4) indicates that any Mg-Si or Si-C complexing in the fluid is negligible, as such species were not included in calculating the phase boundaries in Fig.,4.4. in contrast, my results demonstrate that forsterite solubility in low X_{CO2} fluids at 800 °C is 3 times greater than that in pure H_2O reported by Macris (2020). This implies non-negligible Mg-C complexing, which should be taken into account in cases where Mg mass transfer is important (though this is beyond the scope of the present study).

Second, agreement between the experimental data and the modified Newton-Manning model is consistent with the inference that silica trimers and higher oligomers are negligible at T≤800 °C at 10 kbar . Neglecting trimers in the DEW model yields nearly identical phase boundaries. In short, phase relations involving silica in MSCOH fluids at the conditions of this study can be modeled exclusively as monomers and dimers.

Finally, the agreement between experiment and theory gives confidence that the predicted positions of additional phase boundaries are accurate. Figure 4.4 shows predicted positions of three additional phase boundaries: talc-forsterite, talc-enstatite, and enstatite-talc. All lie at higher X_{SiO2} than were investigated experimentally.

4.4.3. Predicted T-X_{SiO2} phase relations

The agreement between experiment and theory provides a basis for evaluating the evolution of T-X_{SiO2} phase relations in the MSCOH system from pure H_2O to X_{CO2} at least as high as 0.4 (Fig. 4.5). Phase equilibria calculated with both modeling approaches are included. As above, the differences are generally minor, though it can be seen that greater discrepancies emerge at the lowest X_{SiO2}.

Figure 4.5 shows that the addition of CO_2 causes key changes in the phase relations. First, as demonstrated in Chapter 3, quartz solubility declines with rising CO_2. Next, the addition of even a small amount of CO_2 stabilizes magnesite such that it has a comparatively large stability field (Fig. 4.5B). High H_2O phases such as antigorite and brucite rapidly become unstable. The range of X_{SiO2} at which magnesite is stable greatly expands with increasing X_{CO2}.

The phase relations depicted in Fig. 4.5 reveal an intriguing behavior. Consider a system at constant X_{CO2}, initially in equilibrium with magnesite and forsterite. The fluid will have very low X_{SiO2} regardless of CO_2 content. However, as temperature declines, the X_{SiO2} buffered by this mineral pair increases. The effect becomes less pronounced when talc instead of forsterite becomes stable with magnesite. Nevertheless, the general trend of increasing X_{SiO2} with

declining T persists. Only at T sufficiently low to yield quartz saturation does X_{SiO2} then decline with further T decrease. This observation has important implications for the coupling between CO_2 and SiO_2 during metasomatic mass transfer. The implications are explored in the next section. The enhancement of X_{SiO2} due to magnesite stability has not previously been documented and must be experimentally verified.

4.4.4 Application to the mantle wedge: silica metasomatism in carbonated ultramafic rocks

Open system processes control the rate of carbon subduction into the mantle and decarbonation and dehydration reactions facilitate the migration of highly reactive carbon-rich fluids along the subducting slab and into the mantle wedge. Although carbon-rich fluids have been recognized as important agents of element metasomatism, quantification of relevant reactions and pathways has lacked experimental validation of model extrapolation to mixed fluids. Here I use coupled C and Si metasomatism in the mantle wedge above subduction zones to demonstrate the utility of the experimental results of this study.

The modeling approach involves extension of methods develop by Ferry (1994). Ferry showed how metamorphic reactions driven by infiltration of fluid into a rock can be used to monitor the extent of fluid-rock interaction and fluid magnitudes. The progress of an infiltration reaction, ξ, is related to the change in abundance of a phase involved in the reaction via

$$\xi = \frac{\Delta n_a}{v_a} \tag{4.20}$$

where Δn_a is the change in quantity, here the number of moles, of species *a* in the rock resulting from reaction, and v_a is the stoichiometric coefficient of *a* in the reaction. Fluid interacting with an arbitrary volume of rock will result in mineral-fluid reaction, during which species will either be released to the fluid by the rock, absorbed by the rock from the fluid or both. Ferry (1994) showed that the progress of a reaction is related to the total number of moles of fluid (n_T) involved in driving the reaction:

$$n_T = \xi \frac{\nu_i - X_i^f (\Sigma_j \nu_j)}{\left(X_i^f - X_i^o\right)} \tag{4.21}$$

where X_i is the mole fraction of species *i* in the fluid, superscripts ° and *f* refer to the concentrations of *i* before and after fluid-rock reaction, and the sum is taken over all mobile species *j* including *i*, that participate in the mineral-fluid reaction. Manning (1995) used this approach to determine the reaction progress of a silica-saturated metasomatizing fluid interacting with an already fully hydrated peridotite to understand the silicification of ultramafic rocks along three subduction zone pathways. However, his analysis focused on the slab-mantle interface and did not account for the role of CO_2, which is a common component of fluids derived from subducted lithologies including metasediments, metabasalt and serpentinite.

In order to understand the effects of H_2O-CO_2-SiO_2 fluids on ultramafic rocks, a thermodynamic model capable of predicting the concentration of silica buffered by quartz undersaturated lithologies in H_2O-CO_2 solutions is required. Although complex thermodynamic models such as the Deep Earth Water model (DEW) of Sverjensky et al (2014) have gained considerable attention in the geochemistry community, it alone is not capable of predicting the

solubility of aqueous species in fluids with reduced H_2O activity, which are common during metamorphism. In light of this and the better fit to the experimental results of this Chapter (3), I use my modified Newton and Manning (2008) model for this example.

4.4.4.1 Model PT path and initial compositions

Kinematic models of heat transfer in subduction zones (e.g., Syracuse et al 2010; Van Keken et al 2011; Peacock 1990, 1996; Peacock et al 2005) demonstrate that temperatures in the mantle wedge above the slab-mantle interface are similar to a class of hanging wall systems that give rise to "inverted metamorphism", in which temperature increases with decreasing depth along a vertical profile. To explore metasomatic effects I use a schematic PT gradient reflective of the inverted geotherm of a mantle wedge, ranging from 500 °C and 20 kbar at the nominal slab-mantle interface to 5 kbar at 800 °C at a point well into the mantle. Slab and mantle-wedge lithologies are commonly tectonically intermixed in a tectonic mélange (e.g., Bebout 2007). Such a mixture juxtaposes slab lithologies with high P metamorphic assemblages that contain quartz with low-Si ultramafic lithologies. The PT path I assume models fluid-rock interaction over a more extensive range of the mantle wedge conditions than is likely in a single subduction zone. However, it is useful to illustrate the range of infiltration reactions and magnitudes rather than to correspond exactly to a particular thermal model, and it allows evaluation of effects for many medium to high T subduction systems.

The model assumes that a H_2O-CO_2 fluid becomes quartz saturated via interaction with a slab lithology at some PT position in the slab-mantle mélange. The fluid then interacts with the surrounding ultramafic rock by exchanging silica. Following Manning (1995), the initial

unaltered model mantle wedge lithologies are assumed to be a mix of forsterite and enstatite in the MgO-SiO_2 system; bulk compositions ranging between pure enstatite to pure forsterite are explored. Although the true bulk composition of the mantle lithosphere requires FeO, Al_2O_3 and CaO, the results of this simplified model provide a fundamental understanding for CO_2 effects on silica metasomatism in silica undersaturated lithologies.

To illustrate the effects of Si metasomatism, the initial mantle lithologies were initially fully reacted with fluids with X_{CO2} of 0, 0.005, 0.05 and 0.2, which represent CO_2-poor to CO_2-rich subduction-zone settings. Figure (4.6) shows the starting mantle-wedge mineral assemblages as a function of the initial mode of enstatite (relative to forsterite) and pressure along the PT path. Note that P and T covary; the temperature at a particular pressure is shown along the top of the figure. The fields in the diagrams correspond to univariant assemblages, the horizontal lines to divariant assemblages, and the vertical lines to invariant assemblages in the MSCOH system. Forsterite and enstatite are stable together in the presence of an H_2O-CO_2 fluid only at low P and high T. Closer to the slab, the starting assemblages comprise a mix of hydrous minerals ± magnesite depending on X_{CO2}. As X_{CO2} increases, the magnesite-bearing assemblages occupy a progressively greater portion of the starting mantle wedge.

4.4.4.2 X_{Si} in fluids along the PT path

Modeling Si metasomatism in carbonated rocks requires knowledge of PT-X_{Si} phase relations. I used the same methods as in Section 4.3 to compute stable phase diagrams at the four X_{CO2} conditions (Fig. 4.7). As T rises and P declines, the solubility of quartz increases. Any initially quartz saturated fluid thus contains progressively more dissolved Si, at a given X_{CO2}, at shallower positions. As in the isobaric phase relations at 1 GPa (Fig. 4. 5), increasing X_{CO2} yields

a progressively larger stability field of magnesite. However, unlike Fig 4.5, it appears that there is a compensating effect between P and T such that there is little change in the X_{Si} of the phase boundaries at a given P-T.

In the CO_2-free MSH system, a fully hydrated bulk composition with 70 initial volume % forsterite ($V_{fo}°$), or $V_{en}° = 30\%$, will be made up of antigorite + brucite adjacent to the subduing slab at 20 kbar and 500 °C (Fig. 4.6), and the static pore fluid is buffered at $X_{SiO2} = 3.42E\text{-}05$ (fig 4.7A). As depth decreases, and temperature raises, X_{SiO2} increases along the univariant antigorite-brucite line until the invariant point brucite + antigorite + forsterite is reached at 18.8 kbar, 524 °C, where the static pore fluid contains $X_{SiO2} = 4.32E\text{ -}05$. At this point, decreasing pressure follows the univariant line antigorite + forsterite (Fig. 4.6) until the invariant point talc + antigorite + forsterite is reached 13.4 kbar, 632 °C, where the pore fluid contains $X_{SiO2} = 1.55E\text{ -}03$. The shallow slopes of the univariant lines forsterite + talc and enstatite + forsterite result in little change in X_{SiO2} as the pressure decreases to 5 kbar, 800 °C, where $X_{SiO2} = 4.58E\text{-}03$. Thus, as for a quartz-bearing rock, in the absence of carbonation, a pore fluid in an silica undersaturated MSH rock will also see rising X_{Si} along the model PT path.

In contrast, in the presence of CO_2, the trend becomes more complex because magnesite dramatically affects the X_{SiO2} of the pore fluid (Fig. 4.7B-D). For example, at 20 kbar and 500 °C, $V_{fo}° = 70\%$ and $X_{CO2} = 0.005$, the stable assemblage at the slab top is magnesite + quartz, where the pore fluid contains $X_{SiO2} = 3.65E\text{ -}03$ (Fig. 4.7B). This is approximately 100X more enriched in silica then at the same conditions in the MSH system. Decreasing P and increasing T leads to invariant point magnesite + quartz + talc at 19.4 kbar, 512 °C, at which $X_{SiO2} = 4.10E\text{-}03$, hitting the maximum X_{SiO2} for this bulk composition. Further decrease in P (increase in T) lowers the X_{SIO2} of the fluid because the stable assemblage is now magnesite + talc. The decline

continues until the invariant point talc + antigorite + magnesite at 15.4 GPa, X_{SiO2} = 1.34E-03. Despite the decline, X_{Si} is still 3X more concentrated in silica than at the same PT in the MSH system. The decline in Si concentration continues to the next invariant point antigorite + magnesite + forsterite at 1.44 GPa and 612 °C and the MSH (X_{SiO2} = 7.36E-04). With further P decrease, the assemblages are the same as in the CO_2-free system. Due to the inconsequential change in the activity of water (a_{H2O} = 0.995 and a_{H2O} =1.0, respectively), the X_{SiO2} of the two systems are nearly identical. Similar effects can be seen upon increasing X_{CO2} from 0.005 to 0.05 or 0.2, except that they are shifted to shallower conditions due to the expansion of the magnesite stability field.

4.4.4.3 SiO_2 metasomatism

For metasomatism driven by infiltration of SiO_2-bearing $H_2O \pm CO_2$ fluid, the total number of moles of the fluid, n_F, corresponds to the initial concentrations of SiO_2 H_2O and CO_2 in the fluid is defined by:

$$n_F = n^i_{SiO2} + n^i_{H2O} + n^i_{CO2} \tag{4.22}$$

The mole fractions of SiO_2, H_2O, CO_2 are thus

$$X^i_{SiO2} = \frac{n^i_{SiO2}}{n^i_{SiO2} + n^i_{H2O} + n^i_{CO2}} = \frac{n^i_{SiO2}}{n_F} \tag{4.23}$$

and

$$X^i_{H2O} = \frac{n^i_{H2O}}{n^i_{SiO2} + n^i_{H2O} + n^i_{CO2}} = \frac{n^i_{H2O}}{n_F} \tag{4.24}$$

$$X^i_{CO2} = \frac{n^i_{CO2}}{n^i_{SiO2} + n^i_{H2O} + n^i_{CO2}} = \frac{n^i_{CO2}}{n_F} \tag{4.25}$$

which leads to

$$n^i_{SiO2} = X^i_{SiO2} n_F \tag{4.26}$$

and

$$n^i_{H2O} = X^i_{H2O} n_F \tag{4.27}$$

$$n^i_{CO2} = X^i_{CO2} n_F \tag{4.28}$$

To understand how the addition of a silica drives the consumption of low-silica phases and the production of high silica phases, consider the general reaction between a Mg carbonate (A) and a hydrated Mg-silicate (E):

$$aA + bH_2O + cSiO2 = dCO_2 + eE \tag{4.29}$$

Assuming Mg is immobile, the stoichiometry for Eq. (2.29) requires that for any progress of the reaction, the abundance of A and E, and the concentrations of H_2O, SiO_2, CO_2 in the fluid, change in proportion to the reaction's stoichiometry. All chemical reactions are statements of

mass balance, so the change in any one species, Δn_i, in the reaction must be related to change in all the others. Thus, from Eq. (4.20):

$$\xi = \frac{\Delta n_A}{-\nu_A} = \frac{\Delta n_{H2O}}{-\nu_{H2O}} = \frac{\Delta n_{SiO2}}{-\nu_{SiO2}} = \frac{\Delta n_{CO2}}{\nu_{CO2}} = \frac{\Delta n_E}{\nu_E} \tag{4.30}$$

Equation (4.30 shows how the reaction progress is explicitly interlinked with the abundance or concentration of each participating species.

During metasomatism, an initial fluid is modified into a final fluid of known composition. The changes in fluid components due to metasomatism are

$$\Delta n_{SiO2} = n^f_{SiO2} - n^i_{SiO2} \tag{4.32}$$

$$\Delta n_{H2O} = n^f_{H2O} - n^i_{H2O} \tag{4.33}$$

and

$$\Delta n_{CO2} = n^f_{CO2} - n^i_{CO2} \tag{4.34}$$

For Si metasomatism, combination of Eq. (4.23) and (4.32-4.34) gives the final Si concentration

$$X^f_{SiO2} = \frac{n^i_{SiO2} + \Delta n_{SiO2}}{n^i_{SiO2} + \Delta n_{SiO2} + n^i_{H2O} + \Delta n_{H2O} + n^i_{CO2} + \Delta n_{CO2}} \tag{4.35}$$

and combining with Eq. (4.30) leads to

$$X_{SiO2}^{f} = \frac{n_{SiO2}^{i} + \nu_{SiO2}\xi}{n_{SiO2}^{i} + \nu_{SiO2}\xi + n_{H2O}^{i} + \nu_{H2O}\xi + n_{CO2}^{i} + \nu_{CO2}\xi} \tag{4.36}$$

Solving Eq. (4.36) for ξ gives

$$\xi = \frac{n_{SiO2}^{i} - X_{SiO2}^{f}\left(n_{SiO2}^{i} + n_{H2O}^{i} + n_{CO2}^{i}\right)}{X_{SiO2}^{f}(\nu_{SiO2} + \nu_{H2O} + \nu_{CO2}) - \nu_{SiO2}} \tag{4.37}$$

Noting that $(\nu_{SiO2} + \nu_{H2O} + \nu_{CO2})$ is the sum of the reaction coefficients of all components in the fluid, $\sum_j \nu_j$, and combining with Eq. (4.22) gives

$$\xi = \frac{n_T\left(X_{SiO2}^{i} - X_{SiO2}^{f}\right)}{X_{SiO2}^{f}\sum_j \nu_j - \nu_{SiO2}} \tag{4.38}$$

Equation (4.38) can be rearranged to give Eq. (4.21), here written in terms of infiltration of a silica metasomatizing H_2O-CO_2 fluid:

$$n_F = \xi \frac{\nu_{SiO2} - X_{SiO2}^{f}(\sum_j \nu_j)}{\left(X_{SiO2}^{f} - X_{SiO2}^{i}\right)} \tag{4.39}$$

As an example of applying Eq. (4.39), determining the number of moles of silica saturated fluid required for the complete conversion of reactant A to the product E in Eq. (4.29) can be determined by:

$$n_F = \left(\frac{\Delta n_A}{-\nu_A}\right) * \left(\frac{\nu_{SiO2} - X^f_{SiO2}(-b-c+d)}{\left(X^f_{SiO2} - X^i_{SiO2}\right)}\right) \quad (4.40)$$

Figure 4.8 demonstrates the effects of infiltration of fixed number of moles of (n_F) of silica saturated H_2O-CO_2 fluid into model mantle wedge lithologies. Each panel of 4 figures shows a given X_{CO2} with four representative values of n_F: 0.1, 1, 3, 6. At the lowest water rock ratio, $n_F = 0.1$, only a slight metasomatic modification of the mineral assemblages occurs from fig (4.6). At P < 6.5 kbar and $V°_{en} > 95\%$, enstatite is consumed to form talc and then anthophyllite formation, regardless of X_{CO2}. As n_F increases, the silica-poor assemblages are replaced by silica-rich assemblages. In the CO_2-free system, at $n_F = 3$, forsterite has been completely converted to higher Si minerals. An additional 3 moles ($n_F = 6$) results in the near complete replacement of silica poor assemblages by high-Si ones.

When the starting bulk rock composition is both hydrated and carbonated at a fixed X_{CO2}, values of n_F only slightly greater than those causing hydration and carbonation of the peridotite result in little metasomatic modification and are like Fig 4.6. At $X_{CO2} = 0.005$, X_{SiO2} is nearly the same as in pure water (Fig 4.7), resulting in silicate-only reactions undergoing metasomatic modification at similar rates to those in Fig 4.8. However, fields containing magnesite require larger volumes of fluid to convert magnesite to silica-bearing assemblages (Fig. 4.8B-D). Increasing X_{CO2} from 0.005 to 0.2 in the metasomatizing fluid results in a decrease in X_{SiO2}, and an increase in magnesite stability. The stability of magnesite and the reduced X_{SiO2} of the fluid allows greater volumes of metasomatizing fluids to interact with the silica-pore assemblages before converting to higher variant assemblages (Fig. 4.8B-D). Once an assemblage is in equilibrium with quartz, the assemblage no longer records the fluid rock interaction.

Figure 4.9 illustrates n_F required to convert starting mineral assemblages to Si-metasomatic assemblages for selected starting bulk compositions. For example, Dick et al. (1984) showed that typical abyssal peridotites are spinel harzburgites with 75 ± 5% olivine, 21 ± 4% enstatite, 3.6 ± 2% diopside and 0.5 ± 0.2% spinel. Therefore, metasomatic phase relations for $V°_{en}$ = 20% may closely approximate fluid-rock interactions in natural mantle-wedge peridotites above subducting oceanic lithosphere. Starting bulk compositions with higher $V°_{en}$ of 50 and 70% are useful to account for any previous history of silica addition elsewhere in the subduction system. For all bulk compositions and initial bulk CO_2 content, certain mineral assemblages are diagnostic of SiO_2 addition. This can be seen in Figure 4.9, which shows values of nF required to generate mineral assemblages indicative of Si addition. For example, the assemblage talc + enstatite always requires Si addition, though the value of n_F required to produce this assemblage varies with initial X_{CO2} and $V°_{en}$. Similarly, at any condition, hydrated and carbonated peridotite requires the addition of silica to produce the assemblages enstatite + anthophyllite, talc + anthophyllite, anthophyllite + quartz, and talc + quartz (Fig. 4.9).

In the MSH system (X_{CO2} = 0.0), the generation of diagnostic silicification assemblages requires only a few moles of fluid before quartz saturation occurs at intermediate depth and temperature. As the temperature decreases to 500 °C at 20 kbar, the concentration of silica in the fluid decreases and higher nF is required to produce silica rich assemblages. Figure 4.9 demonstrates that assemblages that intersect or nearly the quartz saturation surface (Fig. 4.7) necessitate highly variable quantities of fluid to convert the low silica assemblage to the higher variant state. For example, the assemblage talc + anthophyllite, at $V°_{en}$ = 20%, and 0.66 GPa, 48.25 mol/cm^3 of fluid is required at to convert all the anthophyllite to talc, while at 8.2 kbar only 3.71 mol/cm^3 is required. The conversion of enstatite to anthophyllite, which nearly intersects

the silica saturation line at 5 kbar, requires 9.11 mol/cm^3 while only 2.6 mol/cm^3 of fluid are required at 8.2 kbar. The presence of talc + quartz provides a minimum of approximately 3.5 mol/cm^3 of fluid, and interacted with the periodate regardless of its starting forsterite and enstatite composition. The significant increase in n_F needed to produce quartz-saturated assemblages can be explained by Eq. (4.39), which shows that as X_{SiO2}^{f} approaches X_{SiO2}^{i} the denominator approaches zero and n_T goes to infinity.

4.5. Conclusion

In this experimental work, I presented the first oxygen fugacity-controlled measurements that constrained the concentration of silica in H_2O-CO_2 fluids in equilibrium with magnesite + forsterite, magnesite + talc, and magnesite + quartz. Additionally, the first ever single crystal forsterite solubility measurements were conducted in H_2O-CO_2 fluids and demonstrated enhanced forsterite solubility compared to pure water (Marcris et al., 2020), which provides evidence for Mg-C complexing in the fluid. Quartz solubility measurements in the presence or absence of magnesite indicated that Mg and Si do not form complexes.

My results allow for the development of a thermodynamic model capable of predicting the concentration of silica quartz buffering reactions in H_2O-CO_2 fluids. The model indicates that concentration of silica in pore fluids not buffered by magnesite decrease in concentration with decreasing temperature and increasing X_{CO2}. However, under the correct conditions the presence of magnesite can enhance the concentration of silica in a pore fluid over 100X that in the equivalent CO_2-free assemblage. This result demonstrates that in silica undersaturated systems, contrary to intuition, silica solubility is enhanced even as the a_{H2O} decreases. The results provide

a foundation for modeling of silica metasomatism during infiltration of H_2O-CO_2 fluids in high pressure environments. This leads to the identification of mineral assemblages diagnostic of Si addition, and can quantify the amount of fluid needed to produce such assemblages.

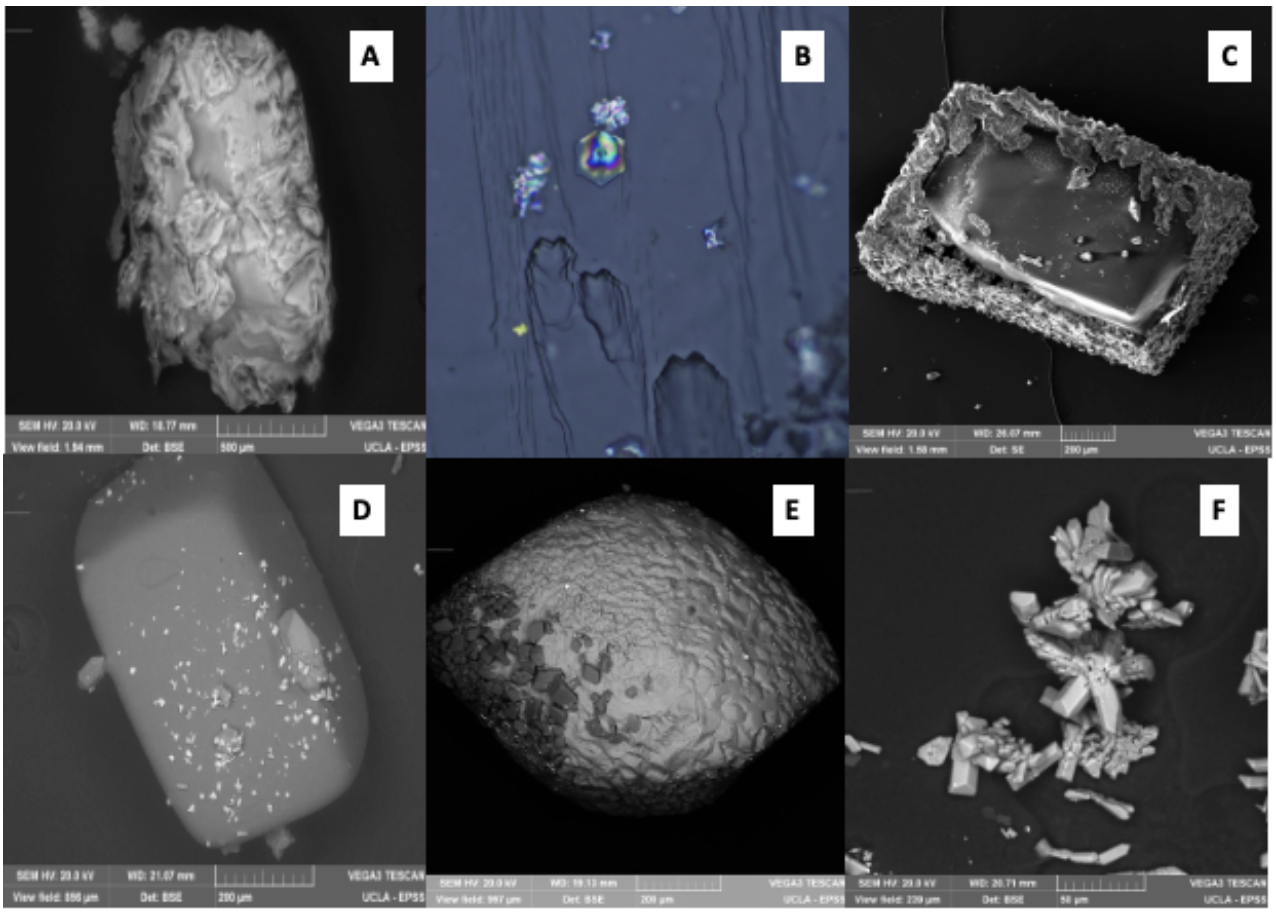

Figure. 4.1. (A) Backscattered electron image of talc replacing magnesite demonstrating silica saturation and conversion of magnesite to talc (MGFO_77). (B) Reflected light image of talc crystals attached to the surface of a magnesite. X_{Si} is near silica saturation resulting in few talc crystals (MGFO_54). (C) Backscattered electron image of euhedral secondary forsterite crystals pseudomorphing a magnesite crystal. The forsterite formed by by reaction with Si-rich fluid at 800 °C, 10 kbar, and X_{CO2} = 0.05. The original outline of the magnesite is seen by the forsterite rind. (D) Backscattered electron image of euhedral forsterite crystal in run MGFO_GOLD. Bright spots are Ag crystal precipitated upon quenching, which are derived from the decarbonation of AgOX. (E) Backscattered electron image depicting incongruent dissolution of forsterite to magnesite (FOCO_14). (F) Backscattered electron image of vapor transported forsterite crystals resulting from the addition of silica prior to run and congruent forsterite dissolution (FOCO_18).

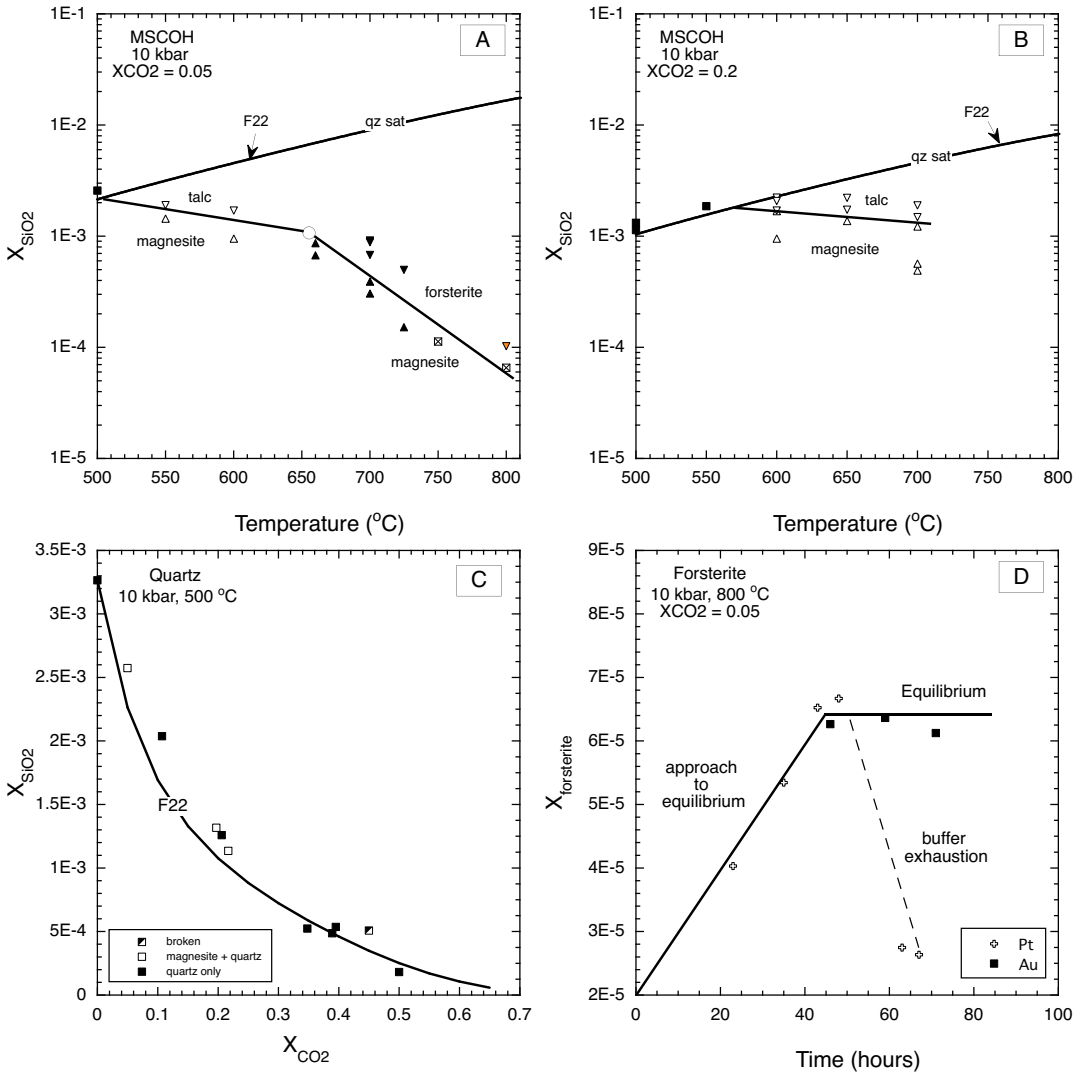

Figure. 4.2 (A, B) Mole fraction of silica (X_{SiO2}) vs temperature (°C) at 10 kbar and 500 – 800 °C, X_{CO2} = 0.05 and 0.20. Symbol key: sold black squares represent quartz solubility in the presence of magnesite; open triangles represent bracketed magnesite + talc equilibrium; closed triangles represent bracketed forsterite experiments (downward facing open triangles represent experiments with excess X_{SiO2} resulting in congruent forsterite solubility and are considered maximum due to numerous small forsterite crystal growth); squares with an internal x represent congruent forsterite solubility experiments; orange downward facing triangle is run MGFO_GOLD which demonstrated runs in excess of 30 hours were required to form forsterite on magnesite surface. The black line at silica saturation was calculated using methods outlined in Chapter 3. The black lines at magnesite + talc and magnesite + forsterite represent the constrained silica concentration at univariant equilibrium. The magnesite + talc + forsterite invariant point is depicted as an open circle. (C) Quartz solubility in H_2O-CO_2 solutions vs X_{SiO2} of quartz solubility in the presence of magnesite compared to predicted X_{SiO2} in Chapter 3. The overlap in data implies negligible Mg-Si complexing. (D) Forsterite solubility vs time at 800 °C, 10 kbar, X_{CO2} = 0.05. Forsterite dissolves congruently at these conditions. Results demonstrate that 38 hours was required for equilibrium

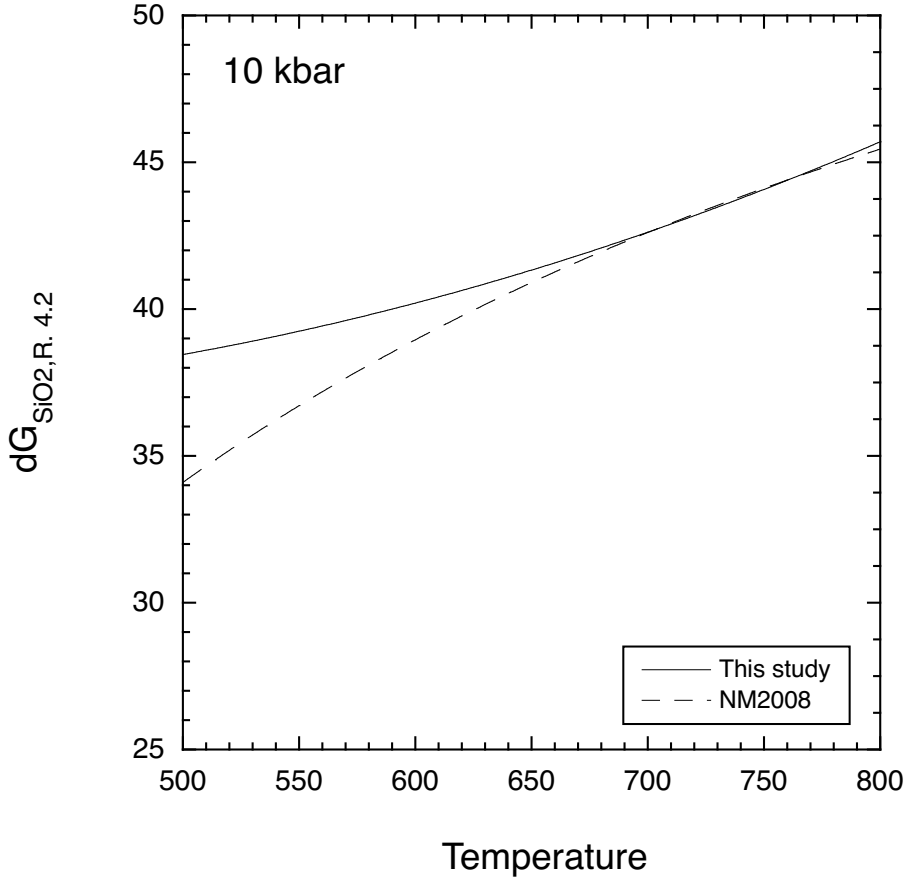

Figure. 4.3. Standard Gibbs free energy of Reaction (4.2) at 10 kbar and 500 – 800 °C. The dashed line represents values calculated from Newton and Manning (2008, Eq. 8). The sold black line represents values calculated using the newly formulated model for silica hydration (Chapter 3).

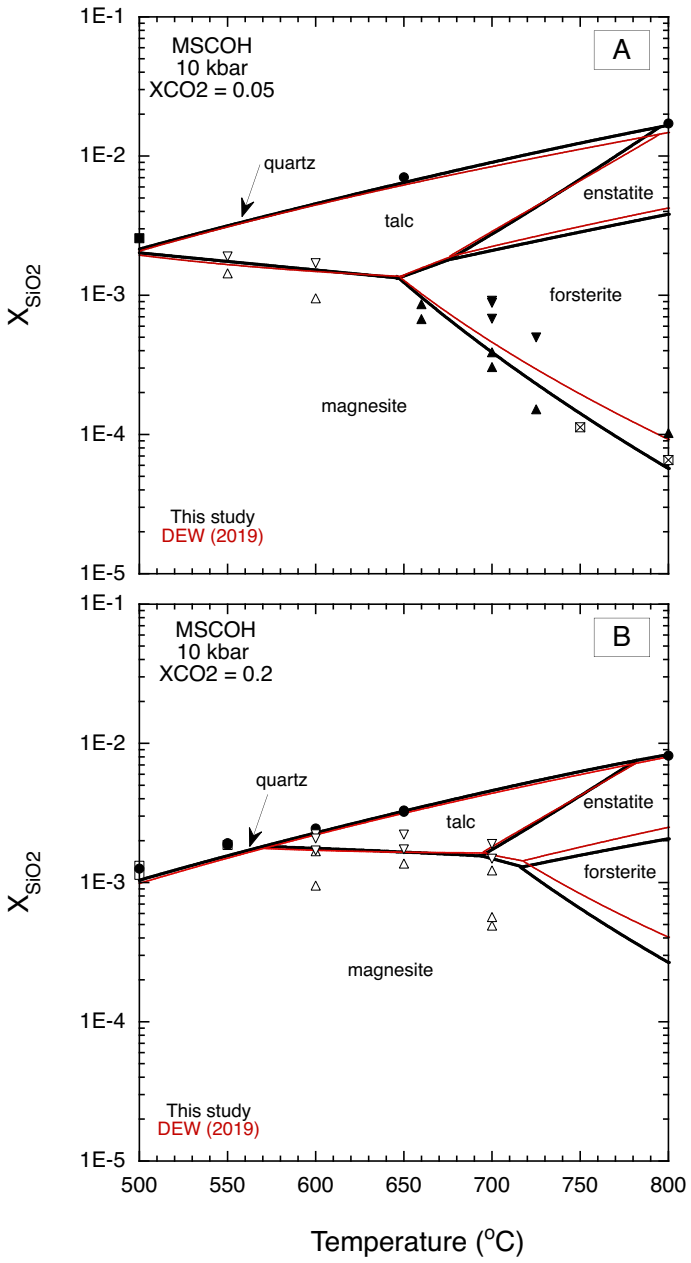

Figure. 4.4. Experimental results compared to calculated T-X_{SiO2} phase relations for reactions in Table (4.3) at 10 kbar, 500 to 800 °C, X_{CO2} = 0.05 and 0.20 using the two approaches outlined in section 4.4.1.2. and 4.4.1.3. The black lines represent the calculated $X_{SiO2,}$ using the modified Newton and Manning (2008) model and the red lines represent X_{SiO2} calculated using the DEW model.

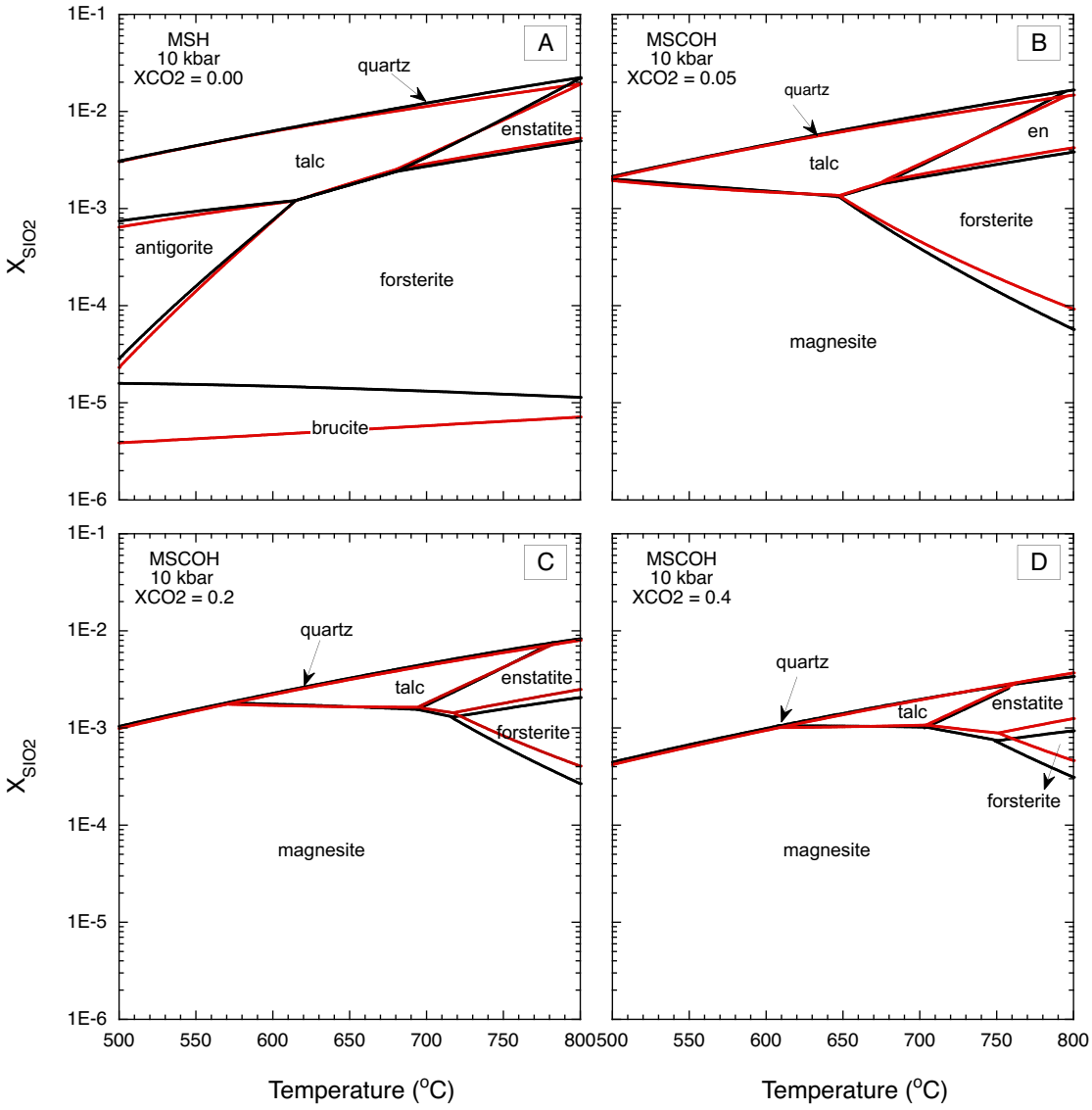

Figure. 4.5. The phase relations for reactions in Table (4.3) at 10 kbar, 500 to 800 °C, X_{CO2} = 0.05, 0.05, 0.20, 0.40 using the two approaches outlined in section 4.4.1.2. and 4.4.1.3. The black lines represent the calculated $X_{SiO2,}$ using the modified Newton and Manning (2008) model and the red lines represent X_{SiO2} calculated using the DEW model. Increasing X_{CO2} results in expansion of the magnesite stability field and increasing X_{SiO2} with decreasing temperature along the magnesite + talc, magnesite + enstatite and magnesite + forsterite equilibrium.

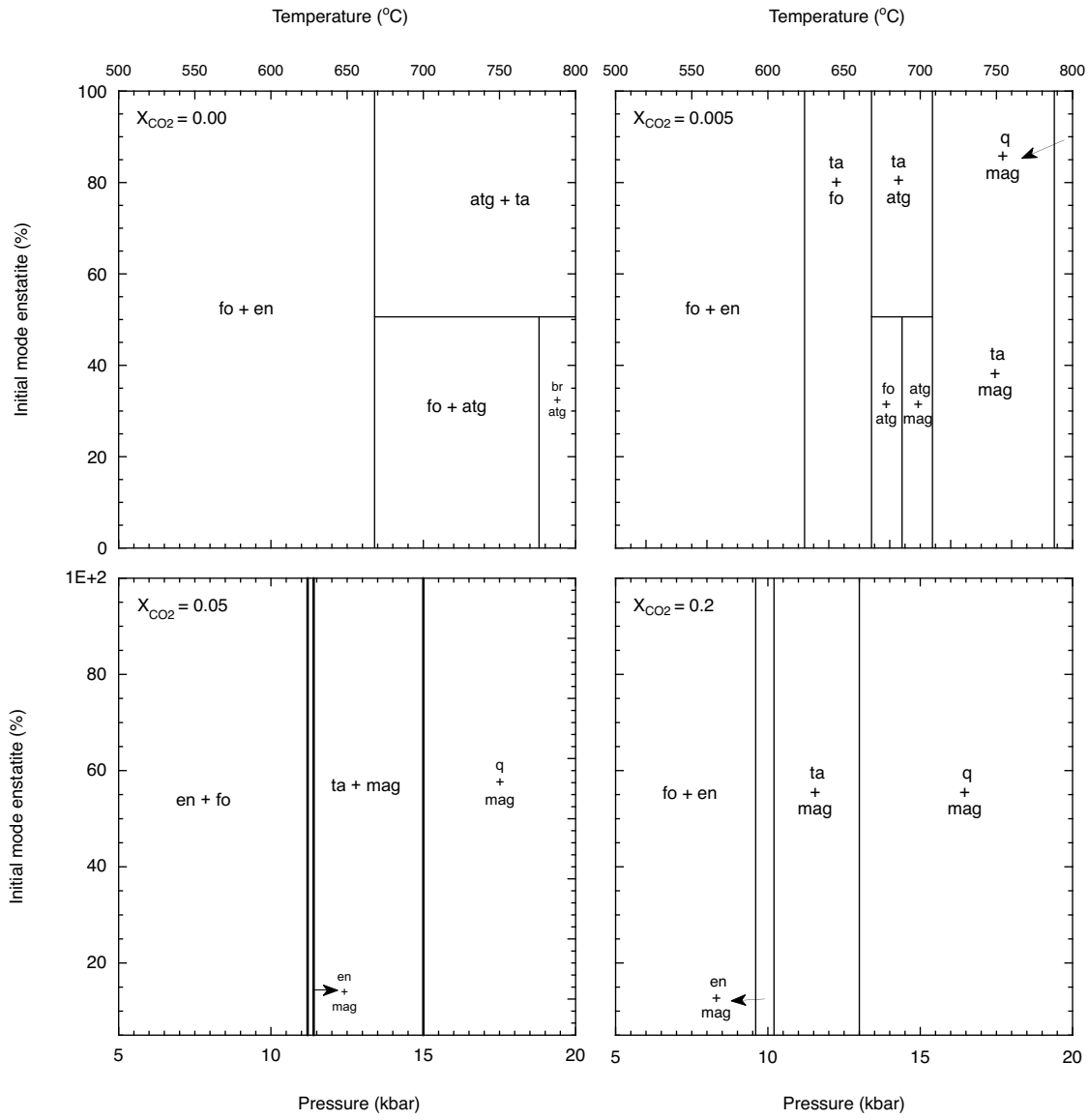

Figure. 4.6. Fully hydrated and carbonated MSCOH peridotite assemblages as a function of P and T along the model geothermal gradient. Considered compositions were limited to the range from 100 vol% enstatite to 100 vol% forsterite.

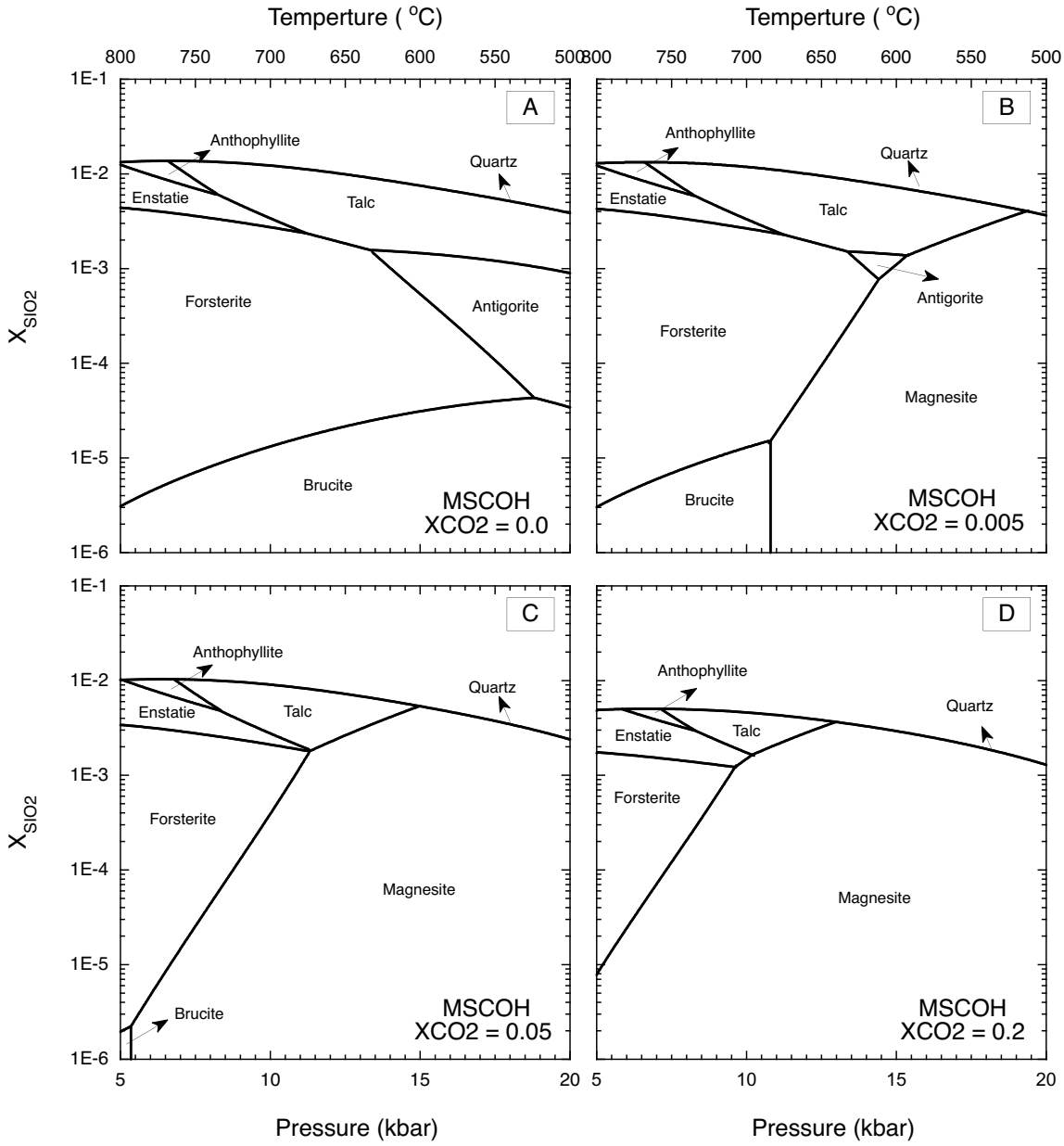

Figure. 4.7. Metasomatic phase diagrams in the system MSCOH at X_{CO2} = 0.000, 0,005, 0.050 and 0.200, along the model geothermal gradient.

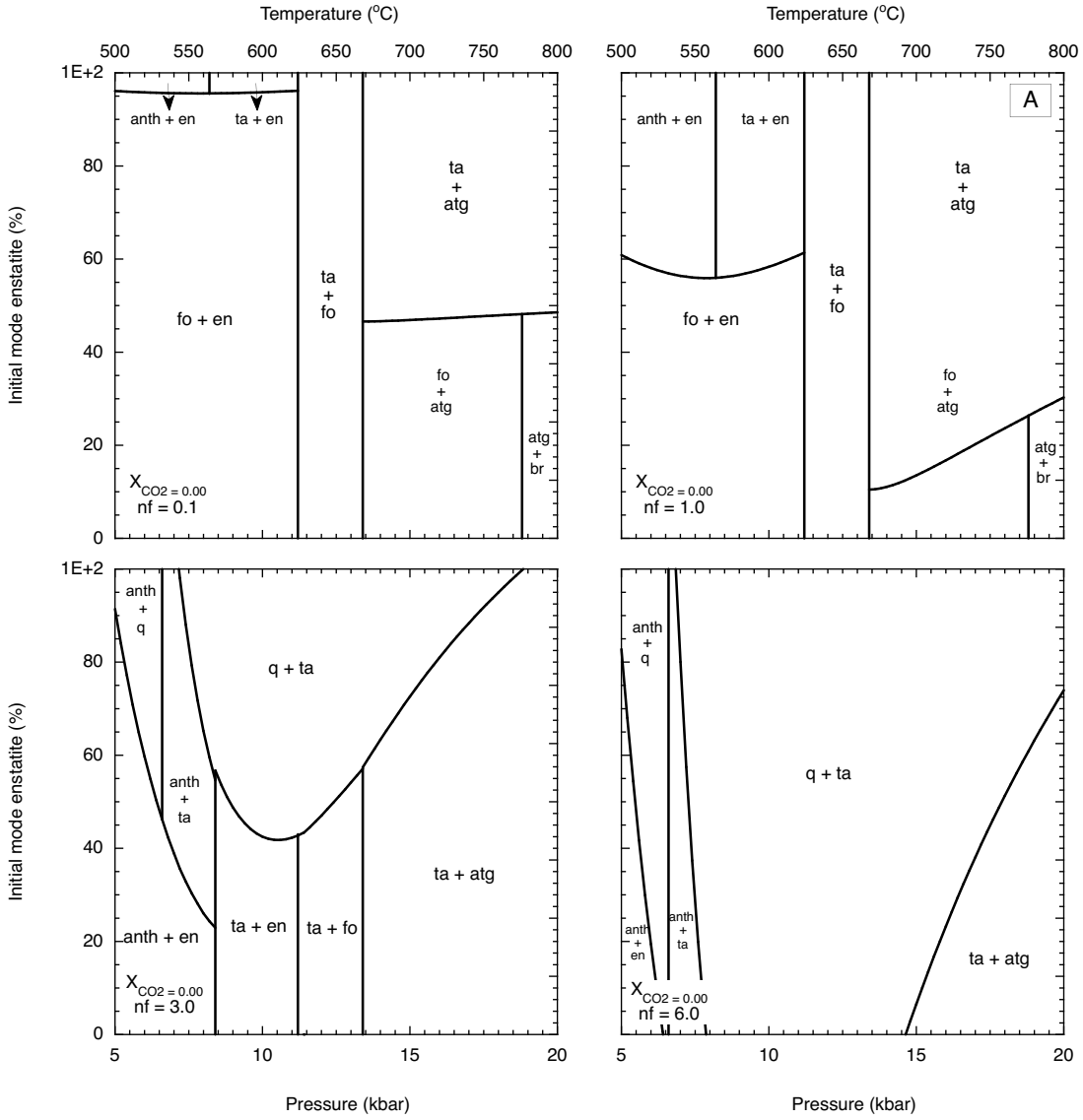
Temperature (°C)
500 550 600 650 700 750 800
1E+2
80
60
40
20
0
Initial mode enstatite (%)
anth + en
ta + en
ta + atg
ta + fo
fo + en
fo + atg
atg + br
$X_{CO2 = 0.00}$
nf = 0.1
A
nf = 1.0
anth + q
q + ta
anth + ta
ta + en
ta + fo
anth + en
nf = 3.0
anth + en
nf = 6.0
5 10 15 20
Pressure (kbar)

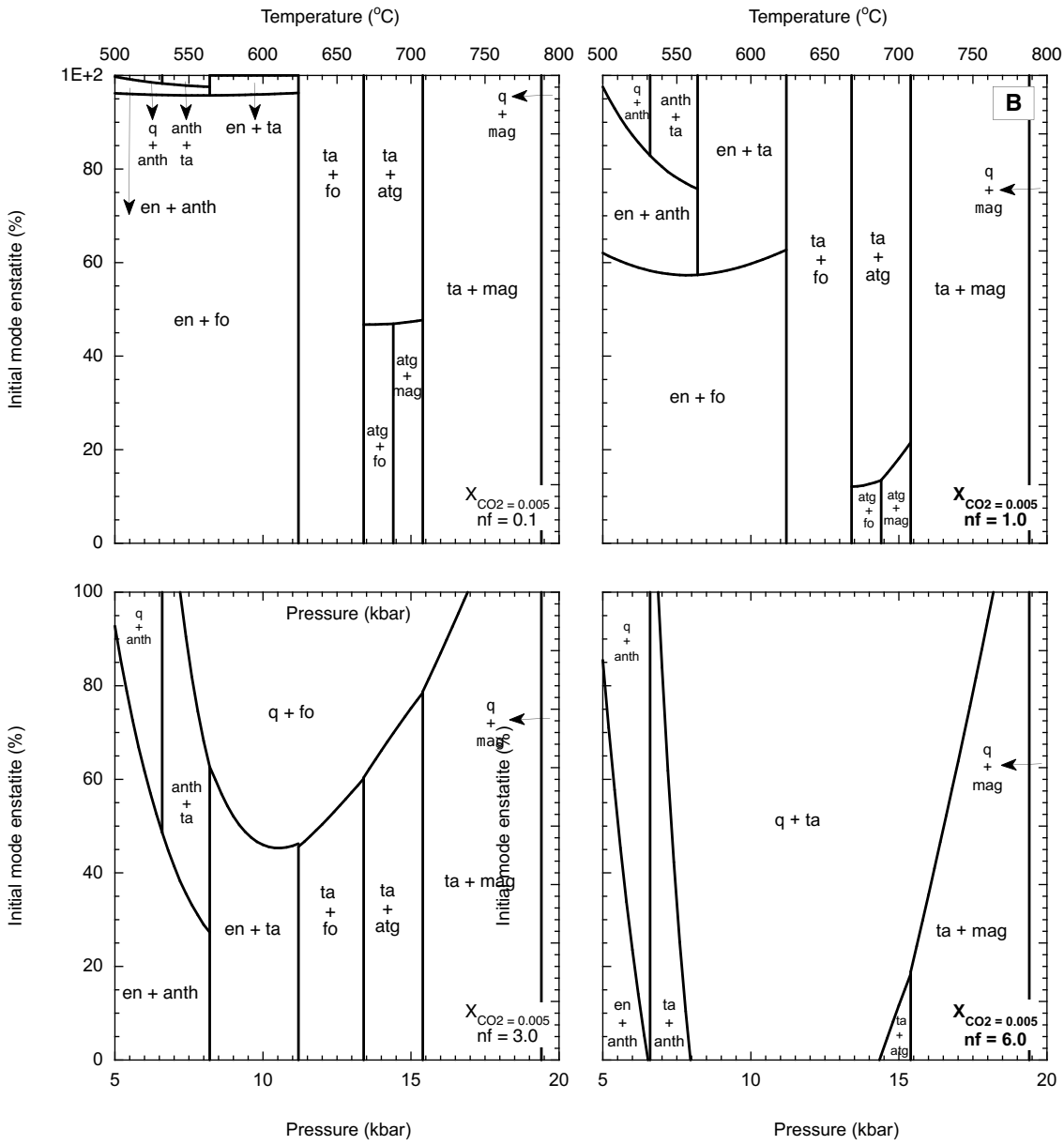
Temperature (°C)
500
550
600
650
700
750
800
1E+2
80
60
40
20
0
Initial mode enstatite (%)
q + anth
anth + ta
en + ta
en + anth
en + fo
ta + fo
ta + atg
atg + mag
atg + fo
ta + mag
q + mag
X CO2 = 0.005
nf = 0.1
B
anth + ta
X CO2 = 0.005
nf = 1.0
100
Pressure (kbar)
q + fo
X CO2 = 0.005
nf = 3.0
5
10
15
20
q + ta
en + anth
ta + anth
ta + atg
X CO2 = 0.005
nf = 6.0

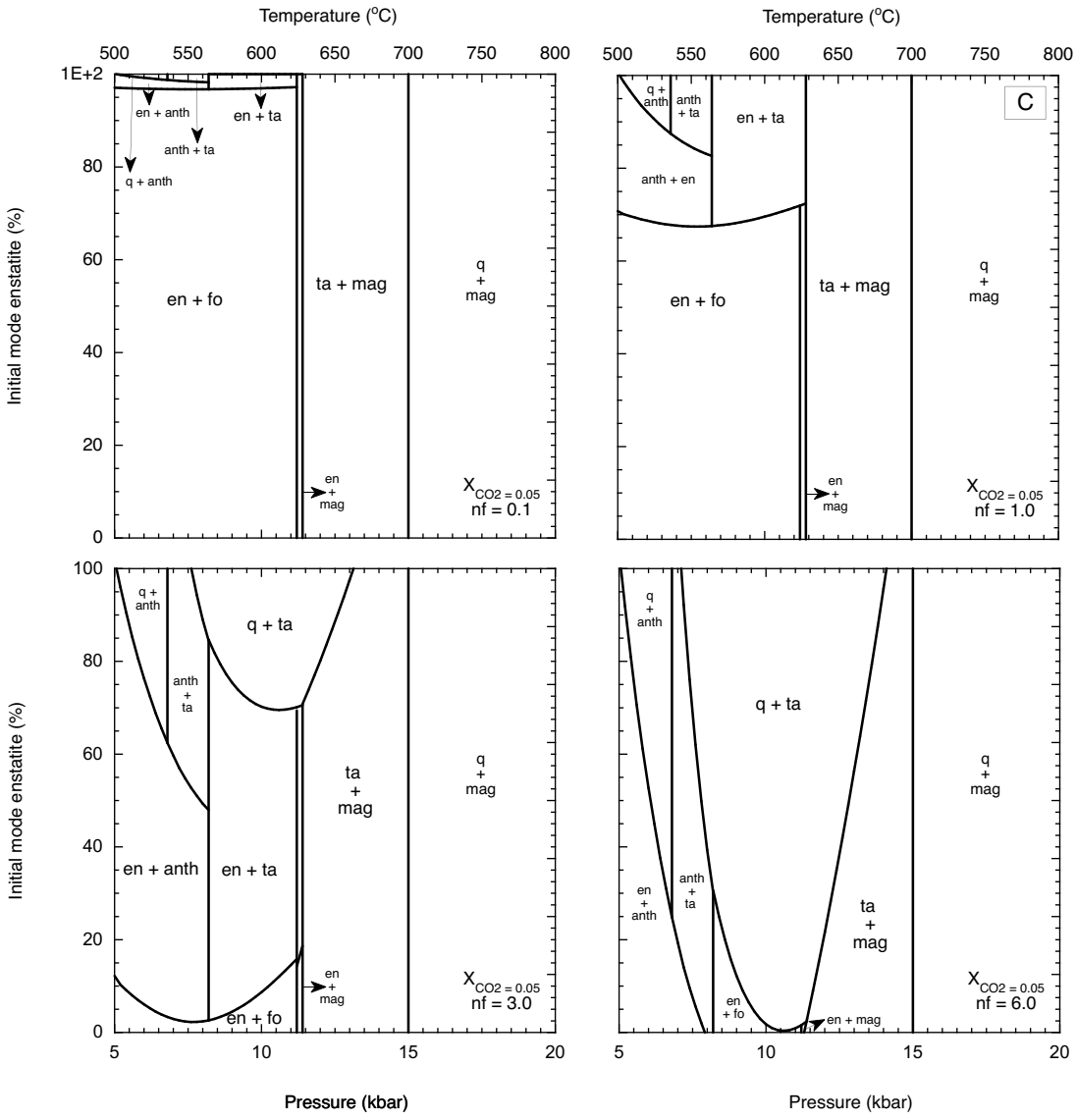
Temperature (°C)
500
550
600
650
700
750
800
1E+2
80
60
40
20
0
Initial mode enstatite (%)
en + anth
anth + ta
en + ta
q + anth
en + fo
ta + mag
q
+
mag
en
+
mag
X CO2 = 0.05
nf = 0.1
C
q +
anth
anth
+ ta
en + ta
anth + en
nf = 1.0
100
q + ta
anth
+
ta
ta
+
mag
nf = 3.0
en
+
anth
en + fo
nf = 6.0
5
10
15
20
Pressure (kbar)

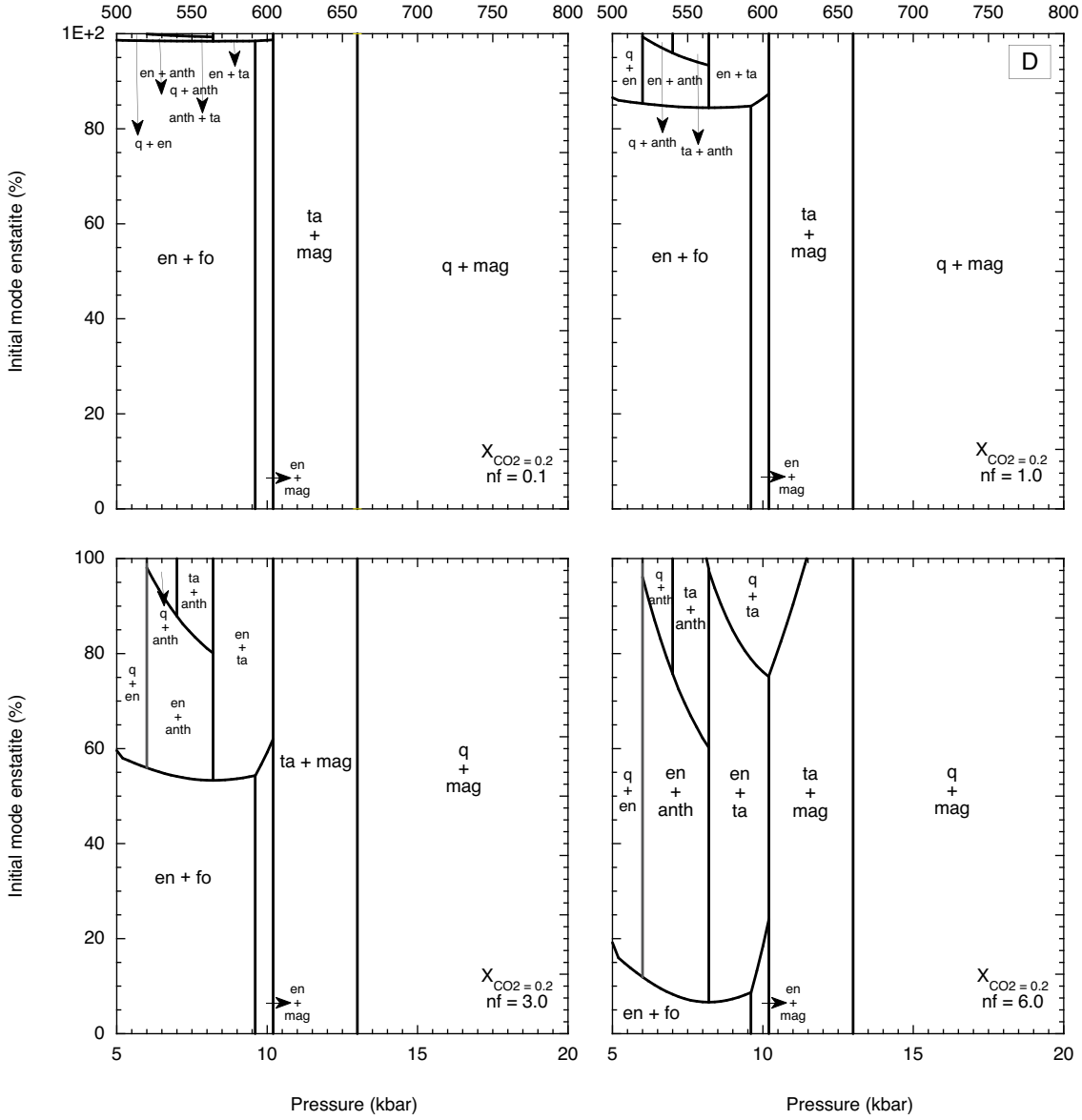

Figure. 4.8. Metasomatic assemblages produced by a isothermal, isobaric flow of different quantities of quartz-saturated fluid as a function of starting enstate mode and position along the model geothermal gradient.

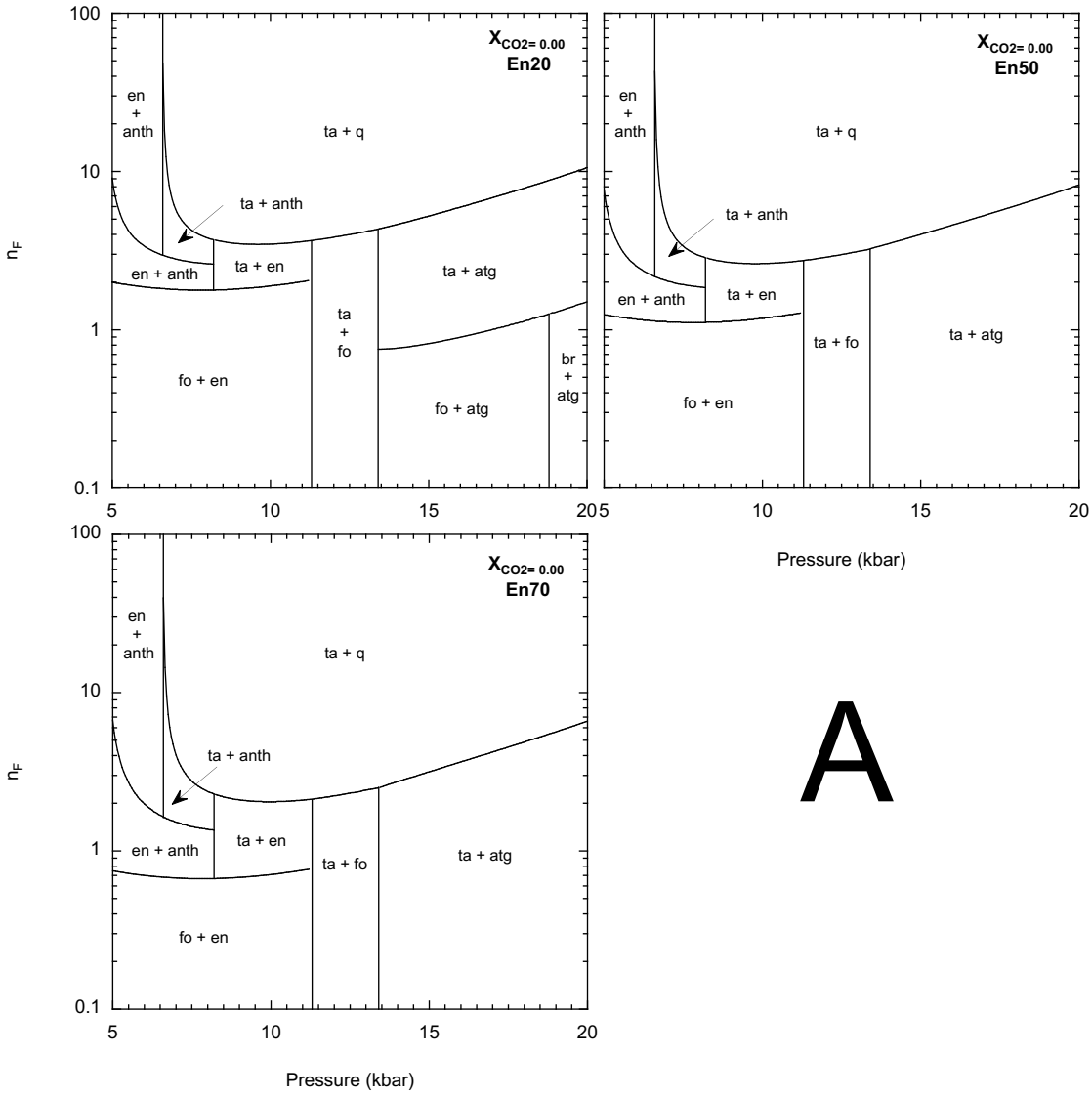
$X_{CO2= 0.00}$
En20
en + anth
ta + q
ta + anth
en + anth
ta + en
ta + atg
ta + fo
fo + en
fo + atg
br + atg
$X_{CO2= 0.00}$
En50
ta + fo
$X_{CO2= 0.00}$
En70
n_F
Pressure (kbar)
100
10
1
0.1
5
10
15
20

A

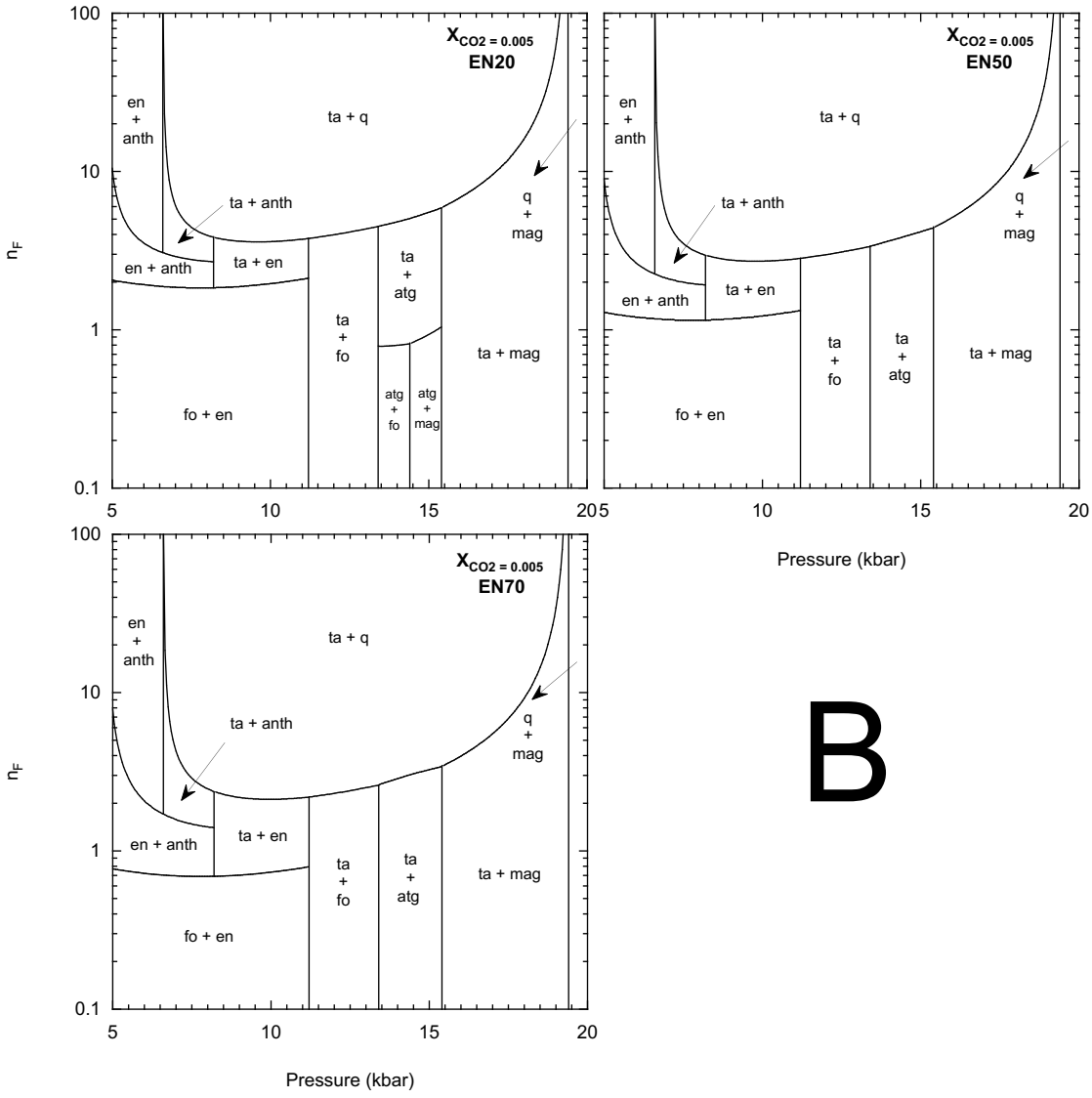
X_{CO2} = 0.005
EN20
EN50
EN70
en + anth
ta + q
ta + anth
q + mag
en + anth
ta + en
ta + atg
ta + fo
ta + mag
fo + en
atg + fo
atg + mag
n_F
Pressure (kbar)
100
10
1
0.1
5
10
15
20

B

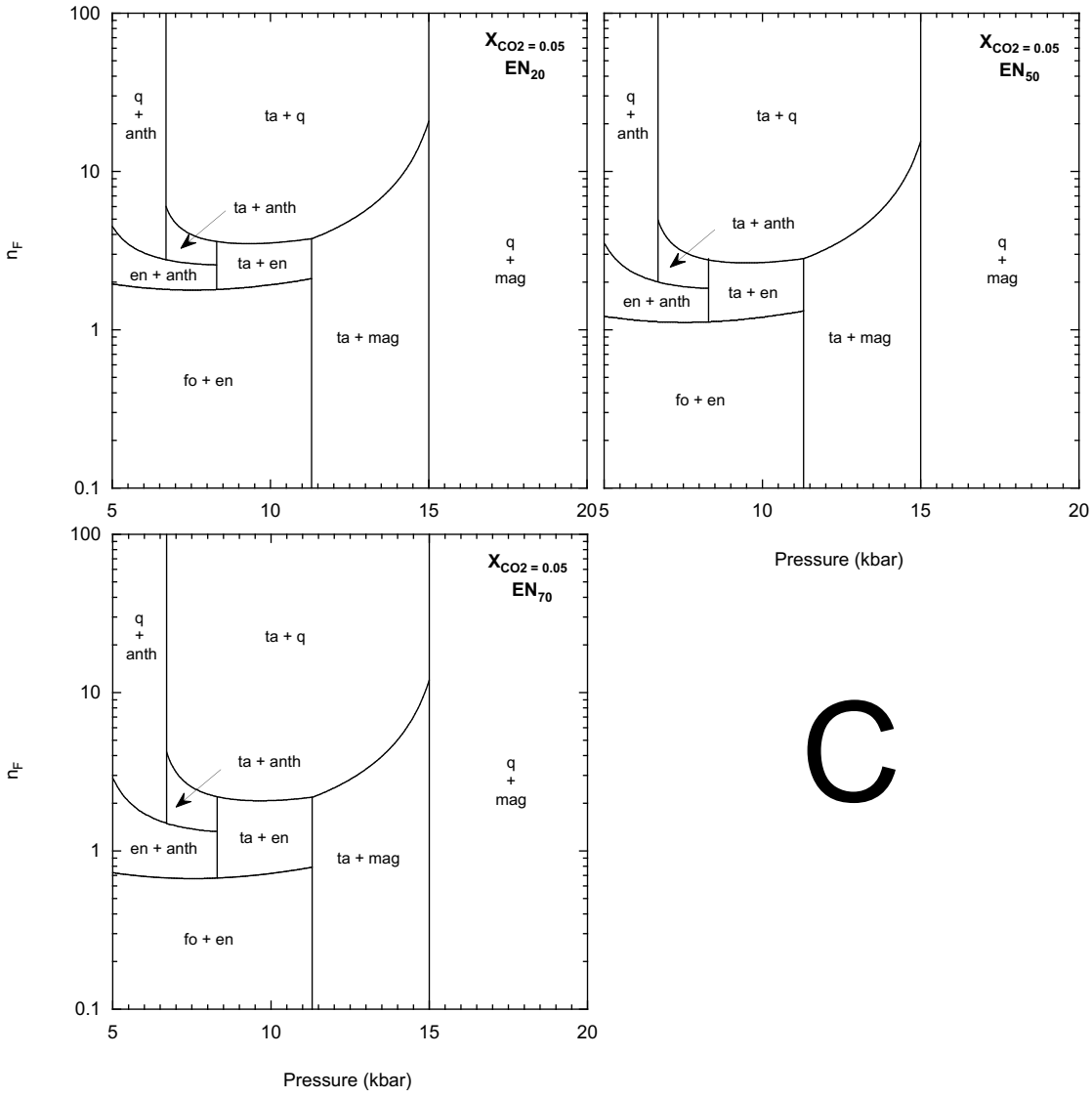
$X_{CO2 = 0.05}$
EN_{20}
$X_{CO2 = 0.05}$
EN_{50}
$X_{CO2 = 0.05}$
EN_{70}
q + anth
ta + q
ta + anth
ta + en
en + anth
ta + mag
fo + en
q + mag
n_F
100
10
1
0.1
5
10
15
20
Pressure (kbar)

C

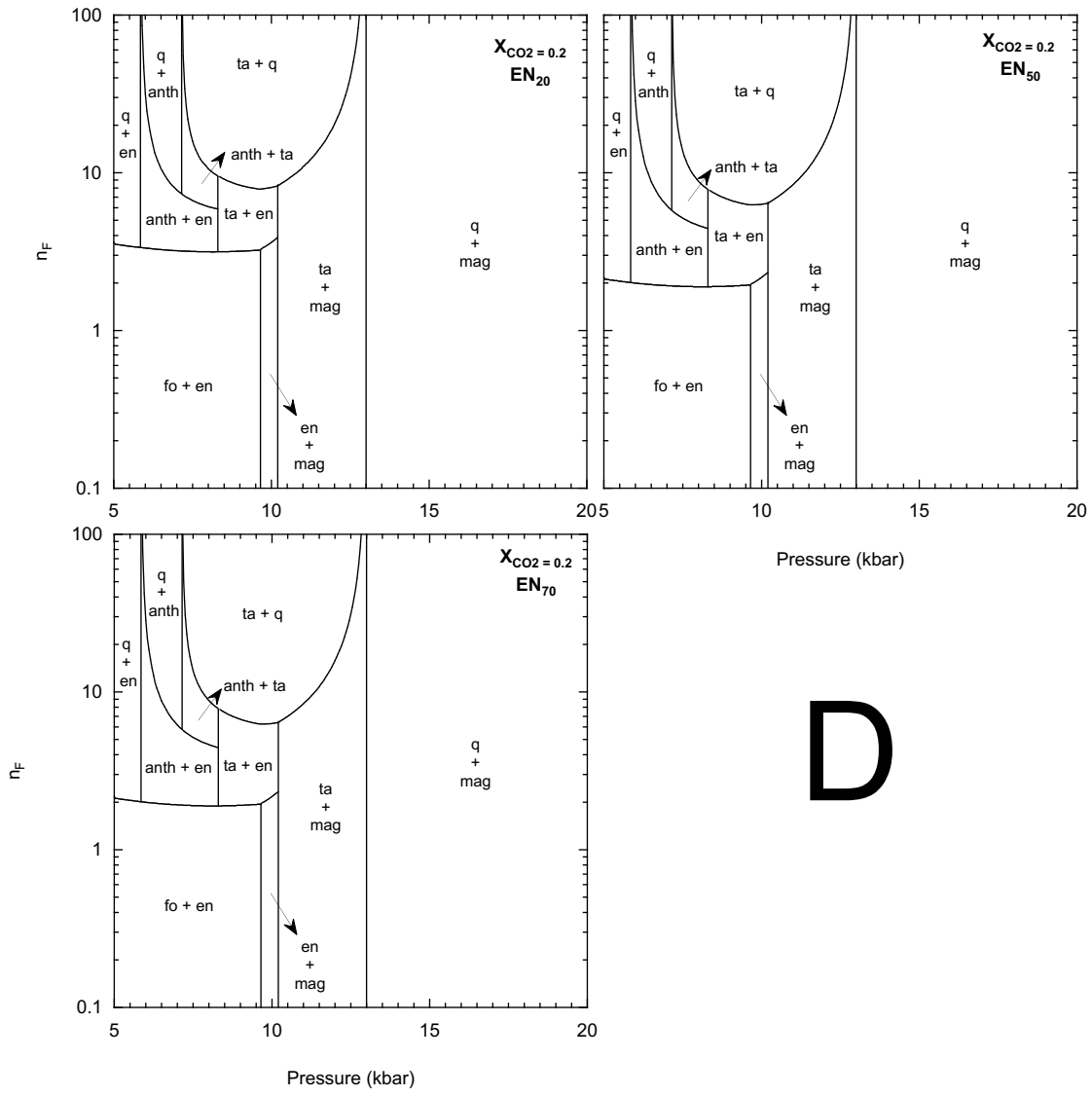

Figure. 4.9. Variations of water-rock ratios required to produce metasomatic mineral asemblages by isothermal, isobaric flow of a quartz-saturated fluid.

Table. 4.1. Results of Brackets solubility runs at 10 kbar.

Expt. Number	Temp °C	Duration (hr)	OAD mg	H_2O mg	H_2O_{tot}	Silica float µg	q, in mg	q,out mg	X_{CO2}	X_{H2O}	X_{SiO2}	Buffer	Run Products
QT_54	500	4.0	0.0000	29.6938	29.6938	N/A	2.53117	2.20673	0.00	0.997	0.00327(0)	HW	q
MGFO_101*	500	72.0	1.5002	7.7321	8.1608	N/A	1.08983	1.0159	0.05	0.948	0.00257(0)	HW	mag +q
MGFO_89*	500	72.0	5.3732	4.6894	6.2251	N/A	0.61310	0.58180	0.20	0.792	0.00121(0)	HW	q
MGFO_82*	500	30.0	4.8815	4.2897	5.6848	N/A	1.85537	1.82423	0.20	0.802	0.00132(0)	HW	mag + q
MGFO_87*	500	72.0	4.8835	3.6510	5.0467	N/A	0.64627	0.62185	0.22	0.782	0.00114(1)	HW	mag + q
MGFO_95*	550	48.0	1.4659	7.5483	7.9672	40.260	N/A	N/A	0.05	0.949	0.00144(0)	HW	mag
MGFO_106*	550	26.0	1.4802	7.2483	7.6713	51.440	N/A	N/A	0.05	0.946	0.00190(0)	HW	mag +talc
MGFO_83*	550	24	4.8436	4.0141	5.3984	42.170	1.270	1.228	0.20	0.794	0.00186(0)	HW	mag + q
MGFO_90*	550	42	5.4808	4.3770	5.9434	N/A	2.74450	2.69627	0.21	0.790	0.00192(0)	HW	q
MGFO_53*	600	25.0	5.6426	27.5897	29.2023	97.700	N/A	N/A	0.05	0.947	0.00095(0)	MW	mag
MGFO_81*	600	23.0	1.1376	5.4345	5.7596	34.530	N/A	N/A	0.05	0.945	0.00170(0)	HW	mag + ta
MGFO_49	600	6.3	18.4500	15.3061	20.5791	191.660	N/A	N/A	0.20	0.794	0.00222(0)	MW	mag + ta
MGFO_55	600	1.0	17.8900	15.4765	20.5894	234.200	N/A	N/A	0.20	0.799	0.00272(0)	MW	mag +ta
MGFO_56	600	0.5	18.5599	15.4654	20.7698	184.900	N/A	N/A	0.20	0.795	0.00212(0)	MW	mag + ta
MGFO_57	600	1.0	18.4285	15.5440	20.8108	194.290	N/A	N/A	0.20	0.796	0.00223(0)	MW	mag
MGFO_92*	600	22.0	5.5254	4.7531	6.3323	54.640	N/A	N/A	0.20	0.798	0.00207(0)	HW	mag + ta
MGFO_94	600	22.0	5.5288	4.4190	5.9991	45.840	N/A	N/A	0.21	0.790	0.00181(1)	HW	fail
MGFO_96*	600	23.0	5.5240	4.5305	6.1093	43.040	N/A	N/A	0.21	0.793	0.00168(0)	HW	mag
MGFO_85*	650	20.0	4.7827	4.2493	5.6162	51.560	N/A	N/A	0.20	0.802	0.00221(0)	HW	mag + ta
MGFO_88*	650	24.0	4.8140	3.8214	5.1972	37.900	N/A	N/A	0.21	0.789	0.00173(0)	HW	mag + ta
MGFO_91*	650	22.0	4.7935	3.8291	5.1991	28.700	N/A	N/A	0.21	0.790	0.00131(0)	HW	mag
MGFO_102	650	20.0	5.4291	4.4271	5.9787	80.800	2.756.8	2.676	0.21	0.791	0.00321(1)	HW	q
MGFO_103	650	22.0	5.6302	4.5371	6.1462	85.570	2.67277	2.5882	0.21	0.790	0.00330(0)	HW	q
MGFO_30*	700	2.5	18.9184	16.2732	21.6800	44.430	N/A	N/A	0.20	0.799	0.00049(0)	MW	mag
MGFO_32*	700	3.0	17.9060	15.3775	20.4950	48.270	N/A	N/A	0.20	0.799	0.00056(0)	MW	mag
MGFO_39*	700	3.0	17.7553	15.2278	20.3022	103.460	N/A	N/A	0.20	0.799	0.00122(0)	MW	mag
MGFO_41*	700	3.0	17.8507	15.4202	20.5219	161.970	N/A	N/A	0.20	0.796	0.00189(0)	MW	mag + ta

MGFO_54*	700	2.0	17.8660	15.1564	20.2625	124.460	N/A	N/A	0.20	0.801	0.00147(0)	MW	mag + ta
MGFO_100*	800	48	1.5047	7.8396	8.2697	N/A	2.53477	2.0287	0.05	0.934	0.01714(0)	HW	q
MGFO_105*	800	5.0	5.8139	4.6001	6.2617	N/A	2.548	2.331	0.21	0.783	0.00815(0)	HW	q

Explanation: Weights of Oxalic acid, and H2O are prior to experiment; H2Otot is sum of H2O added and H2O derived from breakdown of oxalic acid dyhdrate. Qtz,in, weight of quartz before run, q, out, weight of quartz after experiment. Abbreviations: OAD, oxalic acid dihydrate; mag, magnesite; q, quartz; ta, talc; ts, time series. Buffers: MW, Mn oxides + H2O; HW, hematite + H2O.

Table. 4.2. Results of Brackets solubility runs at 10 kbar.

Expt. no	Temp °C	Dur. (hr)	CO_2 source mg	H_2O mg	H_2O_{total} mg	fo in µg	fo out µg	silica µg	X_{CO2}	$X_{SiO2,total}$	X_{fo}	Run Products	capsule type	Notes
FOCO_24	660	44	6.5621	30.13063	32.0060654	126.97	70.24	52	0.055	6.741(1)E-04	2.143(3)E-04	fo + mag	Au	OAD
FOCO_25	660	38	6.18027	30.21004	31.9763491	68.9	9.63	71.9	0.052	8.631(0)E-04	2.247(2)E-04	fo + mag	Au	OAD
FoCO_17	700	78	15.3696	32.3140	32.3140	350.04	326.33	24.57	0.053	3.047(0)E-04	8.891(9)E-05	fo + mag	Au	AgOX,
FOCO_21	700	45	6.30967	30.32003	32.1233214	116.47	82.6	29.7	0.053	3.902(2)E-04	1.278(2)E-04	mag + fo	Au	OAD
FOCO_23	700	48	6.44347	30.20646	32.0479912	216.47	122.24	36.4	0.054	6.776(5)E-04	3.558(2)E-04	fo	Au	OAD
FOCO_22	700	46	6.23747	30.24526	32.0279168	175.73	62.7	51.27	0.053	8.820(0)E-04	4.277(4)E-04	fo	Au	OAD
FOCO_19	700	51	6.1615	30.26004	32.0209847	251.03	133.43	52.7	0.052	9.127(2)E-04	4.454(8)E-04	fo	Au	OAD
FoCO_14	725		14.7186	32.1581	32.1581	710	669.85	N/A	0.051	1.516(6)E-04	1.516(6)E-04	mag + fo	Au	AgOX,
FOCO_32	725	48	6.2782	32.0738	33.8680973	310.23	238.13	28.54	0.050	4.986(3)E-04	2.588(7)E-04	fo	Au	OAD
FoCO_13	750	66	15.2955	32.2255	32.2255	797.57	768.37	N/A	0.053	1.098(7)E-04	1.098(7)E-04	Fo	Au	AgOX, ts
MGFO_Gold	800	30	15.29054	34.8220	34.8220	0	0	12.5	0.050	1.023(5)E-04	-	mag + fo	Au	AgOX, Mag. St.
FOCO_0	800	23	14.6140	32.3916	32.3916	367.4	360.08	N/A	0.051	2.747(7)E-05	2.747(7)E-05	Fo	Pt	AgOX, ts
FoCO_1	800	23	10.5096	21.3998	21.3998	425.2	418.07	N/A	0.055	4.031(1)E-05	4.031(1)E-05	Fo	Pt	AgOX, ts
FoCO_5	800	35	14.7233	32.3683	32.3683	356.9	342.66	N/A	0.051	5.345(3)E-05	5.345(3)E-05	Fo	Pt	AgOX, ts
FoCO_4	800	43	14.5775	32.4992	32.4992	383.84	366.4	N/A	0.051	6.524(3)E-05	6.524(3)E-05	Fo	Pt	AgOX, ts
FoCO_9	800	46	14.3908	32.07713	32.07713	387.9	371.37	N/A	0.051	6.265(9)E-05	6.265(9)E-05	Fo	Au	AgOX, ts
FoCO_2	800	49	14.4012	30.1684	30.1684	418.53	401.93	N/A	0.054	6.668(9)E-05	6.668(9)E-05	Fo	Pt	AgOX, ts
FoCO_8	800	59	14.4117	32.5046	32.5046	209.5	192.5	N/A	0.050	6.362(1)E-05	6.362(1)E-05	Fo	Au	AgOX, ts
FoCO_3	800	67	14.5772	30.2059	30.2059	180.8	174.23	N/A	0.054	2.634(6)E-05	2.634(6)E-05	Fo	Pt	AgOX, ts
FoCO_6	800	71	18.6705	40.3322	40.3322	381.37	361.02	N/A	0.052	6.124(5)E-05	6.124(5)E-05	Fo	Au	AgOX, ts

Explanation: Weights of silver oxalate (AgOX), Oxalic acid dihydrate (OAD), and H2O are prior to experiment;.Fo,in, weight of forsterite before run, Fo, out, weight of forsterite after experiment. Abbreviations: OAD, oxalic acid dihydrate; mag, magnesite; fo, forsterite; ts, time series. Buffers: MW, Mn oxides + H2O; HW, hematite + H2O. For forsterite incongruent solubility measurements XSiO2 was determined by just the addition of silica float, the XSIO2 from the dissolution of forsterite was not recorded due to magnesite growth on forsterite crystals which did not allow for accurate weight loss measurements. The addition of silica float resulted in forsterite congruent solubility. The XSiO2 at forsterite congruent solubility was determined by the combination of silica float and the weight weight loss of the forsterite crystal and the collection of as many forsterite vapor transported crystals as possible. Because of this, XSIO2 is a maximum.

Table. 4.3. Selected Equilibria in the System $MgO\text{-}SiO_2\text{-}H_2O\text{-}CO_2$

MSH – base equilibria

a. $17\ Mg_3Si_2O_5(OH)_4 = 3\ Mg(OH)_2 + Mg_{48}Si_{34}O_{85}(OH)_{62}$
chrysotile brucite antigorite

b. $20\ Mg(OH)_2 + Mg_{48}Si_{34}O_{85}(OH)_{62} = 34\ Mg_2SiO_4 + 51\ H_2O$
brucite antigorite forsterite

c. $Mg_{48}Si_{34}O_{85}(OH)_{62} = 4\ Mg_3Si_4O_{10}(OH)_2 + 18\ Mg_2SiO_4 + 27\ H_2O$
antigorite talc forsterite

d. $Mg_3Si_4O_{10}(OH)_2 + Mg2SiO4 = 5MgSiO_3 + H_2O$
talc forsterite enstatite

e. $Mg_{48}Si_{34}O_{85}(OH)_{62} + 14\ Mg_3Si_4O_{10}(OH)_2 = 90MgSiO_3 + 45\ H_2O$
antigorite talc enstatite

f. $Mg_{48}Si_{34}O_{85}(OH)_{62} = 14\ Mg_2SiO_4 + 20\ MgSiO_3 + 31\ H_2O$
antigorite forsterite enstatite

g. $9\ Mg_3Si_4O_{10}(OH)_2 + 4\ Mg_2SiO_4 = 5\ Mg_7Si_8O_{22}(OH)_2 + 4\ H_2O$
talc forsterite anthophyllite

h. $Mg_7Si_8O_{22}(OH)_2 + Mg_2SiO_4 = 9\ MgSiO_3 + H_2O$
anthophyllite forsterite enstatite

i. $Mg_7Si_8O_{22}(OH)_2 = Mg_3Si_4O_{10}(OH)_2 + 4\ MgSiO_3$
anthophyllite talc enstatite

j. $7\ Mg_3Si_4O_{10}(OH)_2 = 3\ Mg_7Si_8O_{22}(OH)_2 + 4\ SiO_2 + 4\ H_2O$
talc anthophyllite quartz

k. $Mg_7Si_8O_{22}(OH)_2 = 7\ MgSiO_3 + SiO_2 + H_2O$
anthophyllite enstatite quartz

l. $Mg_3Si_4O_{10}(OH)_2 = 3\ MgSiO_3 + SiO_2 + H_2O$
talc enstatite quartz

m. $Mg(OH)_2 = MgO + H_2O$
brucite periclase

MSH- silicification equilibria

a. $3Mg_2Si_2O_6 + 2H_2O + 2SiO_{2,aq} = 2\ Mg_3Si_4O_{10}(OH)_2$
enstatite quartz talc

b. $3Mg_2SiO_4 + 2H_2O + 5SiO_{2,aq} = 2Mg_3Si_4O_{10}(OH)_2$
forsterite quartz talc

c. $Mg_2SiO_4 + SiO_{2,aq} = Mg_2Si_2O_6$
forsterite enstatite

d. $2MgCO_3 + 2SiO_{2,aq} = Mg_2Si_2O_6 + 2CO_2$
magnesite quartz enstatite

e. $7Mg_2Si_2O_6 + SiO_{2,aq} + H_2O = Mg_7Si_6O_{22}(OH)_2$
enstatite quartz anthophyllite

f. $3Mg_7Si_6O_{22}(OH)_2 + 4SiO_{2,aq} + 4H_2O = 7Mg_3Si_4O_{85}(OH)_{62}$
anthophyllite quartz antigorite

g. $24Mg_2SiO_4 + 10SiO_{2,aq} + 31H_2O = Mg_{48}Si_{34}O_{85}(OH)_{62}$
forsterite quartz antigorite

h. $Mg_{48}Si_{34}O_{85}(OH)_{62} + 30SiO_{2,aq} = 16Mg_3Si_4O_{10}(OH)_2 + 15H_2O$
antigorite quartz talc

i. $2Mg(OH)_2 + SiO_{2,aq} + Mg_2SiO_4 + 2H_2O$
brucite forsterite

j. $48Mg(OH)_2 + 34SiO_{2,aq} = Mg_{48}Si_{34}O_{85}(OH)_{62} + 17H_2O$
brucite quartz antigorite

k. $SiO_2,q + nH_2O = nH2O\bullet\ SiO_{2,aq}$
quartz Hydrated silica

l. $3Mg_7Si_8O_{22}(OH)_2 + 4\ SiO_{2,aq} + 4\ H_2O = 7\ Mg_3Si_4O_{10}(OH)_2$
anthophyllite talc

MSCH- Silicification equilibria

a. $3MgCO_3 + H_2O + 4SiO_{2,aq} = 3CO_2 + 1Mg_3Si_4O_{10}(OH)_2$

magnesite talc

b. $2MgCO_3 + SiO_{2,aq} = 2CO_2 + Mg_2SiO_4$
magnesite forsterite

c. $2MgCO_3 + 2SiO_{2,aq} = Mg_2Si_2O_6 + 2CO_2$
magnesite enstatite

d. $48MgCO_3 + 34SiO_{2,aq} + H_2O = Mg_{48}Si_{34}O_{85}(OH)_{62} + 48CO_2$
magnesite antigorite

[anthophyllite incompatible with magnesite]

---

*Reactant assemblages

Table. 4.4. Reaction Coefficients of H_2O and Secondary Minerals for Silicification of Model Peridotites

Stable Secondary assemblages	H_20	Brucite	Chrysotile	Antigorite	Talc	Forsterite	Enstatite	Anthophyllite	Magnesite
Brucite + Chrysotile	$\frac{3n_f^o + n_e^o}{2}$	$\frac{n_f^o + n_e^o}{2}$	$\frac{n_f^o + n_e^o}{2}$						
Chrysotile + antigorite	$\frac{3n_f^o + n_e^o}{2}$		$\frac{10n_f^o + 7n_e^o}{3}$	$\frac{n_e^o + n_f^o}{6}$					
Antigorite + talc	$\frac{3n_f^o + n_e^o}{2}$			$\frac{5n_f^o + n_e^o}{90}$	$\frac{7n_e^o + 10n_f^o}{45}$				
Antigorite + brucite	$\frac{51n_f^o + 17n_e^o}{17}$	$\frac{10n_f^o + 7n_e^o}{17}$		$\frac{n_f^o + n_e^o}{34}$					
Forsterite + antigorite	$\frac{31n_e^o}{20}$			$\frac{n_e^o}{20}$		$n_f^o - \frac{14n_e^o}{20}$			
Forsterite + talc	$\frac{n_e^o}{5}$				$\frac{n_e^o}{5}$	$n_f^o - \frac{n_e^o}{5}$	$n_e^o - \frac{20n_f^o}{14}$		
Enstatite + antigorite	$\frac{31n_f^o}{14}$			$\frac{n_f^o}{14}$					
Forsterite + enstatite						n_f^o	n_e^o		
Magnesite+ talc					$\frac{n_f^o + n_e^o}{4}$				$\frac{5n_f^o + n_e^o}{4}$
Magnesite + enstatite							$n_f^o + n_e^o$		n_f^o
Magnesite + Antigorite				$\frac{n_f^o + n_e^o}{34}$					$\frac{10n_f^o + 7n_e^o}{17}$
Talc + anthophyllite					$\frac{-9n_f^o - n_e^o}{4}$			$\frac{5n_f^o + n_e^o}{4}$	
Enstatite + anthophyllite							$9n_f^o + n_e^o$	$-n_f^o$	
Magnesite + forsterite						$n_f^o + n_e^o$			$-n_e^o$
Enstatite + talc							$5n_f^o + n_e^o$	$-n_f^o$	

n_f^o = initial forsterite content (moles); n_e^o= initial enstatite content (moles). Coefficients were derived using molar volumes from Holland and Powell (1998) by simultaneously solving for Mg, Si, and H mass-balance expressions for each assemblage.

4. References

Newton, R. C., Aranovich, L. Y., Hansen, E. C., & Vandenheuvel, B. A. (1998). Hypersaline fluids in Precambrian deep-crustal metamorphism. Precambrian Research, 91(1-2), 41-63.

Berman, R. G. (1988). Internally-consistent thermodynamic data for minerals in the system Na2O-K2O-CaO-MgO-FeO-Fe2O3-Al2O3-SiO2-TiO2-H2O-CO2. Journal of petrology, 29(2), 445-522.

Bebout, G. E., & Barton, M. D. (1989). Fluid flow and metasomatism in a subduction zone hydrothermal system: Catalina Schist terrane, California. Geology, 17(11), 976-980.

Brooks, H. L., & Steele-MacInnis, M. (2019). A model for the solubility of minerals in saline aqueous fluids in the crust and upper mantle. American Journal of Science, 319(9), 754-787.

Bohlen, S. R. (1984). Equilibria for precise pressure calibration and a frictionless furnace assembly for the piston-cylinder apparatus. Neues Jahrbuch für Mineralogie, Monatshefte, 404-412.

Chou, I. M., (1978) Calibration of oxygen buffers at elevated P T using the hydrogen fugacity sensor. American lite. Mineralogist, 63, 690–703.

Eugster , H. P., & Wones , D. R., (1962) Stability relations of the ferruginous biotite, annite. Petrol. 3, 82-125.

Ferrando, S. (2012). Mg-metasomatism of metagranitoids from the Alps: genesis and possible tectonic scenarios. Terra Nova, 24(6), 423-436.

Ferry, J. M. (1986). Reaction progress: a monitor of fluid—rock interaction during metamorphic

and hydrothermal events. In Fluid—Rock Interactions During Metamorphism (pp. 60-88). Springer, New York, NY.

Falk, E. S., & Kelemen, P. B. (2015). Geochemistry and petrology of listvenite in the Samail ophiolite, Sultanate of Oman: Complete carbonation of peridotite during ophiolite emplacement. Geochimica et Cosmochimica Acta, 160, 70-90.

Hacker, B. R. (2008). H2O subduction beyond arcs. Geochemistry, Geophysics, Geosystems, 9(3).

Holland, T. J. B., & Powell, R. (1990). An enlarged and updated internally consistent thermodynamic dataset with uncertainties and correlations: the system K2O–Na2O–CaO–MgO–MnO–FeO–Fe2O3–Al2O3–TiO2–SiO2–C–H2–O2. Journal of metamorphic Geology, 8(1), 89-124.

Holland, T. J. B., & Powell, R. T. J. B. (1998). An internally consistent thermodynamic data set for phases of petrological interest. Journal of metamorphic Geology, 16(3), 309-343

Holland TJB, Powell R (1991) A compensated-Redlich-Kwong (CORK) equation for volumes and fugacities of CO2 and H2O in the range 1 bar to 50 kbar and 100-1600°C. Contributions to Mineralogy and Petrology 109: 265-273

Huang, F., & Sverjensky, D. A. (2019). Extended Deep Earth Water Model for predicting major element mantle metasomatism. Geochimica et Cosmochimica Acta, 254, 192-230.

Kelemen, P. B., & Manning, C. E. (2015). Reevaluating carbon fluxes in subduction zones, what goes down, mostly comes up. Proceedings of the National Academy of Sciences, 112(30), E3997-E4006.

Koziol, A. M., & Newton, R. C. (1995). Experimental determination of the reactions magnesite+ quartz= enstatite+ CO2 and magnesite= periclase+ CO2, and enthalpies of formation of enstatite and magnesite. American Mineralogist, 80(11-12), 1252-1260.

Macris, C. A., Newton, R. C., Wykes, J., Pan, R., & Manning, C. E. (2020). Diopside, enstatite and forsterite solubilities in H2O and H2O-NaCl solutions at lower crustal and upper mantle conditions. Geochimica et Cosmochimica Acta, 279, 119-142.

Manning, C. E., & Boettcher, S. L. (1994). Rapid-quench hydrothermal experiments at mantle pressures and temperatures. American Mineralogist, 79(11-12), 1153-1158.

Manning, C. E. (2013). Thermodynamic modeling of fluid-rock interaction at mid-crustal to upper-mantle conditions. Reviews in Mineralogy and Geochemistry, 76(1), 135-164.

Newton, R. C., & Manning, C. E. (2002)a. Solubility of enstatite+ forsterite in H2O at deep crust/upper mantle conditions: 4 to 15 kbar and 700 to 900 C. Geochimica et Cosmochimica Acta, 66(23), 4165-4176.

Newton, R. C., & Manning, C. E. (2003). Activity coefficient and polymerization of aqueous silica at 800 C, 12 kbar, from solubility measurements on SiO2-buffering mineral assemblages. Contributions to Mineralogy and Petrology, 146(2), 135-143.

Newton, R. C., & Manning, C. E. (2006). Solubilities of corundum, wollastonite and quartz in H2O–NaCl solutions at 800 C and 10 kbar: interaction of simple minerals with brines at high pressure and temperature. Geochimica et Cosmochimica Acta, 70(22), 5571-5582.

Newton, R. C., & Manning, C. E. (2008). Thermodynamics of SiO2–H2O fluid near the upper critical end point from quartz solubility measurements at 10 kbar. Earth and Planetary Science Letters, 274(1-2), 241-249.

Newton, R. C., & Manning, C. E. (2009). Hydration state and activity of aqueous silica in H2O-

CO2 fluids at high pressure and temperature. American Mineralogist, 94(8-9), 1287-1290.

Newton, R. C., & Manning, C. E. (2010). Role of saline fluids in deep-crustal and upper-mantle metasomatism: insights from experimental studies. Geofluids, 10(1-2), 58-72.

Newton, R. C., & Manning, C. E. (2016). Evidence for SiO2-NaCl complexing in H2O-NaCl solutions at high pressure and temperature. Geofluids, 16(2), 342-348

Peacock, S. A. (1990). Fluid processes in subduction zones. *Science*, *248*(4953), 329-337.

Peacock, S. M. (1996). Thermal and petrologic structure of subduction zones. *Subduction: top to bottom*, *96*, 119-133.

Peacock, Simon M., Peter E. van Keken, Stephen D. Holloway, Bradley R. Hacker, Geoffrey A. Abers, and Robin L. Fergason. "Thermal structure of the Costa Rica–Nicaragua subduction zone." *Physics of the Earth and Planetary Interiors*149, no. 1-2 (2005): 187-200.

Plank, T., & Manning, C. E. (2019). Subducting carbon. Nature, 574(7778), 343-352.

Syracuse, E. M., van Keken, P. E., & Abers, G. A. (2010). The global range of subduction zone thermal models. *Physics of the Earth and Planetary Interiors*, *183*(1-2), 73-90.

Shock, E. L., & Helgeson, H. C. (1988). Calculation of the thermodynamic and transport properties of aqueous species at high pressures and temperatures: Correlation algorithms for ionic species and equation of state predictions to 5 kb and 1000 C. Geochimica et Cosmochimica Acta, 52(8), 2009-2036.

Sverjensky, D. A., Harrison, B., & Azzolini, D. (2014). Water in the deep Earth: The dielectric constant and the solubilities of quartz and corundum to 60 kb and 1200 C. Geochimica et Cosmochimica Acta, 129, 125-145.

Sverjensky, D. A., Shock, E. L., & Helgeson, H. C. (1997). Prediction of the thermodynamic properties of aqueous metal complexes to 1000 C and 5 kb. Geochimica et Cosmochimica Acta, 61(7), 1359-1412.

Takei H. and Hosoya S. (1985) Growth of MnSiO3 and (Mn,Mg)SiO3 crystals by the floating zone method. J. Crystal Growth 71, 17–22.

Tropper, P., & Manning, C. E. (2007). The solubility of corundum in H2O at high pressure and temperature and its implications for Al mobility in the deep crust and upper mantle. Chemical Geology, 240(1-2), 54-60.

Thompson, J.B., Jr., 1959, Local equilibrium in metasomatic processes, in Ableson, P.H., Researches in geochemistry, b. 1: New York, Hohn Wiley and Sons, p.427-457.

van Keken, P. E., Hacker, B. R., Syracuse, E. M., & Abers, G. A. (2011). Subduction factory: 4. Depth-dependent flux of H2O from subducting slabs worldwide. Journal of Geophysical Research: Solid Earth, 116(B1).

Walther, J. V., & Helgeson, H. C. (1977). Calculation of the thermodynamic properties of aqueous silica and the solubility of quartz and its polymorphs at high pressures and temperatures. Am. J. Sci.;(United States), 277(10).

Wolery, T. J. (1992). EQ3/6, a software package for geochemical modeling of aqueous systems: package overview and installation guide (version 7.0) (No. UCRL-MA--110662-PT. 1). Lawrence Livermore National Lab

Zotov, N., & Keppler, H. (2002). Silica speciation in aqueous fluids at high pressures and high temperatures. Chemical Geology, 184(1-2), 71-82.